UQAC
Université du Québec
à Chicoutimi

ACOUSTIC PERFORMANCE ANALYSIS OF AN APPARENT CLT FLOOR STRUCTURE

BY CHENG QIAN

MANUSCRIPT-BASED THESIS PRESENTED TO THE UNIVERSITY OF QUEBEC AT CHICOUTIMI IN PARTIAL FULFILLMENT OF THE REQUIREMENTS FOR THE DOCTOR OF PHILOSOPHY IN ENGINEERING

Supervisor:	**Sylvain Ménard ing., Ph.D.**	**Professor at the University of Québec at Chicoutimi**
Co-supervisors:	**Delphine Bard Ph.D., Docent**	**Associate Professor at Lund University**
	Jean-Luc Kouyoumji Ph.D.	**Research Project Manager at FCBA**

Québec, Canada

RÉSUMÉ

Avec le développement des sciences du bois et des techniques de construction, de plus en plus de bâtiments de grandes hauteurs, de longues portées se retrouvent dans le marché. Au cours des dernières années, la part de marché de la construction en bois n'a cessé d'augmenter. Contrairement à la renaissance de la construction en bois, le problème de l'isolation acoustique interpelle l'industrie. En général, par rapport à la construction lourde conventionnelle, comme les bâtiments en béton, les constructions en bois sont vulnérables au bruit, en particulier au bruit d'impact en basse fréquence. Différentes normes sont appliquées aux bâtiments en bois pour évaluer leurs performances acoustiques. Cependant, la norme ISO ne prend pas la considération le bruit en basse fréquence (en-dessous de 100 Hz). En conséquence, les occupants des bâtiments en bois peuvent se plaindre du bruit provenant de leurs voisins même si ces bâtiments respectent toutes les exigences de la réglementation. En revanche, en raison des différentes techniques de construction et de la grande variation des propriétés des matériaux à la base de bois, une haute qualité d'isolation acoustique devient difficile à atteindre par rapport aux constructions lourdes.

Les recherches réalisées dans cette thèse visent à acquérir une connaissance du comportement vibro-acoustique d’un plancher Cross Laminated Timber-béton et à développer un modèle de prédiction des bruits d'impact à basse fréquence de ce plancher. Pour atteindre ces objectives, les recherches ont été conduites en trois étapes principales: la prediction de la force; la description des incertitudes introduites par les propriétés mécaniques du bois; la modélisation du comportement dynamique d’un plancher bois-béton. Dans un premier temps, la force générée par la machine à choc ISO a été modélisée d'une manière indirecte. Au lieu de décrire directement la force générée par la machine à choc, la force est déduite à partir des accélérations du plancher et de la réponse fréquentielle du plancher. Ensuite, des tests expérimentaux ont été effectués pour extraire les informations dynamiques du plancher en bois et du plancher bois-béton. Par la suite, une approche stochastique a été proposée pour quantifier les incertitudes induites par les propriétés des matériaux du bois et pour automatiser la procédure de calibration. Basé sur le modèle du Cross Laminated Timber établi, différents matériaux ont été ajoutés au modèle pour simuler la réponse dynamique du plancher flottant. Une première investigation sur la force générée par cinq marteaux a été réalisée. Le niveau de pression acoustique rayonné par le plancher flottant a été simulée en intégrant la méthode de modélisation de la force et le modèle de plancher flottant. À partir des résultats de la simulation, il a été constaté que les propriétés du matériau ont un impact significatif sur les simulations dynamiques. Les propriétés plus précises du matériau peuvent conduire à un résultat plus précis.

Pour résumer, la connaissance sur la réponse dynamique du plancher a été obtenue par ce projet. De plus, des différentes méthodes pour modéliser le comportement dynamique du plancher sont appliquées afin d'obtenir des résultats précis. La connaissance apportée par cette recherche est un pas vers un modèle fiable de prédiction du bruit d'impact en basse fréquence.

ABSTRACT

Recent developments and innovations in wood science and manufacturing techniques, as well as environmental considerations, have contributed to the expansion of wooden constructions in the market. However, despite promising developments during the last decades, further expansion of the market share of wooden construction has been thwarted by problems at the level of acoustic insulation. Indeed, when compared to more conventional concrete constructions, the new wooden constructions are reputed to be vulnerable to noise; especially impact noise in the low-frequency range. One of the difficulties with the current standards used for the evaluation of the acoustic performance of wooden buildings is that these standards were originally developed for concrete buildings. Unfortunately, these standards do not include the most annoying low-frequency noises to which wooden structures are particularly vulnerable. As a result, even though these buildings conform to current building standards, the inhabitants in these dwellings complain about the noise coming from their neighbors. On the other hand, because of the different building techniques used, and the broad material properties of wood itself it can be difficult to achieve a high quality of acoustic insulation in wooden structures, especially when compared to concrete constructions.

The research reported in this thesis aims at developing a low-frequency impact sound prediction model for this type of floor. Three research steps were needed to achieve this: first, the prediction of the force; second, the quantification of the uncertainties induced by the material properties of wood; third, the modelling of the dynamic behavior of actual samples of

Cross Laminated Timber-concrete flooring. In the first step, the force generated by the ISO tapping machine was modelled by means of an indirect method that derived the force by the accelerations of the floor and the dynamic response of the floor instead of directly describing the force. Then, the tests were conducted to extract the dynamic information of the Cross Laminated Timber bare floor as well as the Cross Laminated Timber-concrete floor. The obtained experimental data are served as a reference to calibrate the model afterward. A stochastic approach was proposed to quantify the uncertainties induced by the material properties of wood and to automize the calibration procedure. Based on the developed Cross Laminated Timber model, different materials were integrated to the model to simulate the dynamic response of the floating floor. An initial investigation of the force generated by five hammers was carried out. The pressure radiated by the floating floor was simulated by integrating the force modelling method and the floating floor model. From the experimental phase, it can be concluded that the dynamic response of the structure is sensitive to the boundary conditions. In future experiment trials in order to successfully extract the useful dynamic information of the structure, the boundary conditions should be well defined. For the simulation perspective, it was found that the accuracy of the floor model can have an impact on the accuracy of the simulation of the force. Accurate material properties are one crucial prerequisite to have a more accurate floor model. From the simulation results, it can be seen that the material properties have a significant impact on the dynamic simulations. The use of more accurate material properties can lead to a more accurate result.

To sum up, knowledge of the dynamic behavior of the floors is obtained through this project and different modelling methods were applied in order to provide a relatively accurate simulation result. This research has successfully moved us one step towards a reliable low-frequency range impact sound prediction model.

ACKNOWLEDGMENT

First, I would like to thank my supervisor, Dr. Sylvain Ménard, for giving me the opportunity to come to Canada for this Ph.D. project and for his continuous support and encouragement. Likewise, I am grateful to co-supervisor Dr. Delphine Bard for keeping my stay at Lund University and also for the nice discussions and guidance. Then, I want to extend my thanks to my co-supervisor Dr. Jean-Luc Kouyoumji for the guidance of the experimental tests.

I am grateful to CIRCERB and CRMR and the industrial partners, FPInnovations and Nordic Chantier Chibougamau. A very special thanks goes to Julie Frappier and William Munoz and the fellows of their group to provide the CLT panels so that the tests on CLT can finally be done. Thanks Mr. Sylvain Gagnon for providing their laboratory for the tests and thanks Mr. Anes Omeranovic for mounting the specimens so that the tests could be carried out. I want to express my deep gratitude to Dr. Lin J Hu. She always gives me the insightful suggestions and encourages me at the most difficult moment during this research. Dr. Jian H Zhou is acknowledged for his suggestions which inspired me to go further in the research. A word for thanks to my co-author Dr. Juan Negreira for his generous help and the reviews in particular. I am also pleased to extend my greetings to the colleges from the University of Québec at Chicoutimi and Lund University. Thanks to all the professors at Lund who have given me useful suggestions.

Jie Zhang and Jing Li, thank you for your company during my stay in Sweden and also for telling me how to face challenges in life. Without you, the journey would not have been as pleasant.

A special thanks to my uncle, Rong W Qian, for his support. He is always reachable whenever I need a talk. Finally, I would like to thank my parents for their love, support, and understanding throughout my life.

Table of Contents

PUBLICATIONS

Peer-reviewed Journal Articles

1. Qian, C., Ménard, S., Bard-Hagberg, D., Kouyoumji, J. L., & Negreira, J. (2019). Calibration of the ISO tapping machine for finite-element prediction tool on a wooden-base floor. *Building Acoustics*. https://doi.org/10.1177/1351010X19855227. Impact factor: 0.77

2. Qian, C., Ménard, S., Bard, D., & Negreira, J. (2019). Development of a vibroacoustic stochastic finite element prediction tool for a CLT floor. *Applied Sciences (Switzerland)*, *9*(6), [1106]. https://doi.org/10.3390/app9061106. Impact factor: 1.06

3. Qian, C., Ménard, S., Bard-Hagberg, D., Kouyoumji, J. L., & Negreira, J. Development of a numerical model for predicting low-frequency dynamic behavior of a floating timber-concrete floor. To be submitted.

Conference Articles and Presentation

1. Qian, C., Ménard, S., Bard, D., & Negreira, J. (2018). Description and calibration of the ISO tapping machine in numerical impact sound predictive tools. In *47th International Congress and Exposition on Noise Control Engineering (INTERNOISE 2018).*

2. Qian, C., Ménard, S., Bard, D., & Negreira, J. (2019). Development of stochastic finite prediction element model for CLT floors. In *26th International Congress on Sound and Vibration (ICSV 2019).*

3. Qian, C., (2019). Development of a numerical prediction model for impact sound insulation performance in wooden buildings. *Woodrise 2019.*

LIST OF TABLES

LIST OF FIGURES

LIST OF ABBREVIATIONS

CLT	Cross-Laminated Timber
NLT	Nailed-Laminated Timber
EWP	Engineered Wood Product
EMA	Experimental Modal Analysis
FEM	Finite Element Method
SEA	Statistical Energy Analysis
FRF	Frequency Response Function
NRFD	Normalized Relative Frequency Difference
MAC	Modal Assurance Criterion
PDF	Probability Distribution Function
ISDE	Itô Stochastic Differential Equation
MHA	Metropolis-Hastings Algorithm

LIST OF SYMBOLS

$\sigma_{i,j}$	Stress [Pa]
$\varepsilon_{i,j}$	Strain
E_{ij}	Young's modulus [Pa]
G_{ij}	Shear modulus [Pa]
ν_{ij}	Poisson's ratio
F_n	Fourier coefficient
ω_n	Angular frequency [rad/s]
I	Momentum [kg m/s]
v_0	Initial velocity that the hammer strikes the floor [m/s]
f_0	Resonance frequency of the floating floor [Hz]
s	Dynamic stiffness per unit area of the resilient layer [Pa]
ρ_i	Mass per unit area of the upper and structural slabs [kg/m^3]
f_{sim}	Simulated eigen-frequency [Hz]
f_{mes}	Measured eigen-frequency [Hz]
Φ_i^{sim}	Simulated eigen-vector
Φ_j^{mes}	Measured eigen-vector
A_i	Accelerations of the floor at point i [m/s^2]
FRF_{i_j}	Frequency response function linked to point i and j

F_i	Force generated by impact hammer at point i
c_i	Set of random coefficients that can be described by its PDFs
$\boldsymbol{C}$	Random elastic tensor
$\boldsymbol{E_i}$	Tensor basis of the random elastic tensor $\boldsymbol{C}$
$\boldsymbol{a}$, $\boldsymbol{b}$, and $\boldsymbol{c}$	Unit orthogonal vectors
$\otimes$	Kronecker product
$P_{\boldsymbol{c}}(d\boldsymbol{c})$	unknown probability distribution
$S(p)$	Entropy
λ^i	Lagrange multipliers
$\boldsymbol{g}(\boldsymbol{c})$	Mapping of $\boldsymbol{c}$
$\Phi(\boldsymbol{u},\boldsymbol{\lambda})$	Potential function
$\boldsymbol{U}(r), \boldsymbol{V}(r)$	Markov stochastic process
Θ, T, P	Probability space
$\boldsymbol{W}(r)$	Normalized Wiener process
$\boldsymbol{B}_\lambda$	Random variable
r_o	Iteration step
f^{target}	Target vector
$p(f)$	Pressure radiated by a point
ρ_0	Air density [kg/m^3]
q_0	Volume velocity [m^3/s]
k_0	Wavenumber in the air [rad/m]

r	Distance between the point source and the receiving point [m]

CHAPTER 1 GENERAL INTRODUCTION

1.1. Introduction

The market share of timber constructions for industrial and residential multi-storey buildings has been rapidly increasing during the last decades [1]. Recent research points out that wooden construction innovations can reduce carbon dioxide emissions and fossil fuel consumption [2-7]. This renewable material consumes relatively low energy to be produced and has fewer side effects on the environment, such as water pollution and green gas emission. Light in weight, high degree of prefabrication, fast transportation, low storage costs, and easy to assembly, all these outstanding advantages lead to a steady increase of wooden constructions in market share [8]. Moreover, wooden construction is a great interest in Canada due to its abundant wood resource. The Canadian forest industry contributes billions of dollars each year and no nation derives a more net benefit from trade in forest products than Canada [9].

Today, massive timber panels, such as Cross-Laminated Timber (CLT), Nailed-Laminated Timber (NLT), etc. become the popular alternative of concrete in mid- and high-rise constructions due to their optimized properties which meet the specific needs of the structural design. Massive timber panels can be used as load-carry elements, such as walls and floors in constructions because of their high strength and dimensional stability [10]. Among all massive timber panels, CLT is one of the most popular massive timber panels due to its low air permeability and distinctive specific storage capacity for humidity and thermal energy. Low mass allows CLT to construct on the soil with weak load-bearing properties. It is suitable for the upgrading of existing buildings [11]. CLT continuously breaks the limits of high-rise timber buildings, such as Condos Origine and Brock Commons, shown in *Figure 1.1*.


(a) (b)

Figure 1.1: (a) Condos Origine, Québec City, Canada. (b) 18-storey timber Brock Commons tower, Vancouver, Canada. (Source: Woodskyscrapers)

However, acoustic insulation is a challenge for multi-storey wooden buildings, especially low-frequency noise. Complaints about the noise coming from neighbors, traffic, installation, etc. are raising from the inhabitants in these wooden buildings, even these wooden dwellings have already fulfilled the current acoustic insulation standards. According to the ISO standards, the frequency range of the impact sound measurement standards begins from 100 Hz and up to 3150 Hz [12, 13]. Like Sweden, the frequency range of evaluation can be decreased to 50 Hz. However, the first several eigen-frequencies of floors which cause the most significant annoyance, like foot-fall noise, are lower than 50 Hz [14]. But these frequencies are excluded from the evaluation procedures. As a consequence, even though the wooden constructions fulfilled the requirements of standards, the low-frequency issue isn't really addressed, resulting in many complaints coming from the residents [15].

To address this problem, it is always desirable to know the acoustic insulation performance of the structure element before the construction in order to prevent the costly changes after the erection of the building. Today most prediction approaches are based on empirical engineering experiences and tests. But in general, the tests could be expensive and time-consuming. The results given by the tests in the laboratory do not always correlate with in-situ measurements. In the laboratory, the flanking transmissions are removed, whereas, in-situ, the flanking transmission can play an important role in sound insulation, which can result in a degraded sound insulation performance. Prediction models, in spite of being highly useful for the design of new buildings, are still very lacking today [14]. Gaining an adequate understanding of the dynamic behavior of wooden construction would be one important step towards a reliable prediction model. In this report, the dynamic behavior of the bare CLT floor and the CLT-concrete floor were investigated. The corresponding models were established based on the experimental results to simulate the dynamic behavior of the floors.

1.2. Problem Statement

From the practice, it is proven that dynamic behavior of floor, especially the impact sound at low frequencies, like foot-fall noise [16-19], is an important consideration in the design phase and neglecting the dynamic behavior of floor will degrade the acoustic insulation for occupants, especially for who lives in the wooden buildings. The impact sound transmission is illustrated in Figure 1.2. A well-known example [20] in North American is that one supposed to be a “luxury” condos in the San Francisco Bay Area received an $80 million class-action suit against the developer. One of the major claims is the footfall noise coming from the wooden ceiling. From this example, we can see that more attention should be paid to the low-frequency noise in wooden construction.

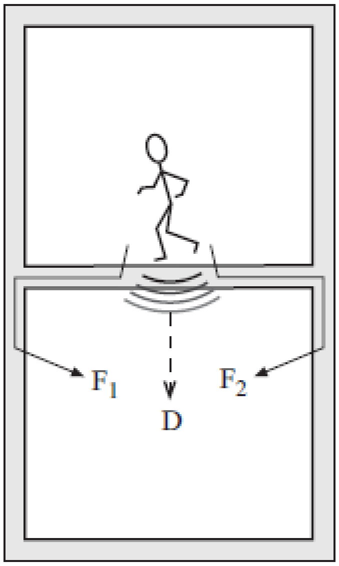

Figure 1.2: Impact sound transmission. “D” denotes direct transmission whereas “Fi” indicates the different flanking paths involved [12].

In recent years, many research found that lightweight buildings do not behave like heavy constructions [21-30]. Lightweight buildings perform better acoustic insulation in mid- and high-frequency range comparing to heavy constructions, whereas, the low-frequency acoustic insulation performance should be further investigated [31]. But current standards, such as ISO 10140 and ISO 717, do not evaluate the sound insulation below 100 Hz (optionally below 50 Hz). In the recent research[32], it was found that the correlation determination between $L'_{n,w} + C_{I,50-2500}$ and the subjective evaluation is only 32%, whereas, when the frequency band of $L'_{n,w} + C_{I,20-2500}$ is extended to 20 Hz, the corresponding correlation is remarkably increased (up to 74%). Furthermore, from the perspective of the FEM modelling, the lack of reliable input parameters of the material and different construction techniques make the high sound insulation quality of the wooden buildings more difficult to be attained [33]. Wood being a natural material has more uncertainties comparing to a homogenous artificial material. So far, there is no accurate calculation method for the acoustic performance of lightweight buildings [6, 14, 34]. The product development is mainly based on the empirical experience [35]. In order to improve the impact sound insulation of wooden buildings, it is desirable to know more knowledge of low-frequency vibro-acoustic behavior of wooden buildings. And reliable prediction tools are in need to prevent expensive over-designed acoustic solutions before the constructions.

1.3. Objectives

The main objective of this project is to try to gain the knowledge of the vibro-acoustic behavior of the cross laminated timber-concrete floor and to develop a low-frequency impact sound prediction model for this type of floor. The prediction of an acoustic pressure field can be divided into three steps: 1) Predicting the force caused by the impact source; 2) Predicting the transmission of vibrations from the location of the impact to the receiving room; 3) Predicting the acoustic pressure field caused by the vibrations in the ceiling, walls, and floor of the receiving room [36]. The research scope of this thesis focusses on the prediction of the impact source and the transmission of vibrations. The prediction of the sound pressure emitted by the structure is roughly investigated under certain strict assumptions. To achieve that, the force generated by the ISO tapping machine should be characterized. After that, the dynamic response of the CLT bare floor and the CLT-concrete floor should be investigated in order to predict the impact sound afterward.

So, derived from the main objective, several specific objectives are presented in the following points:

1) Proposing a modeling method to characterize the force introduced by the ISO standardized tapping machine.
2) Gaining knowledge of the dynamic properties of the CLT bare floor and CLT-concrete floor.
3) Developing a modeling method to automate the orthotropic material calibration procedure and to quantify the uncertainties induced by the material properties.
4) Investigating the modeling method of the connections between different materials of the CLT-concrete floor and developing a FE model to make a step towards predicting vibro-acoustic behavior of the CLT-concrete floor.

1.4. Originality of the Research

Acoustic insulation is one of the main challenges of wooden dwellings, especially the low-frequency impact noise. This is due to the fact that wooden constructions respond more actively to a given input excitation comparing with heavy constructions [6]. Moreover, the various construction methods and the big variations of the material properties of wood make the acoustic performance of the wooden buildings more difficult to predict. Consequently, in some multi-storey wooden buildings, many residents perceive the impact sound as annoying noise even though these buildings have fulfilled the requirements of the regulations [25, 37-39]. Today, due to the lack of reliable input material properties of structures and knowledge of the wooden buildings, no reliable prediction model is available to estimate the acoustic performance of wooden buildings before the construction. The purpose of this research is to establish a prediction model of the floor. The vibro-acoustic behavior of the CLT bare floor and the CLT-concrete floor were obtained by means of experimental tests. Based on the dynamic response of the floors, the corresponding models were established. Modeling methods were developed to derive the force generated by the ISO tapping machine, to characterize the uncertainties induced by the material properties of CLT and to describe the connections of different layers of the floating floor in the FE model. By integrating all the developed models, the dynamic response of the floor can be modeled, and subsequently, the accelerations can be calculated. The pressure radiated by the floor can be potentially determined under certain assumptions since the pressure is proportional to the accelerations of the floor [40]. The frequency band of the measurements as well as the corresponding models was enlarged up to 200 Hz. Furthermore, through the difficulties met in the measurement phase, the appropriate simplification of the boundary condition was proposed. And the adequate boundary condition modelling was found. All in all, this research is one step towards a reliable and accurate low-frequency impact sound prediction model.

1.5. Methodology

To achieve the goals of this project, the research was carried out through three steps, as shown in Figure 1.3. We begin with force characterization. The force generated by the tapping machine is described by means of the acceleration and dynamic response of the floor. Then, the CLT is calibrated by using the stochastic approach. Based on the methods developed, the dynamic behavior of the CLT-concrete floor is modelled.

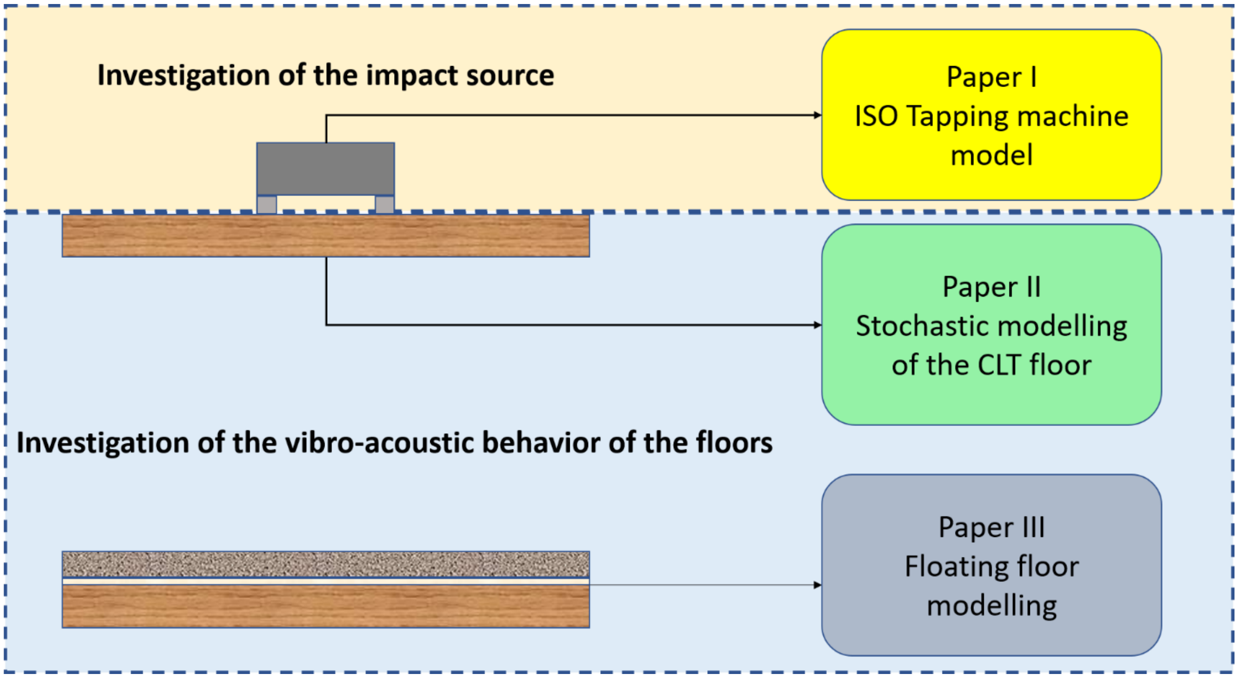

Figure 1.3: Structure of the research.

To establish an impact sound prediction model, the force generated by the ISO tapping machine should be characterized. The dynamic properties (eigen-frequencies; eigen-modes; damping ratios) of the base floor (the CLT floor) were extracted from the experimental tests. The base floor model was established according to the measurement results. Then, the accelerations of the floor generated by ISO tapping machine were recorded in order to derive the input force yielded into the system. By integrating the force into the numerical model of the floor, the simulated accelerations were compared with the measured ones to validate the force modeling method. In order to facilitate the calibration procedure of the CLT floor and to quantify the uncertainties induced by the material properties of CLT, the stochastic model to describe the orthotropic material parameters was introduced into the model. The reference data to validate the model was the dynamic information of the floor obtained from the previous measurements.

The vibro-acoustic behavior of the CLT-concrete floor was studied in the final phase. The experimental tests were performed on this floating floor to obtain measurement data to validate the FE model afterward. The connections between different materials in the floating floor was studied. The material parameters of the materials on the floor were calibrated and validated by comparing the simulation results with the experimental data. An initial calculation of sound generated by the tapping machine and radiated by the floor was calculated under certain strict assumptions.

1.6. Thesis Organization and Relationships between the Different Chapters

This thesis consisting of six chapters is designed as a collection of the articles which cover the content of the work. To achieve the ultimate goal of this research, different studies were carried out. The 1st chapter dedicates to a general introduction of this thesis. The literature review is presented in the 2nd chapter. The 6th chapter is a general conclusion and the perspective for the future work.

To develop an impact sound prediction model, the first question is how to model the source of the impact sound. In the 3rd chapter, the force generated by the ISO tapping machine, which is employed as the impact source in the ISO standards, is studied. An indirect method of simulating the force is presented in the 3rd chapter.

During the development of force modeling, it was found that the model of the base floor where the ISO tapping machine was placed on can have an influence on the accuracy of the force modeling. So, in the 4th chapter, a stochastic modeling approach was developed to quantify the uncertainties induced by the material properties of the structure and to automate the calibration procedure. The model validated was based on the experimental results.

The 5th chapter aims at investigating the modeling approach to characterize the dynamic behavior of the CLT-concrete floor. In the final section of this chapter, an initial try to calculate the pressure emitted by the floor was made by employing the modeling methods in the previous chapters.

CHAPTER 2 LITERATURE REVIEW

In this chapter, the context of the sound insulation in wooden buildings is given in the first section. A short introduction to wood as the construction material is presented. The modeling approaches, the statistical energy analysis (SEA) and the finite-element method (FEM) are briefly discussed. Following this, the literature review related to the research carried out in this project is presented in the last section.

2.1. Sound Insulation in Wooden Buildings

Acoustics includes sound and vibration [15]. Due to the variability and the intrinsic features of wood, wooden constructions are vulnerable to the sound insulation compared to the heavy constructions, like concrete buildings. Sound insulation in dwellings, generally, encompasses two different kinds: airborne sound insulation and impact sound insulation.

The current solutions to estimate the sound insulation performance of wooden buildings in the early design phase are based on either practical tests or employing the existing prediction methods. However, using the test to evaluate the acoustic performance of the constructions is not only expensive but also time-consuming. Meanwhile, the obtained results may not be useful just because of a slight change in construction. There exist some empirical models and prediction methods, like ISO 12354 [41-44], which estimates the airborne sound and impact sound performance by taking into account the flanking transmission. These standards are base on the Statistical Energy Analysis (SEA) which requires a diffuse vibration field. However, due to the higher internal loss of lightweight buildings, the reverberation vibration field is difficult to achieve, especially in the low-frequency range, because of the lower modal density [45]. As a consequence, the uncertainties of the prediction increase in the low-frequency range [46]. Furthermore, the inhomogeneity and anisotropic of lightweight elements are not considered in the calculation standards [15] Therefore, reliable prediction tools are needed to avoid severe and costly changes in the design phase of wooden buildings.

2.1.1. Airborne Sound

Airborne sound can be described as sound waves generated by a sound source reaching a building structure, then causing vibration of structure which is transmitted to the other side of the structure and radiated out of the structure to create pressure variation in the air on the other side of the structure. Subsequently, the noise is created on the other side of the building element. The airborne sound transmission is described in Figure 2.1.

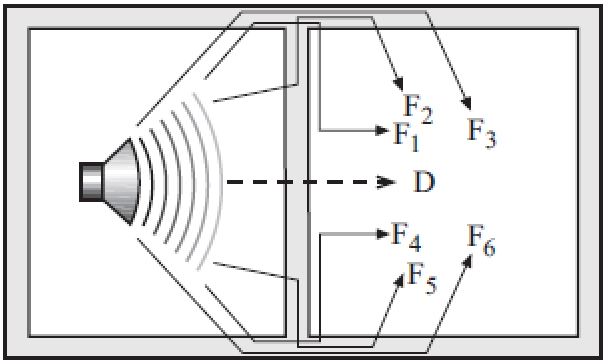

Figure 2.1: Airborne sound transmission. “D” denotes direct transmission whereas “Fi” indicates the different flanking paths involved [12].

Mass per unit area is an important factor for the airborne sound insulation in wooden construction. Because of the low density of the wood, wooden dwelling could be prone to airborne sound issues, especially in the low-frequency ranges. Modern audio equipment, like HiFi system and appliances, are the typical airborne sound sources that can potentially generate annoying noise far below 100 Hz. Some Nordic countries have extended the frequency range of building code down to 50 Hz to dealt with the impact sound insulation issue. The airborne sound is out of the scope of this thesis and it will not be discussed in this work.

2.1.2. Impact Sound

The structural-acoustic process can be divided into four steps, shown in Figure 2.2. The first stage is the generation of oscillation. The second stage is the transmission which encompasses the transfer of oscillation energy from the mechanisms of generation to a structure. The third step is the distribution of energy throughout the oscillated structure system. This procedure is called propagation. The last one is radiation. Any structural part vibrating in the air passes on power to the air, and that is perceived as an audible sound [40].

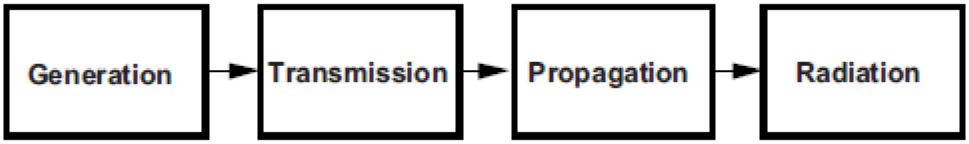

Figure 2.2: Structural acoustic process [40].

Airborne sound and impact sound can be transmitted into the receiving room through the direct and flanking transmission. The waves generated on the top of the floors can propagate through the load-bearing walls and radiate into the receiving room, resulting in louder noise compared to the noise only directly coming from the ceiling. The model development reported in this thesis is only one step towards an applicable prediction model. So, this work only focusses on the direct sound transmission, and the flanking transmission is beyond the scope of this thesis.

Impact sound has been reported as the most critical sound source in dwellings [47]. It is a long-standing problem needed to be tackled in the multi-family buildings, especially for wooden constructions [20, 48]. The low-frequency impact noise, typically generated by footfall or dropped object, is one of the most annoying impact sources in the wood-frame buildings [14, 15, 20, 25, 28, 32, 35, 48-53]. To dealt with that, different solutions are developed to decrease the impact sound transmission. These solutions are only capable of reducing impact noise in the mid- and high-frequency range; they fail to provide satisfactory performance in the low-frequency range [15].

Although the wooden dwellings are fulfilled the standard requirements, the complaints have still risen from the occupants in this type of buildings, especially the low-frequency noise. It was found that these standards do not function as they should be in wooden constructions since wooden buildings behave differently in low-frequency range other than concrete constructions. Furthermore, the ISO standards employ a tapping machine as the excitation source. The small hard masses of the tapping machine can hardly mimic the human walking without hard shoes, which can have no-linear effects. Moreover, the low-frequency impact sound evaluation is underestimated in the single number ratings defined in standards. This low-frequency issue could be partly resolved by introducing the low-frequency adaptation term. Recent research [25, 32] reveals that there still exist mismatches between the subjective and the objective ratings, even with the adaptation terms. It was demonstrated that when the evaluation frequency range is enlarged down to 20 Hz, the correlations between the subjective ratings performed by inhabitants in wooden dwellings and the objective ratings performed by ISO standards can be largely improved. Because the first several eigen-frequencies of floor containing the most of vibration energy and believed to cause the most annoyance are lying under 30 Hz [54]. It is recommended that the impact sound evaluation should be extended to 20 Hz in order to achieve a higher acoustic quality of dwellings.

All in all, today's standards are needed to be revised to provide more general and robust methods to facilitate acoustic comfort achievement in wooden buildings. Nevertheless, regarding the practical and juridical reasons, the wooden construction industry is still following the current standards even though the low-frequency sound evaluation, which is essential to achieve high acoustical quality in wooden dwellings, is excluded from the regulations. Thus, this thesis mainly focusses on gaining knowledge about the generation of the impact sound as well as the dynamic response of the excited wooden structures in the low-frequency range.

2.2. Wood as a Construction Material

2.2.1. Mechanical Properties of Wood

Wood has been used as a building construction material throughout history because of its unique mechanical and machining characteristics [10]. Wood is usually considered as a lightweight construction material since it has the high strength-to-weight ratio properties compared to the conventional artificial construction materials, such as concrete or steel. With the same load-bearing capacity, wooden structures are lighter than concrete structures in general.

As a natural material, mechanical properties of wood are governed by the direction of fibers and the annual rings of the trees, meanwhile, they are also affected by the moisture contents and temperature [55]. Wood can be modeled in micro-scale, meso-scale as well as macro-scale levels depending on different purposes. Generally, wood is considered as homogenized cylindrical orthotropic structure, shown in Figure 2.3 (a), which is characterized by three mutually perpendicular axes, longitudinal (L), tangential (T) and radial (R). However, when the cross-section of the wooden structure is small or locates far from the pith of the trunk, the curve effect of the annual rings could be neglected [56]. For the sake of simplicity, wood can be described by the rectangular orthotropic model, shown in Figure 2.3 (b). The vibration of structures induced by human activities is very slight, and thereby wood can be modeled as a linear elastic and homogenous material at the macro-scale level in this thesis.

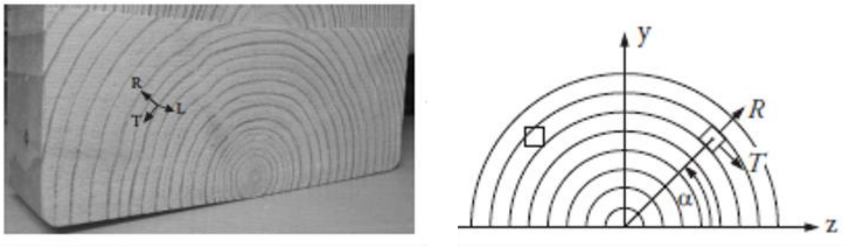

(a) (b)

Figure 2.3: (a) Cross-section of a raw wood log; (b) Rectangular orthotropic wood model [14].

The constitutive behavior of the structure can be described by Hook's law under the linear elastic assumption. The stress can be represented by nine stress components, $\sigma_{i,j}$, with $i,j = 1,2,3$. Same as stress, the strain can also be represented by nine strain components, $\varepsilon_{i,j}$, with $i,j = 1,2,3$. Regarding the symmetrical plans of the strain and stress in the three mutually perpendicular directions, the orthotropic materials can be expressed as:

$$\begin{Bmatrix} \varepsilon_1 \\ \varepsilon_2 \\ \varepsilon_3 \\ \gamma_4 \\ \gamma_5 \\ \gamma_6 \end{Bmatrix} = \begin{bmatrix} S_{11} & S_{12} & S_{13} & 0 & 0 & 0 \\ S_{12} & S_{22} & S_{23} & 0 & 0 & 0 \\ S_{13} & S_{23} & S_{33} & 0 & 0 & 0 \\ 0 & 0 & 0 & S_{44} & 0 & 0 \\ 0 & 0 & 0 & 0 & S_{55} & 0 \\ 0 & 0 & 0 & 0 & 0 & S_{66} \end{bmatrix} \begin{Bmatrix} \sigma_1 \\ \sigma_2 \\ \sigma_3 \\ \tau_4 \\ \tau_5 \\ \tau_6 \end{Bmatrix} \tag{2-1}$$

In this work, the engineer constants are employed in the FE modeling software to model the wooden structure. For the sake of simplicity and modeling concerns, the Hook's law of orthotropic material expressed with the help of the engineer constants is shown in Equation (2-2).

$$\begin{Bmatrix} \varepsilon_1 \\ \varepsilon_2 \\ \varepsilon_3 \\ \gamma_4 \\ \gamma_5 \\ \gamma_6 \end{Bmatrix} = \begin{bmatrix} \frac{1}{E_1} & -\frac{\nu_{21}}{E_2} & -\frac{\nu_{31}}{E_3} & 0 & 0 & 0 \\ -\frac{\nu_{12}}{E_1} & \frac{1}{E_1} & -\frac{\nu_{32}}{E_3} & 0 & 0 & 0 \\ -\frac{\nu_{13}}{E_1} & -\frac{\nu_{23}}{E_2} & \frac{1}{E_3} & 0 & 0 & 0 \\ 0 & 0 & 0 & \frac{1}{G_{23}} & 0 & 0 \\ 0 & 0 & 0 & 0 & \frac{1}{G_{13}} & 0 \\ 0 & 0 & 0 & 0 & 0 & \frac{1}{G_{12}} \end{bmatrix} \begin{Bmatrix} \sigma_1 \\ \sigma_2 \\ \sigma_3 \\ \tau_4 \\ \tau_5 \\ \tau_6 \end{Bmatrix} \tag{2-2}$$

Wood as a natural material has imperfections, such as the knots or the growth ring irregularities. These natural defects create the variations of elastic constants not only in the different species of wood but also in the nominally identical wooden structures, as well as in single one log. Subsequently, they result in the different dynamic behavior of the wooden structures. As a consequence, the mechanical properties of wood (even with the same species of wood) are difficult to quantify and the calibration of dynamic properties of wooden structures is always a challenging task. This variability of mechanical properties can be addressed by using the probabilistic method, such as stochastic approach [57]. More details are presented in chapter STOCHASTIC CALIBRATION PROCEDURE. The material properties of the CLT panel can be derived from the dynamic response of the structure by conducting the modal testing [58]. But this method can only determine three parameters. They are respectively Young's moduli in principle and vertical directions (E_x and E_y) as well as one shear modulus (G_{XY}). Nevertheless, a 3D finite-element model demands six input parameters (E_x, E_y, E_z and G_{xy}, G_{yz}, G_{xz}). In this work, we didn't employ this method to acquire the material properties of the CLT panel.

2.2.2. Cross-Laminated Timber

Nowadays, massive timber panels, like CLT, becomes more popular in the mid- and high-rise wooden buildings. Owing to their high strength and dimensional stability, massive timber panels can be a substitute for concrete, masonry, and steel to make wood skyscrapers possible. In addition to natural and sustainable characteristics of massive wooden panels, CLT gains more attention due to its outstanding load-bearing in- and out-plan performance and a high degree of prefabrication, as well as its low air permeability, specific storage capacity for humidity and thermal energy characteristics. The conception idea of CLT was initially developed from the 1970s to the 1980s in Switzerland, Austria, and Germany, and it took twenty years until the first technical approval made in 1998 [11]. CLT panels consist of several layers of boards, orientated 90 degrees with each other, and glued together on their broad faces [59]. The CLT panel is shown in Figure 2.4. The narrow faces of the adjacent board can be glued, known as edge bonding, or left without bonding even with small air gaps. There has been a large number of global activities being carried out in production, use, and standardization all over the world, like Scandinavia, Austria, Canada, the United States, New Zealand, Japan, and China. CLT has been applied to high-rise buildings, such as an 18-storey student residence in Vancouver, Canada. It is also one of the primary objective materials in this work.

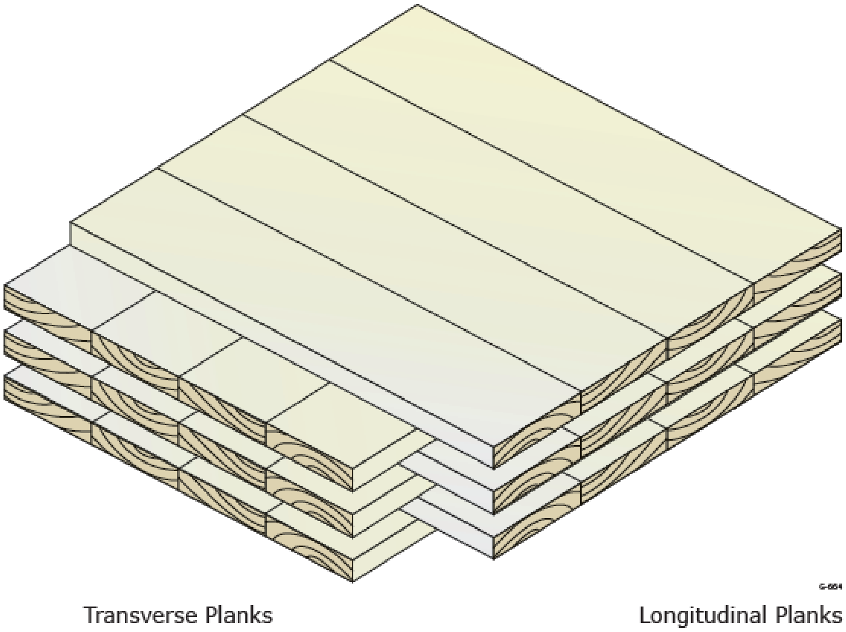

Figure 2.4: CLT panel configuration [59].

As an essential indicator of quality control, elastic properties of CLT are considered as the checking parameters for the serviceability limit designs which govern the design of structural assemblies built with mass timber panels. It has a paramount influence on the dynamic response of CLT panels. Although the elastic properties of CLT can be obtained through either static or dynamic evaluation methods [10, 58, 60], these obtained elastic properties can not give a promising result without repetitive calibrations, when dealing with the dynamic response simulations of CLT panels. Since the lay-up, raw material, and manufacturing parameters can have an impact on the properties of a full-sized wood-base panel. Consequently, it is always necessary to calibrate the material properties to investigate the dynamic response of wood-based structures. In general, the wood-based structure is modeled as transversely isotropic material [61, 62], but the rolling shear modulus plays an important role in the effective bending stiffness of the plate. So, in the research reported here, the CLT panel is modeled by an orthotropic material instead of a transversely isotropic material.

No matter the designers or the inhabitants show a high expectation of the acoustic comfort achievement in timber dwellings [63]. However, the wooden buildings are facing the challenge coming from the low-frequency noise [25, 32]. The CLT due to its low volume density and high stiffness property, the bare CLT floor could not provide sufficient sound insulation to meet the sound insulation requirement, so, it would be necessary to gain more knowledge of the CLT acoustic properties and to develop the solutions to increase its sound insulation performance [64, 65].

On the one hand, the different types of measurements were carried out to seek for the solutions. It is known that there is no reference curve in the standard ISO 10140 and ISO 717 [13, 66] for the CLT panel to evaluate the impact sound insulation improvement. But the experimental tests [67] reveal that the rating of the sound insulation performance of the topping highly depends on the shape of the reference curve. In [67], a reference curve was developed for the CLT floor. But more data are needed to justify the reliability of the proposed curve. The CLT constructions are also compared to the other kind of timber buildings. In a recent research [68], it was found that the impact sound insulation of the CLT construction has a larger variation in low frequency range (50-100 Hz) compared to the prefabricated volume-based building, whereas, the CLT construction has a better impact sound performance at frequencies higher than 400 Hz. Few years later, in another work [65], the impact sound tests were conducted on the CLT system and the timber-concrete composite system. Different configurations of floor were combined with the CLT system or the timber-concrete composite system. The experimental results show that the timber-concrete system has a better sound reduction performance than the CLT system in general.

On the other hand, efforts were made to predict the acoustic performance of the CLT construction. Kouyoumji et al employed the Statistical Energy Analysis to predict the acoustic insulation of the CLT buildings [69]. Also, the prediction methods were developed for calculating the sound radiation efficiency of the CLT constructions [70, 71]. Meanwhile, the parallel work was carried out on utilizing the measurement data to predict the apparent impact and airborne sound of the CLT construction by taking into account the flanking transmission [72, 73]. The prediction method ISO 12354 was chosen in these works because the CLT is close to the homogeneous materials, such as concrete, for which the standards are initially designed. This prediction model demands the direct transmission quantities (R_w, $L_{n,w}$), measured in laboratory condition according to ISO 10140 series, the vibration reduction index K_{ij} measured according to ISO 10848-1 as well as the geometrical dimensions as input data. It is relatively easy to find direct transmission quantities of CLT. However, only limited vibration reduction index of CLT can be found in the research [73-75]. Although extensive investigations have been carried out on the acoustic performance of the CLT panels, the available database for the standardized prediction model is till lacking compared to other construction systems, both heavy and lightweight [76]. Besides the prediction standards, empirical equations are proposed to estimate the impact sound insulation of the bare CLT floor [77]. It can be seen that the acoustic prediction of prefabricated construction systems like CLT using standardized methods is not entirely accurate [78].

From the noise control perspective, it necessary to know how the vibrating structure radiates the sound. The sound radiation efficiency is a physical quantity to define the capacity of a structure to radiate the sound, which is defined as:

$$\sigma = \frac{W}{\rho c S \overline{|v|^2}/2}, \tag{2-3}$$

where W is the power radiated from a structure with surface area S and vibrating with the spatially averaged, mean-square velocity $|v|^2$. This radiation efficiency compares the power radiated by an object to a rigid piston of the same area. It should be noticed that when the flexural wavelength of the structure is smaller than the acoustic wavelength in the air, only a near field is formed. The acoustic wave decays fast and it couldn't propagate into the far field. In this case, the velocity of the floor can be large, whereas the radiation efficiency can be low, which means little sound radiated in the receiving volume. The corresponding frequency is called coincident frequency [40]. The CLT panel has two coincident frequencies, since the CLT panel exhibits a highly orthotropic behavior and the bending velocity is different in the two principal directions.

However, there is no standardized method to measure the sound radiation efficiency, neither in laboratory condition nor in-situ [71]. The mean square velocity of the structure can be measured by using a scanning laser vibrometer or the accelerometers. The power radiated from a structure, W, is not directly measurable. But it can be determined from the other quantities, such as the sound pressure or measured complex vibration velocity [79]. These indirect approaches are either suitable for the higher frequency range or have certain assumptions, like the evaluated structure should be surrounded by an infinite rigid baffle. All these conditions imply that it is not evident to measure the sound radiation efficiency. On the other hand, the prediction of the sound radiation efficiency is also a demanding task. In a recent study [70], the radiation efficiency of a 4-side simply supported CLT panel is predicted by two different approaches. One modal approach is applicable in the frequency band where the continuous distribution of modes should be satisfied. Another more detailed and more accurate analytical approach which can even calculate the radiation efficiency under the critical frequency is presented. This method demands a perfect simply supported boundary condition which is difficult to attain. These two methods can provide a reasonably good agreement with the experimental results in general, even though some discrepancies can be observed in the low frequency range or around the critical frequency. It can be seen that the measurement and prediction of the sound radiation efficiency are not straightforward. But this acoustical descriptor can be an important input data for the building acoustic prediction models [70, 80, 81].

In the frame of this work, the dimension of the console of the ISO standardized step sound laboratory where the tests in this work carried out is 3×4m^2. The industrial company can not provide a CLT panel of this specific dimension. As a consequence, two CLT panels of 1.5×4m^2 were connected together in order to fill in the testing room. But this connection and boundary conditions in the laboratory made the vibration modes difficult to be extracted. The modes are considered as reference to calibrate the models. To address this problem, one single leaf of CLT panel was simply supported on two shorter edges. So, we have only investigated the dynamic response of the CLT panel and the CLT-concrete floor under 2 shorter side simply supported boundary condition. It is necessary to calculate the sound radiation efficiency which characterize the relation between the surface velocity of the structure and the sound radiated into the lower volume. But before that, the boundary conditions in the laboratory and connections between two CLT panels should be addressed in the model. Then the accuracy of surface velocity given by the model should be justified. Finally, the measurement and calculation of the sound radiation efficiency can be carried out. Due to the limited time, in this work, we can only investigate the dynamic response of the floors, and we tried to calculate the surface velocity and pressure radiated by a 1.5×4m^2 under some strict assumptions. It is only one step towards a well-established prediction model.

2.3. Modelling Approaches and Measurement Method

2.3.1. Modelling Approaches

Although there is a great need of a prediction tool in the early design stage, due to the lack of the reliable material properties input and the lack of dynamic behavior of wooden construction knowledge, reliable prediction tool is still in the margin. Most of the current prediction models are based on two different methods.

One method is the SEA. The SEA method was initially developed to predict the vibration or noise level for a complex structure. It is an energy-based analysis method for vibroacoustic problems. For the steady-state conditions, a power balance is established between different subsystems. The input energy is either dissipated within the subsystem or coupled to other subsystems where it is dissipated or radiated to the acoustic field. Average vibration and sound pressure levels are derived from the subsystem energies with a minimum level of modelling complexity and detail. However, only average vibration and noise levels in each subsystem can be obtained due to the assumption of the equal distribution of energy over space in each subsystem [82, 83].

Although the SEA method has many advantages, such as low-cost computation time, still, the drawbacks to predicting the vibroacoustic behavior of wooden construction are obvious. Neither frequency distribution nor spatial energy distribution in subsystems could be obtained. As the energy is equally distributed in each resonant mode of the subsystem. Furthermore, the SEA method is more suitable for homogeneous constructions, such as concrete and masonry buildings. It is easier to predict the acoustic performance in mid- and high-frequency range because of the higher modal density. But in the low-frequency range where the more severe acoustic issues for wooden construction locate, the SEA method fails to give a satisfying answer. For example, the ISO 12354 based on the SEA method is a prediction standard taking into account the first order flanking transmission. This standard only considers the resonant transmission. It implies that this standard is not suitable for the predictions lower than the critical frequency. However, for the wooden construction, low-frequency is the most important frequency range of interest [45].

Another general method with a high resolution is the Finite Element Method (FEM). The FEM is a computer-aided mathematical technique for obtaining the approximate numerical solutions of the abstract equations of calculus that predict the response of physical systems subjected to external influences [84]. The governing equations can be differential equations that describe many kinds of engineering problems. The governing equations hold a certain region which will be divided into smaller regions, called elements. It should be noticed that the adjacent elements should not be overlapped nor have gaps between them. Then in each element, the governing equations are transformed into algebraic equations, called element equations. The terms in the element equations are numerically evaluated then the resulting numbers are assembled into a matrix depending on the geometry. After applying the boundary conditions, an approximate solution should be derived from the equation systems. But sometimes due to these enormous details, the computation time could become unreasonable. So how to include enough details to give a reliable result meanwhile to keep the computation time in an acceptable range should also be taken into consideration [84]. In [85, 86], the 5-ply and 7-ply CLT panels were modelled as a single segment by shell elements or solid elements. The mesh convergence study was performed to determine the size of the mesh. The simulated eigen-frequencies were compared with the measured ones. It can be seen that higher the frequency is, larger the discrepancies are. Furthermore, the highest frequency of interest is 100 Hz. There is no comparison of the FRF which is important for calculating the accelerations of the floor.

In this project, FEM is chosen to be the main method to develop predictive tools. A commercial software, Abaqus, developed by Dassault Systèmes [87], is mainly used in this thesis.

The reason to choose the FEM is that compared to other methods, FEM is more commercially developed, and a well-established computer program is a more friendly use for consulting companies and for the industry. Furthermore, compared to SEA, FEM is able to include more details of the structure and to give robust results in the low-frequency range, which is paramount for wooden constructions.

2.3.2. Measurement Method

Experimental Modal Analysis (EMA) is the processes involved in testing components or structures to obtain a mathematical description of their dynamic or vibration behavior. A modal test is undertaken in order to obtain a mathematical model of the structure. In general, a modal test is performed to obtain a mathematical model of a structure, but there are different subsequent uses of different purposes [88]:

1) Model validation. It is the most commonly used application in measuring a structure's vibration properties to compare with the corresponding data produced by a FE model or other theoretical model. Validating the major eigen-frequencies and mode shapes can provide reassurance of the reliability of the theoretical model before its use for predicting the response of a structure to complex excitations, such as shock, or other further stages of analysis.
2) Substructuring process. Another application is to establish a mathematical model of a component which may be incorporated with other components in a structural assembly. This is widely used in a theoretical analysis of complex structures.

3) Force determination. In many cases, the knowledge of the dynamic force causing vibration is required, but direct measurement of these forces is not practical, such as lacking the measurement equipment. One solution is to combine the response caused by force and the transfer functions of the structure to deduce the force.

Roughly speaking, EMA encompasses three main steps:

1) Experiments. The test protocol should be designed. A predefined mesh should be drawn on the structure in question to determine the positions of excitations and sensors and to record the dynamic response of the structure. The boundary conditions and acquisition parameters, like frequency band, resolution, number of recorders, window selection, etc. should be decided at this stage.
2) Data processing. After the measurements are finished, the recorded data are post-processed through fitting a mathematical expression to the measured results. This is done by minimizing the squared error between the measured data and the mathematical function. The dynamic properties of the tested structure are extrapolated from the mathematical expression.
3) Model validation. The extracted modal model should be able to represent the dynamic behavior of the structure in the studied frequency band.

In the frame of this work, the aim of carrying out EMA on the specimen is to obtain dynamic properties of the structures in order to validate models and to derive the external force through the dynamic response of the structure.

A hammer or a shaker can be used to excite the structures. Compared with the shaker, hammer testing is quick, easy, and relatively cheap. This type of excitation requires very little hardware, and the measurement time is short, and thereby, it is highly suitable for in-situ measurements. However, the input force can change depending on different operators and different locations. Sometimes, a large structure needs a high peak force to be set into motion, which may cause local damage to the structure. Thus, the hammer test is more recommended for a simple structure. Shaker test has higher repeatability of which the hammer test lacks. Furthermore, the excitation signal feed to shaker can be designed depending on different structures and different purposes of use. But the support condition of the use of shakers is more demanding. Because the force is transmitted via a connection road, called stinger, which possesses the high axial stiffness and low bending stiffness characteristics, so the stinger should keep vertical to transmit the force properly. The shaker should be mechanically isolated from the specimen like suspended on the solid ceiling in order not to affect the dynamic response of the structure [56, 89].

Regarding the available conditions of the laboratory and the time schedule of the project, the impact hammer was chosen as the external excitation for this project. The hammer reference is Brüel & Kjær, type 8208, serial No. 51994. The medium tip of the hammer was chosen since the highest frequency of interest in this research is 200 Hz. The force impulse and spectrum and the measurement set up are respectively shown in Figure 2.5 and Figure 2.6.

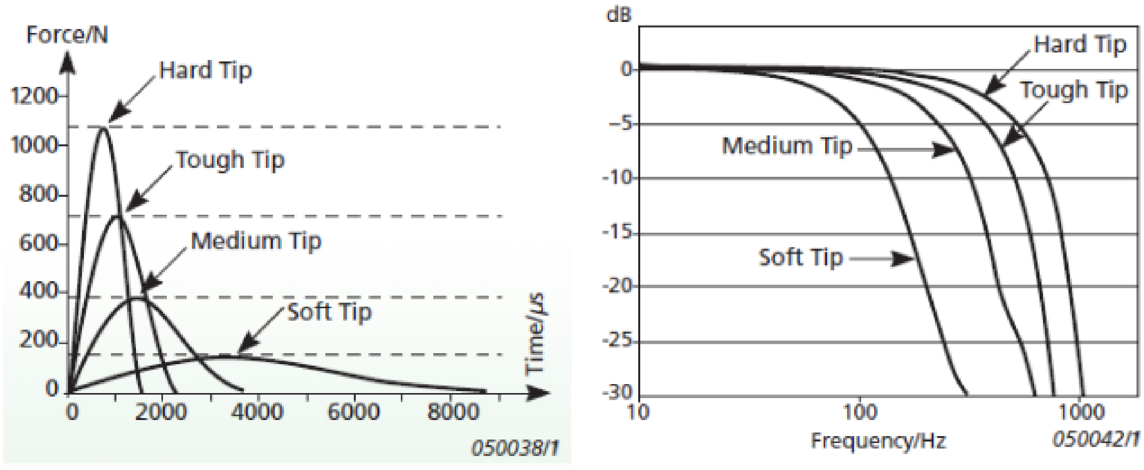

(a)

(b)

Figure 2.5: (a) Impulse shapes of the hammers showing the shape as a function of the used impact tip. (b) Force spectra of the hammers showing the frequency response as a function of used impact tip [90].

Single input multiple output (SIMO) protocol was employed in order to optimize the data consistency. In this case, several accelerometers were attached to the predefined positions, and the impacted hammer roved around the tested element to obtain the dynamic response of the structure.

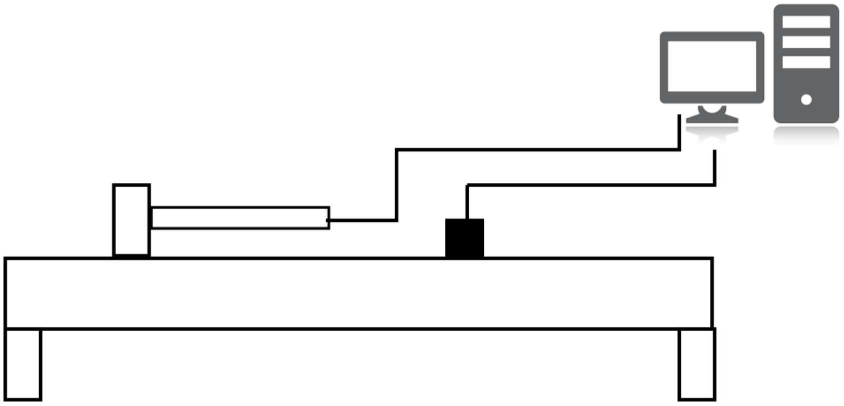

Figure 2.6: Illustration of the EMA set-up.

2.3.3. Force Generated by ISO Tapping Machine

There are several standardized excitation sources, such as ISO tapping machine, Japanese ball, rubber tire. The Japanese ball is a hollow heavy-soft spherical impact source defined in the Japanese standards [91]. This source is 2.55 kg weight and 183 mm in diameter. The impact force of the rubber ball has properties close to the impact of human [34]. Another source described in [92] is a 3 kg rubber tire which is dropped from 300 to 900 mm height. The peak of force can be 1250 to 2400 N. This source is employed to mimic the children jumping [93]. The ISO tapping machine may not be the best choice to investigate the low-frequency noise. In this work, the ISO tapping machine is employed as the impact source. But before the ISO standards abandon this source to evaluate the impact noise down to 50 Hz, it is necessary to investigate its dynamic behavior.

The current standards [12, 13, 94] employ a five-hammer tapping machine as an excitation source, shown in Figure 2.7.

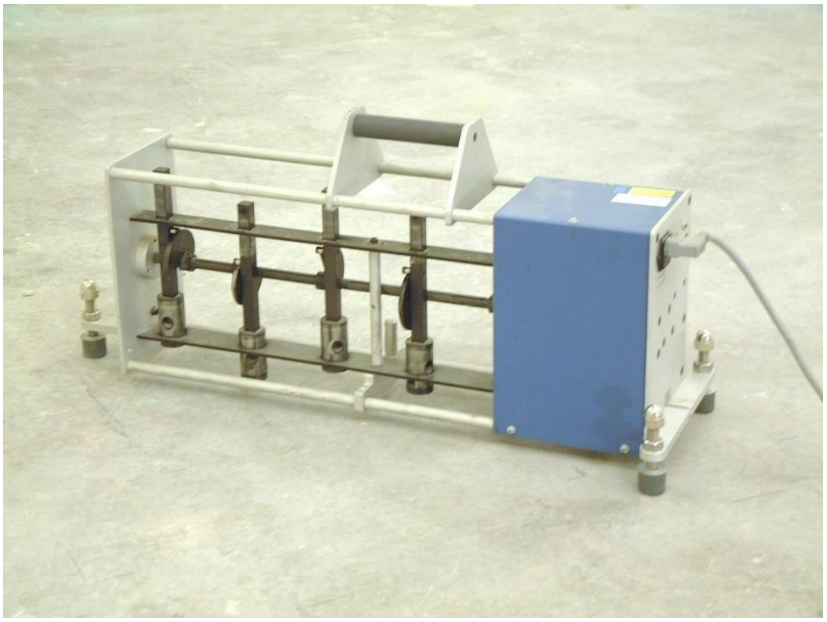

Figure 2.7: ISO standardized tapping machine [14].

The hammers are distributed along a line, the distance between two hammers being 40 cm. Each hammer measures 0.5 kg, freely falling from 4 cm height. The hammers strike the floor 10 times/s [95]. This source can be described by the Fourier series [40]:

$$F(t) = F_0 + 2\sum_{n=1}^{\infty} F_n\, cos(\omega_n t), \tag{2-4}$$

where $\omega_n = n2\pi f_s$ and F_n are the Fourier coefficients which can be obtained by:

$$F_n = \frac{2}{T}\int_0^T F(t)\cos(\omega_n t)\, dt = \frac{2}{T} I = 2mv_0 f_s, \tag{2-5}$$

where I represents the momentum that results from the impact hammer mass m striking the floor surface in question with velocity v_0. This result holds strictly for the ideal impact, meaning that the hammer and surface of the floor are hard enough that each impact force can be considered as an ideal Dirac Delta function, illustrated in Figure 2.8.

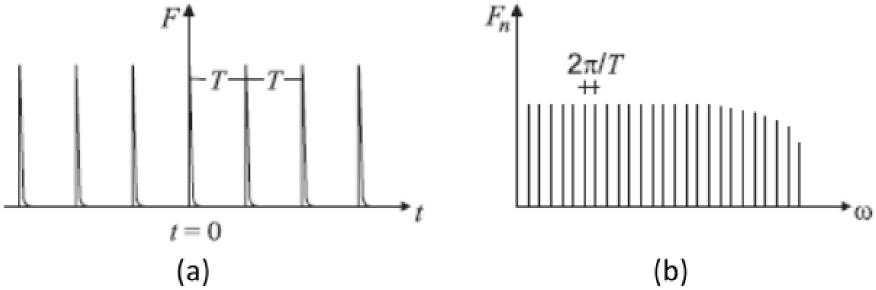

Figure 2.8: (a) Time dependence of force produced by the mechanical hammer system (b) Spectrum of force [96].

Vér [97] improved this model by adding an elastic layer on the top of the concrete base floor. But same as Cremer’s model, the practical application of this model is only suitable for low admittance floor. In another work [98], the excitation stiffness was taken into account in the analytical model for the wooden structure. But the model just considered the whole mass of the floor, whereas the participation of the floor mass varies depending on the different eigen-modes. Moreover, the energy dissipation of the floor was ignored in this model. Another improvement of the model was made by taking into consideration the local and global impedance in the model [99]. Nonetheless, the discrepancies in the simulations and the measurements induced by the relative velocity between the bounced hammer and the vibrating floor were observed when comparing the analytical results and the experimental data. This problem was addressed in [100]. However, just a slight improvement was achieved when mimicking measurement results, even though the relative velocity between the hammer and the vibrating floor was introduced in the model. Until here, each improvement increased the complexity of the analytical model, whereas no satisfying force prediction results were achieved.

2.3.4. Stochastic Approach

It is well known that the variety of the wood species, the variation in a nominally identical wooden structure, as well as the lack of material properties database, make the reliable material properties of wood difficult to obtain. Consequently, the calibration of a model is always tedious and time-consuming. Moreover, even with the calibrated model to predict the theoretical identical wooden structure, the prediction results may be different from the realistic case due to the uncertainties induced by wood material properties, workmanship, and geometrical details in structures. As a result, the deterministic model may not be representative enough in a realistic situation. Therefore, it is a necessary step to quantify the variations in the model’s outputs in order to establish an accurate prediction tool ultimately. To achieve that, uncertainties of the wood material properties can be addressed in a model by introducing probabilistic parameters [36]. In Reference [57], a generalized probabilistic model was constructed to take into account the statistical fluctuation associated with the elastic properties in the model. The uncertainties of the mechanical constants of a wooden structure were also investigated in Reference [101]. A small database of Young’s modulus in the longitudinal direction was established by means of vibration measurements. Then, by sampling Young’s modulus distribution established by the obtained database, Monte Carlo simulations were performed in the FE model development to quantify the uncertainties induced by the elastic constants in modelling the vibro-acoustic behavior of wooden buildings in a low-frequency range. However, not only does Young’s modulus in the longitudinal direction have a great impact on the dynamic response of a wooden structure, but Young’s moduli in the other two directions, as well as the shear moduli, play an important role in its vibroacoustic performance. Regarding the uncertainties in structural dynamics, Shannon's maximum entropy principle [102] is an optimal choice to model the random data and the uncertainties [103]. In Reference [104, 105], a probabilistic model was proposed to construct the probability distribution in high-dimension of a vector-valued random variable using the maximum entropy principle. This proposed probabilistic model was then extended to a tensor-valued coefficient (stiffness tensor) with different symmetric levels [103, 106, 107].

2.3.5. Floating Floor Modeling

The reaction of the floating floor can be classified into "locally reacting" or "resonantly reacting". The "locally reacting" floor is often calculated by supposing the floor to be infinitely large and highly damped so that there is no reflecting wave in the slab. The force injected onto the upper slab is only transmitted to the lower structural floor in the vicinity of the excitation position. The impact sound improvement of the "locally reacting" floating floor is described by Cremer [40] as:

$$\Delta L = 40 \log\left(\frac{f}{f_0}\right), \tag{2-6}$$

where f_0 is the resonance frequency of the floor, $f_0 = \frac{1}{2\pi}\sqrt{\frac{s}{\rho_1} + \frac{s}{\rho_2}}$, with s being the dynamic stiffness per unit area of the resilient layer and $\rho_1$and ρ_2 being respectively the mass per unit area of the upper and structural slabs. However, this simplification of the slab being infinite is unrealistic. When the floor is of finite size and lightly damped, the floor is resonantly reacting, meaning that the force injected on the upper slab can excite a homogenous bending wave field on the floor. The impact sound improvement model was improved by Vér [97] as:

$$\Delta L = 30 \log\left(\frac{f}{f_0}\right), \tag{2-7}$$

Equation (2-7) gives a 9 dB/Oct impact sound improvement instead of 12 dB/Oct in Equation (2-6) when we double the frequency. But it is worth noting that the “locally reacting” model (Cremer’s model) and the “resonantly reacting” model (Vér’s model) are only validated for the frequency range higher than the resonance frequency of the floor. These two models are improved by taking into account the prediction at the resonance frequency [108], but the behavior of the floating floor at low frequencies is still ambiguous. It is found that the dynamic stiffness of the resilient layer involved in the floor composition has a very important influence on the impact sound insulation improvement even for every low-frequency range [109]. The influence of more different factors, such as the floating plate dimensions, the elastic properties of the floating plate and the impact position, on the impact sound transmission in the low-frequency range, were further investigated by Cho [110]. Park et al. [49] stated that above the resonance frequency of the floating floor, the upper slab and the structural slab independently react to the input force, whereas, below the resonance frequency, the upper and lower slabs are coupled and they react to the input force as one entire panel. The previous research investigated how different factors influence the impact sound insulation improvement of a floating floor, however, they are descriptive research. The quantitative investigation on the effects of the different factors is still unknown. The ambiguity of the effects of the different factors on the low-frequency impact sound insulation improvement can induce difficulties during the floor conception and in the field of application of the floating floor. To sum up, quantifying the impact of different parameters on the dynamic response of floor is an important step towards understanding and controlling the dynamic response of floor, which is one crucial intermediate step to develop an accurate impact sound insulation prediction model.

CHAPTER 3 MODELLING OF THE DYNAMIC BEHAVIOR OF THE ISO TAPPING MACHINE

This chapter is dedicated to the article entitled “*Calibration of the ISO tapping machine for finite-element prediction tool on a wooden-base floor*” published in ***Building Acoustics***.

Résumé

L’un des principaux défis des constructions en bois est d’obtenir une isolation acoustique de haute qualité, notamment en réduisant le bruit d’impact dans les basses fréquences. Afin d'éviter des tests expérimentaux coûteux en phase de conception, des outils de prévision fiables sont nécessaires. La recherche présentée dans ce chapitre est une étude initiale sur la modélisation de la machine à choc normalisée ISO sur un plancher en Cross Laminated Timber en utilisant la méthode des éléments finis. Le plancher a d'abord été calibré en fonction de ses propriétés dynamiques. L'influence des propriétés mécaniques du plancher a été discutée. La force générée par la machine à choc a ensuite été introduite dans le modèle du plancher Cross Laminated Timber établi. Le modèle a finalement été validé en comparant les résultats simulés avec les accélérations mesurées.

Mots clés: bruit d’impact; modélisation; machine à choc.

Abstract

One important challenge of the wooden constructions is to achieve a high quality of acoustic insulation, especially decreasing the impact noise in the low-frequency range. In order to avoid over-designed solutions and expensive experimental tests in the design phase, reliable prediction tools are in great need. The research reported in this chapter is an initial investigation of modeling the ISO standardized tapping machine on a Cross Laminated Timber floor, by using the FE method. The wooden-based floor was first calibrated in terms of its dynamic properties. The influence of the material properties of the Cross Laminated Timber floor was discussed. The force generated by the tapping machine was then introduced in the established Cross Laminated Timber model. The model was finally validated by comparing the simulation results with the measured accelerations.

Keywords: impact sound; finite-element modeling; ISO tapping machine.

3.1. Introduction

During the last decades, the wooden constructions have steadily increased in the market share due to many advantages, such as sustainability, thermal performance, and so on. However, the sound insulation issue is a big challenge for these kinds of constructions. Even when these buildings fulfill the requirements of the ISO sound insulation standards [94, 111] the impact noise, especially at low-frequency range, is often a source of nuisance for the residents in the wooden buildings [32, 35, 50]. One reason is that the evaluation standards were initially designed for the heavy constructions. And without enough knowledge about the wooden constructions, the standards are directly applied to wooden buildings. Moreover, not enough attention is paid to the low-frequency noise in the evaluation standards, as the standardized evaluation frequency range is from 100 to 3150 Hz [13]. The impact sound in wooden building is described as “thumb” or “boom” which means most of the energy in the low-frequency range, even lower than 100 Hz. Compared to the “clarks” coming from the concrete floor, the impact sound of a wooden floor is more like a muffled “thump”. The energy determining the standardized evaluation is lower than 250 Hz. Only reducing the high frequency content but not low-frequency content can not efficiently improve the sound rating [112]. With an adaptation term, the evaluation frequency range could go down to 50 Hz; however, frequencies below that value are believed to have a big influence on how inhabitants perceive the vibroacoustic performance of those buildings. Consequently, objective evaluations do not always correlate with subjective evaluations. Until now, most improvements of the acoustic insulation of wooden constructions are based on the empirical models, engineers’ experience, and experimental tests which are always expensive and time-consuming. To that end, the use of reliable low-frequency range impact sound insulation prediction tools in the design phase would be of great importance in order to decrease the price and time cost of the wooden construction. To establish a numerical prediction model, the first question is how to model the standardized excitation source in the numerical model.

3.1.1. Aims and Outline of the Chapter

The chapter reported here aims at investigating the dynamic behavior of the ISO tapping machine and proposing a force modeling method that can be employed in a larger project in the future. To achieve that, the dynamic properties of a CLT floor base are obtained by means of EMA tests. Next, a FE CLT model is established according to the experimental data. This CLT model is a base model to calculate the accelerations of the floor produced by the ISO tapping machine to validate the force modeling method.

The first section of this chapter dedicates to the measurements carried out on the CLT floor. The EMA tests were performed to obtain the dynamic information of the floor. The accelerations of the floor produced by the standard tapping machine were recorded in order to validate the force modeling method. In the modeling phase, a FE model of the CLT floor was established by fitting the modeling results to the measurement data. The force modeling method and model validation are shown in the following sections. The obtained results are discussed, and conclusions are drawn in the last section.

3.2. Experimental Tests on the CLT Floor

To calibrate the FE model, the dynamic properties (the eigen-frequencies, the mode shapes, the damping ratios) of this floor were obtained from the EMA tests. The accelerations of the panel generated by the ISO tapping machine were recorded to validate the force modeling method.

3.2.1. Specimen Description

The wooden structural element under investigation is a 4 m × 1.5 m CLT panel obtained from Les Chantiers Chibougamau Ltée in Chibougamau, Province of Quebec, Canada. The specimen is made of Canadian black spruce of machine stress rated grade E1 (L 1950Fb et T No. 3/Stud), SPF (spruce-pine-fir) machine stress rated (MSR) parallel layers, and SPF Stud/visual grade No. 3 lumber in transverse layers with a density of 520 kg/m^3. This species accounts for 12% of Canada's total softwood inventory and is desirable for its straight lines, lightweight, fiber density, and dimensional stability.

3.2.2. Measurement Set-up

At the initial stage, the 4 m × 1.5 m CLT panel was assembled with another same dimension CLT panel with the help of a nailed lath. This assembled 4 m × 3 m floor was mounted on a console of a step sound laboratory which has a sound sending upper volume and a sound receiving lower volume, shown in Figure 3.1 (a). However, the dynamic properties of this entire CLT floor were difficult to extract due to the weak connection of the two assembled CLT slabs and intricate boundary condition set-up in the console of the step sound laboratory. As a result, only one half CLT slab was investigated to avoid the uncertainties induced by the connection between the panels. The CLT panel was placed on top of the steel-I beams at the shorter sides of the CLT (cf. Figure 3.1 (b)) with the two longer sides of CLT set free (SFSF boundary conditions).


(a) (b)

Figure 3.1: (a) Two leaves CLT panel connected with a thin lath in the standardized step sound laboratory; (b) Simply supported CLT panel.

3.2.3. Experimental Modal Analysis Test on the CLT Floor

EMA tests were conducted on the CLT panel in order to extract the dynamic properties of the specimen. A predefined mesh grid (cf. Figure 3.2) was drawn on the top of the CLT to determine the positions of the excitation and the accelerometers. The resolution of the mesh grid depends on the frequency range of interest as well as the mode shapes. The mode shapes should be estimated before the tests. The excitation positions should not locate on the nodes of the estimated mode shapes. Otherwise, the information of this mode will be lost in the measurement data. The uni-axial accelerometers (Brüel & Kjær Accelerometer Type 4507 001) were placed on the point 10, 11, 13, 17, and 24 (red dots), and the impact hammer (Brüel & Kjær impact hammer Type 51994) was roved around all the points except the shorter edges where zero displacements were assumed. The accelerometers and the impact hammer were connected to the Brüel & Kjær LAN-XI Type 3050-A-060 6 channels front-end. The acceleration signals and the force signals were collected by the Brüel & Kjær PULSE Labshop. The eigen-frequencies, the mode shapes, and the corresponding damping ratios were obtained with the help of the Brüel & Kjær PULSE Reflex.

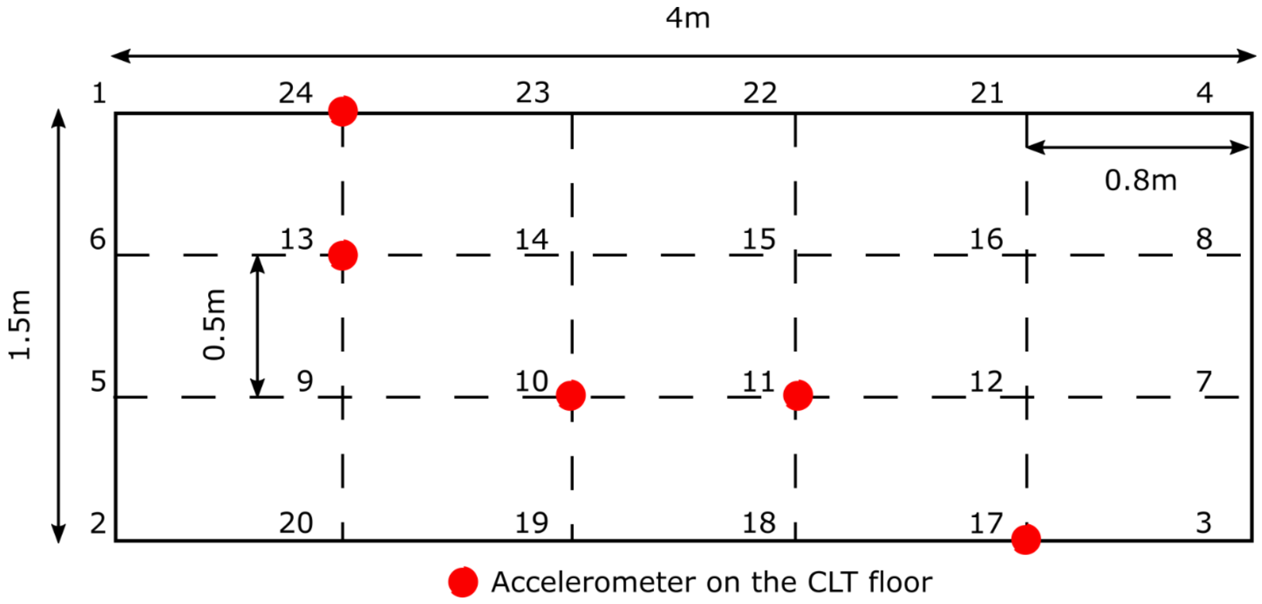

Figure 3.2: Mesh drawn on the surface of the CLT floor.

After the dynamic properties and the dynamic responses of the CLT were extracted, the standardized ISO tapping machine was placed at point 14 on the top of the CLT to investigate the vibration behavior of the CLT plate. The collected information was used to validate the prediction method of the ISO tapping machine. At the initial stage, only one hammer was taken into account. The other four hammers were tapped under the tapping machine during the tests. One accelerometer was placed just near the striking hammer. And another two accelerometers were attached on point 13 and point 14 to record the accelerations of the floor in order to eventually retrieve the force (Figure 3.3).

Figure 3.3: Measurement of the tapping machine on the top of the floor.

3.3. Dynamic Behavior of CLT Floor Modelling

This chapter aims to propose a method to describe the force generated by the ISO tapping machine which could be applied in a larger model afterward. But before developing this method, the dynamic behavior of the CLT floor should be known in the first place, as the ISO tapping machine is put on the top of this floor whose dynamic response can affect the force modeling results. So, the objective of this section is to establish a CLT floor model to provide the relative accurate frequency response function (FRF) simulations in order to validate the force modeling later.

3.3.1. Error Metrics

3.3.1.1. Normalized Relative Frequency Difference

The normalized relative frequency difference (NRFD) is defined as:

$$NRFD = \frac{|f_{sim} - f_{mes}|}{f_{mes}} \times 100\%, \tag{3-1}$$

where f_{sim} is the simulated eigen-frequency and f_{mes} is the measured eigen-frequency. This error metric evaluates the relative difference of the simulated and the measured eigen-frequencies.

3.3.1.2. Modal Assurance Criterion

The modal assurance criterion (MAC) is written as:

$$MAC = \frac{|(\Phi_i^{sim})^T(\Phi_j^{mes})|^2}{|(\Phi_i^{sim})^T(\Phi_i^{sim})||(\Phi_j^{mes})^T(\Phi_j^{mes})|}, \tag{3-2}$$

where Φ_i^{sim} is the ith simulated eigen-vector and Φ_j^{mes} is the jth measured eigen-vector. When the simulated mode shape is perfectly correlated to the measured one, the MAC equals to 1. While there is no correlation between the simulated and measured mode shapes, the MAC is 0. This error metric characterizes the similarity of the simulated and measured mode shapes. Since when the material properties are changed in the model, the eigen-frequencies and the mode order will be changed at the same time. Sometimes, the calibrated model can provide a high NRFD value but a low MAC number, implying that the simulated mode order is not the same as the measured mode order. So, in the work reported here, both NRFD and MAC should be justified in order to keep the relatively low simulated eigen-frequency shifts, at the same time, to maintain the same simulated mode order as the measured one.

3.3.2. Model Description

The commercial software Abaqus [113] is employed in this thesis to develop different models. The FE CLT model encompasses five parts which represent five plies of the specimen, shown in Figure 3.4. The dimensions of the FE model were set to be 4 m × 1.5 m, the same as the dimension of the floor specimen. The material properties of each layer of CLT were first collected from the literature [58]. And the material property orientation of each layer was 90° rotated with one another to model the cross-laminated layers. All the displacements and the rotations of the shorter edges at the bottom of the CLT model were constrained to mimic the SFSF boundary conditions. The 20-node quadratic brick, reduced integration elements were assigned to the entire model. At initial stage, the coarse meshes were assigned to the model. And then the size of the meshes were decreased until there is no significant change in the simulated eigen-frequencies. Finally, the dimension of the mesh was 0.1 m × 0.1 m to ensure the accuracy of the highest frequency of interest. This dimension of meshes also satisfies with the rule of thumb of 6-8 meshes per wavelength. The CLT was calibrated as the accuracy of the base model influences the accuracy of the method/element introduced later in model.

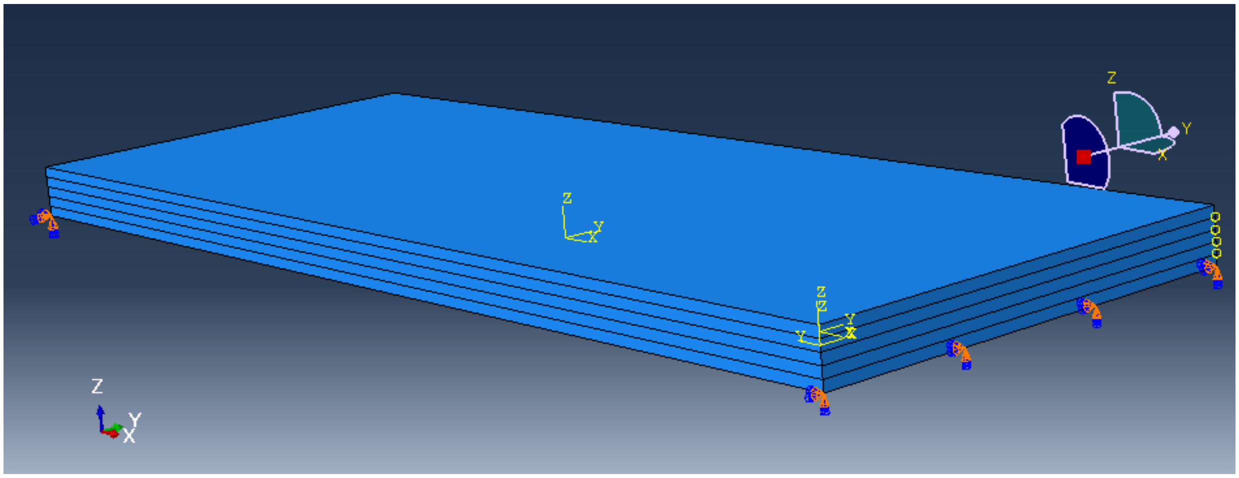

Figure 3.4: FE model of the 5-ply CLT.

3.3.3. Model Calibration

In order to calibrate the CLT model, the elastic material properties were collected from literature and then tweaked until a good match of the simulated eigen-frequencies and the mode shapes was achieved. The CLT model was calibrated in terms of the error metrics introduced in the previous section. The calibrated elastic properties are shown in Table 3.1. The calculated NRFD and MAC values are presented in Figure 3.5 and Figure 3.6.

Table 3.1: Material properties of CLT used in the calibrated FE model.

E_1	E_2	E_3	G_{12}	G_{13}	G_{23}	ν_{12}	ν_{13}	ν_{23}	ρ
8500	3800	3800	800	70	61.8	0.3	0.3	0.44	520

* Stiffness parameters have the unit of MPa, and the density is given in kg/m^3.

Table 3.2: Simulated and measured eigen-frequencies of the bending modes and the corresponding measured damping ratios.

Mode	Simulated eigen-frequency	Measured eigen-frequency	Damping ratio
1	22.2	19.8	4.9
2	33.7	32.2	3.6
3	56.2	56.7	3.2
4	72.9	73.8	3.2
5	105.0	91.0	3.3
6	118.7	125.5	2.8

7	146.8	139.8	1.7
8	170.8	170.4	1.2

* The simulated and measured eigen-frequencies are in Hz and the damping ratios are shown in percentage (%).

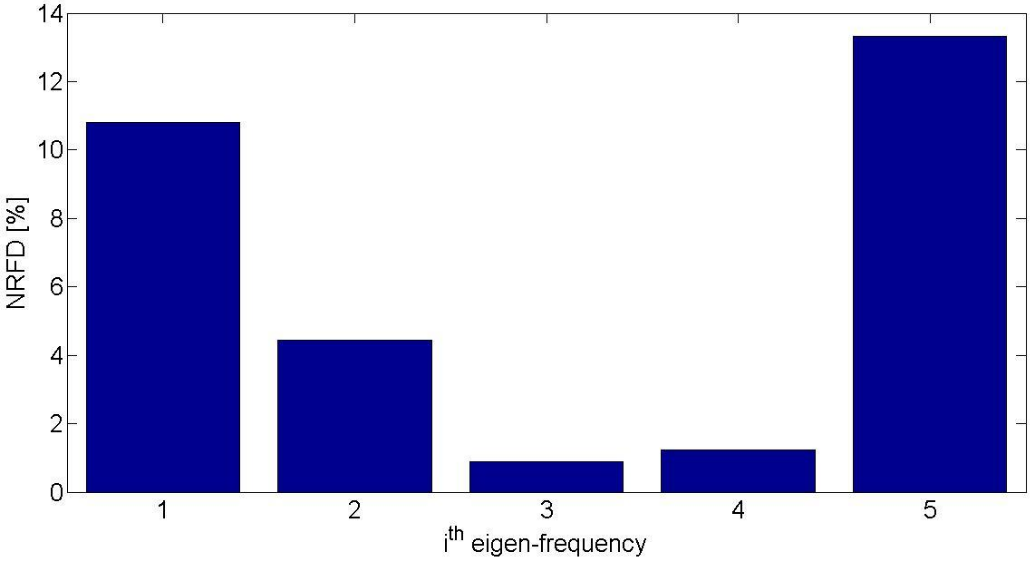

Figure 3.5: NRFDs of the simulated and measured eigen-frequencies.

From the NRFD and the MAC, it can be observed that lower than 100 Hz, all the eigen-frequencies are well captured by the model. The NRFD stays in a relatively low range. And MAC values are in a high range from the 1^{st} to the 4^{th} mode. The simulated FRFs were also compared with the measured FRFs in order to increase the stability and the reliability of the model. A steady-state analysis was performed in Abaqus to obtain the FRFs of the CLT model at points 11, 13, 17, and 24, cf. Figure 3.2. The damping ratios extracted from the experimental tests (shown in Table 3.2) were introduced in the model by means of the direct modal damping.

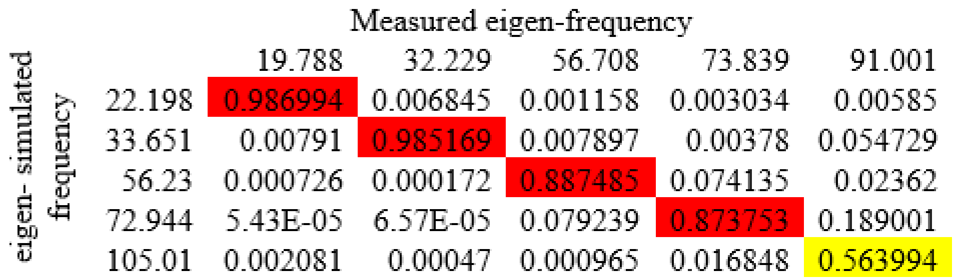

eigen- simulated frequency	Measured eigen-frequency 19.788	32.229	56.708	73.839	91.001
22.198	0.986994	0.006845	0.001158	0.003034	0.00585
33.651	0.00791	0.985169	0.007897	0.00378	0.054729
56.23	0.000726	0.000172	0.887485	0.074135	0.02362
72.944	5.43E-05	6.57E-05	0.079239	0.873753	0.189001
105.01	0.002081	0.00047	0.000965	0.016848	0.563994

Figure 3.6: MAC of the simulated and measured mode shapes of the CLT floor.

3.3.4. Results and Discussions

The simulated and measured FRFs of the specimen at different positions are shown in Figure 3.7.

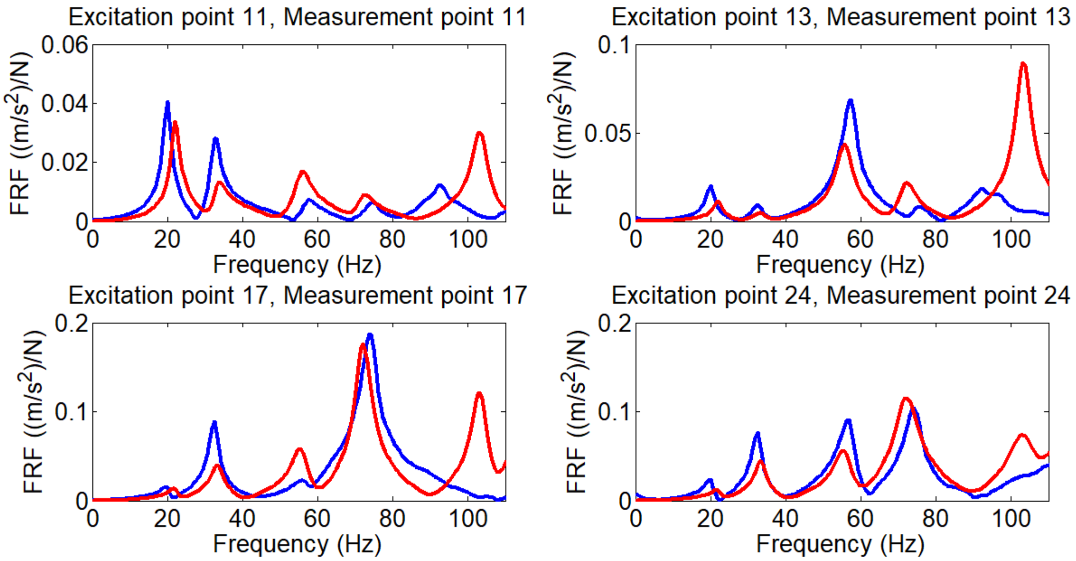

Figure 3.7: FRFs of points 11, 13, 17 and 24. The measurement results are shown in blue and the simulation results in red.

From Figure 3.7, it can be seen that even though there are some eigen-frequency shifts and some discrepancies of simulated amplitudes in the simulations, the first 4 simulated resonances (red curves) at different points are close to the measured ones (blue curves). But when frequency range comes to higher than 80 Hz, an extra resonance appears in the simulations. The simulated eigen-frequency shifts and the extra resonance may result from the inaccurate material properties employed in the model. Since wood is a natural material, it's material properties can have a significant variation and the nominally identical wooden elements can have different dynamic behavior. So, further investigation of the material properties should be carried out to obtain more accurate FRFs. Another source of error could be the ill-conditioned boundary condition of the CLT model when mimicking the real boundary condition. After all, the perfect simply supported boundary condition is very difficult to achieve in the laboratory. The support is always elastic so that the displacement on the boundary is not strictly 0. Constraining all the displacements and the rotations on the boundary lines of the CLT model can be too strong boundary conditions for this real case.

3.4. Dynamic Behavior of the ISO Tapping Machine Modelling

Once the CLT is calibrated in terms of the eigen-frequencies, the eigen-modes, as well as the FRFs, the force generated by the ISO tapping machine, can be introduced in the model. In another work [114], it was proven that in the steady-state regime, the accelerations of a floor calculated in the time domain is equivalent to the ones calculated in the frequency domain. Moreover, the frequency domain calculation is more effective and less time-consuming. Following that conclusion, the frequency domain method was performed to calibrate the model.

3.4.1. Force Determination

In order to avoid the complicated mathematical calculation to describe the force generated by the tapping machine, another modal method [115] is employed here aiming at characterizing the force in question. It is known that the accelerations of the CLT floor at point 10 and point 13 could be written as:

$$A_{10} = FRF_{10\_14} \times F_{14}, \tag{3-3}$$

$$A_{13} = FRF_{13\_14} \times F_{14}, \tag{3-4}$$

where A_{10} and A_{13} are the accelerations at point 10 and point 13, FRF_{10_14} is the FRF linked to points 10 and 14, FRF_{13_14} is the FRF linked to points 13 and 14, and F_{14} is the force generated by one hammer of the ISO tapping machine at point 14. Therefore, the input force generated by the tapping machine could be written as:

$$F_{14} = \frac{A_{13}}{FRF_{13\_14}}, \tag{3-5}$$

where FRF_{13_14} could be obtained from the previous model of the CLT.

After the force is determined from Equation (3-5), the acceleration at point 10 can be deduced by the FRF_{10_14} given by the CLT model and the input force at point 14. It should be noticed that since the calculation of the FRF of the CLT is restricted up to 100 Hz, the measured acceleration should be filtered up to 100 Hz to keep the same frequency content as the input FRF when deriving the input force according to Equation (3-5).

3.4.2. Results and Discussions

The simulated and measured accelerations at point 10 by employing the method introduced in the previous section are shown in Figure 3.8.

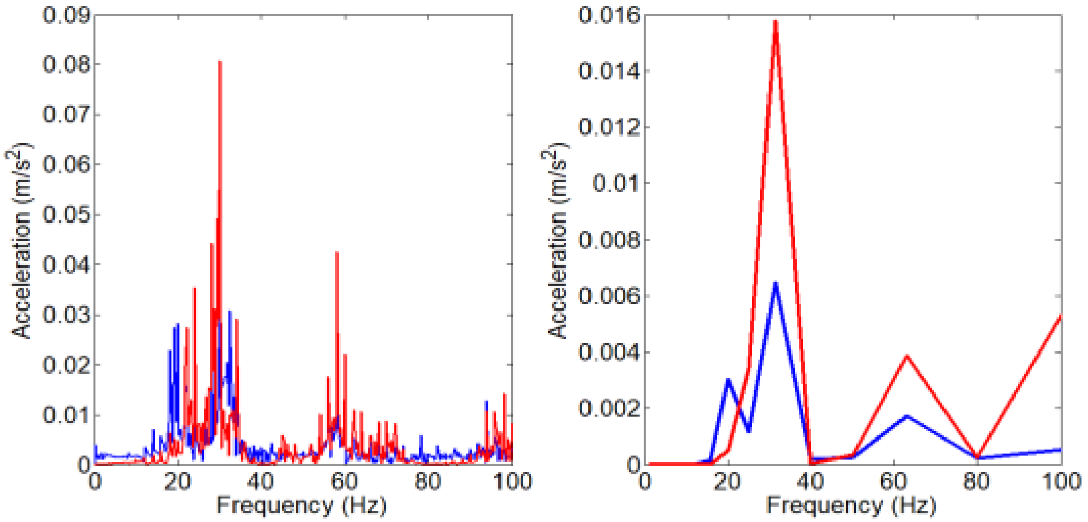

(a) (b)

Figure 3.8: (a) Acceleration of CLT at point 10 in narrowband; (b) Acceleration of CLT at point 10 in 1/3 octave band. Measured acceleration in blue and simulated acceleration in red.

It can be observed in Figure 3.8 that two main resonances are caught by the simulations. The simulated accelerations of the CLT floor correlate better with the measure accelerations around 60 Hz. One of the possible reasons is that the simulated FRFs of the CLT fit better with the measured ones from 30 to 70 Hz. The frequency shifts around 30 Hz may be caused by the frequency shifts of the simulated FRFs lower than 30 Hz in Figure 3.7. Furthermore, it is found that the discrepancies between the simulated accelerations and the measured accelerations become larger compared with the discrepancies in mimicking the measured eigen-frequencies and FRFs in the previous section. It may be due to the uncertainties of the previous simulation from the previous step of simulations. After all, the simulated FRFs are not perfectly correlated with the measured ones. Another source of error could also be an indirect way to estimate the input force. But directly measuring the force will change the contact surface between the hammer and floor surface and subsequently change the force injected into the system. So, this indirect method will still be used in the following model development.

3.5. Conclusions

An indirect force modeling method is developed in this chapter. To achieve that, a base model, the CLT model, was established in order to provide the dynamic system to further calculate the accelerations to validate the force modeling method. This dynamic system, the CLT floor was calibrated by means of the eigen-frequencies, eigen-modes, and FRFs. A quite good agreement is achieved in terms of the FRFs of the CLT at different excitation positions in the low-frequency range, up to 100 Hz, even though there are still some frequency shifts in the simulation results. Then, the force generated by the ISO standardized impact tapping machine was introduced in the previously established CLT model. The simulated accelerations show a good correlation at certain frequencies. But there were still some unignorable discrepancies between the simulations and measurements, which may be due to the frequency shifts in the FRFs modeling propagating and accumulating in the following acceleration simulation step.

So, the simulated FRFs should be further improved to increase the accuracy of the model. The material properties can have a significant impact on the accuracy of simulated eigen-frequencies and the mode order. The material properties of entire CLT panel can be obtained from EMA test [10]. But in this chapter, each layer of the CLT model is modeled as an orthotropic material. In this case, there are nine variables (three Young’s moduli, three shear moduli, and three Poisson’s ratios) to calibrate. During the material properties’ calibration procedure, it is found that when one variable is increased, the effect can be compensated by decreasing another variable. As a consequence, the best combination of material properties can not be easily determined. Furthermore, the calibration procedure is repetitive and tedious. So, more concerns should be paid to material properties’ calibration. Another important factor is the boundary condition. The floor is simply supported on the top of two steel beams. However, it is very difficult to ensure the displacements at these two simply supported edges are 0 when the floor is excited. So, constraining all the displacements and rotations along the simply supported edges are too strong restrictions for modeling the real boundary condition. So, the boundary condition in the model should be further refined to improve the accuracy of the results.

CHAPTER 4 STOCHASTIC CALIBRATION PROCEDURE

This chapter is dedicated to the article entitled “*Development of a Vibroacoustic Stochastic Finite Element Prediction Tool for a CLT Floor*” published in ***Applied Sciences***.

Résumé

L'isolation acoustique en basse fréquence est une tâche ardue à réaliser. Les prédictions en basse fréquence sont nécessaires pour accéder au comportement dynamique d'un plancher en bois lors de la phase de conception initiale afin de réduire le bruit d'impact en basse fréquence. Cependant, en raison de la complexité du matériau du bois et de divers détails structuraux, il est difficile d'obtenir des prédictions de vibrations précises des structures en bois. En même temps, un modèle déterministe ne peut pas représenter correctement le cas réel en raison des incertitudes liées aux propriétés des matériaux et aux changements géométriques. L'approche stochastique introduite dans ce chapitre vise à quantifier les incertitudes induites par les propriétés des matériaux et à proposer une méthode d'étalonnage alternative pour obtenir un résultat relativement précis à la place de l'étalonnage manuel conventionnel. De plus, 100 simulations ont été calculées dans différentes positions d'excitation afin d'évaluer les incertitudes induites par les propriétés mécaniques du matériau du bois lamellé-croisé. Une comparaison entre les résultats simulés et mesurés a été réalisée pour extraire la meilleure combinaison de module de Young et de module de cisaillement dans différentes directions du Cross Laminated Timber.

Mots clés: constructions en bois; bruit en basse fréquence; modélisation; processus stochastique

Abstract

Low-frequency impact sound insulation is a challenging task in wooden buildings. Low-frequency prediction tools are needed to access the dynamic behavior of a wooden floor in an early design phase to ultimately reduce the low-frequency impact noise. However, due to the complexity of wood and different structural details, accurate vibration predictions of wooden structures are difficult to attain. Meanwhile, a deterministic model cannot properly represent the real case due to the uncertainties coming from the material properties and geometrical changes. The stochastic approach introduced in this chapter aims at quantifying the uncertainties induced by material properties and proposing an alternative calibration method to obtain a relatively accurate result instead of the conventional manual calibration. In addition, one hundred simulations were calculated in different excitation positions to assess the uncertainties induced by the material properties of Cross Laminated Timber. A comparison between the simulated and measured results was made in order to extract the best combination of Young's moduli and shear moduli in different directions of the Cross Laminated Timber panel.

Keywords: wooden constructions; low-frequency noise; modeling; stochastic process

4.1. Introduction

The FE method is a widely employed approach to develop numerical prediction models in the wood industry. By performing numerical simulations, experimental acoustical tests can be reduced, and parametric studies can also be carried out to investigate the influence of specific geometrical changes in construction as well as the influence of the variations/uncertainties in material properties, which always have a markable influence on the results. In recent research [116], experimental tests were conducted on a full-scale CLT floor. The material properties of the CLT were collected from the literature and then put into the established FE model to compare the simulation results with the measured ones. A better correlation between the testing results and the modeling results was attained after tuning the collected material properties of CLT. The latter points out the importance of knowing the material properties if a proper calculation of dynamic properties needs to be achieved. A similar conclusion was drawn in References [117-119]. From the previous chapter, it was concluded that the inaccuracy of the base model can be accumulated in the following calculations. So, it is necessary to increase the accuracy of the model to ensure the accuracy of the following calculations. Among the many different parameters (the boundary conditions, the material properties, the model fineness, etc.) which can have influences on the simulation results, the material properties can have a profound effect on the dynamic behavior of the simulated structure. All the evidence from the literature and the previous research indicates that more attention should be paid to the material properties to obtain a better simulation result.

However, wood being a natural material, it can have a big variance in its material properties and thereby two nominally identical wooden structures possessing the same essence can have different dynamic responses to the external excitation. From the perspective of model calibration, the lack of a large database makes calibrations lack sufficient reliable resources. Besides, wood being an orthotropic material, there are nine elastic constants to be determined/calibrated. When one parameter is changed, the effect of changing this parameter can be compensated by modifying the other one. A big variance of material properties of wood, the lack of database and the orthotropic intrinsic property of wood, so it is intricate to determine which combination of these nine elastic constants is the most representative for the material. To that end, this chapter discusses the method to automize the calibration procedure and to quantify the uncertainties induced by the material properties of the CLT floor.

4.1.1. Aims and Outline of the Chapter

This chapter aims at proposing a method to quantify the uncertainties induced by the material properties, and subsequently giving an estimation of the dynamic response of one sort of floor, instead of only one element. With the developed method, the calibration of material properties can be automated, and the more appropriate material properties can be retrieved from the different simulations to increase the accuracy of the model which can be applied in a larger model afterward.

To achieve that, the Monte Carlo simulation was performed on one variable of the material properties of the CLT floor. Then the method was improved by increasing the number of variables. Joint distributions of different mechanical constants without available material property databases were constructed by means of the maximum entropy principle. The random elastic constants generated following the established distributions were considered as the inputs for the FE model to calibrate CLT in a low-frequency range by comparing the simulated results with its dynamic responses obtained from the EMA method (the measurement results from the 3rd chapter). The best combination of the material properties of the CLT panel is selected by minimizing different error metrics.

4.2. Preliminary Sensitivity Analysis

Wood as a kind of orthotropic material has nine different variables (three Young's moduli, three shear moduli, and three Poisson's ratios) to be calibrated. In order to decrease the complexity of calibration, a sensitivity analysis should be performed to investigate the effect of different elastic constants on simulated eigen-frequencies before the stochastic process is introduced to the FE model. The material properties of the CLT panel collected from literature [86] are reported in Table 4.1. In this section, Young's moduli in different directions are increased or decreased by 25% when compared to Young's moduli given by Table 4.1. Shear moduli in different directions were increased or decreased by 15% when compared to the shear moduli given in Table 4.1. The Poisson ratios, ν_{12}, ν_{13}, ν_{23} were set to be 0.25, 0.25, and 0.35, whereas the initial values were 0.3, 0.3, and 0.4. The reference eigen-frequencies employed in NRFDs were calculated according to the elastic constants in Table 4.1. The measured eigen-frequencies were not selected as a reference since the objective of this sensitivity analysis aims to investigate how different elastic constants affect the eigen-frequencies of an FE model through justifying the NRFDs.

Table 4.1: Material properties of CLT collected from the literature.

E_1	E_2	E_3	G_{12}	G_{13}	G_{23}	ν_{12}	ν_{13}	ν_{23}	ρ
9200	4000	4000	900	90	63	0.3	0.3	0.4	520

* Stiffness parameters have the unit of MPa, and the density is given in kg/m^3.

From the NRFDs shown in Figure 4.1 and Figure 4.2, it can be seen that the influence of Young's moduli and shear moduli on eigen-frequencies cannot be ignored. Among all the elastic constants, Young's modulus in the longitudinal direction has the most important influence on eigen-frequency changes. However, Young's modulus in a vertical direction barely changes the eigen-frequencies. Therefore, the variation of Young's modulus in the vertical direction is not reported in Figure 4.1. When looking at Figure 4.3, we could find that all the NRFDs are lower than 0.5%, which indicates that the influences of Poisson's ratios on eigen-frequencies are negligible. From this sensitivity analysis, it can be concluded that Young's moduli and shear moduli have a more significant influence on eigen-frequency calculations than Poisson's ratios. So, the calibration of material properties can be reduced to six variables.

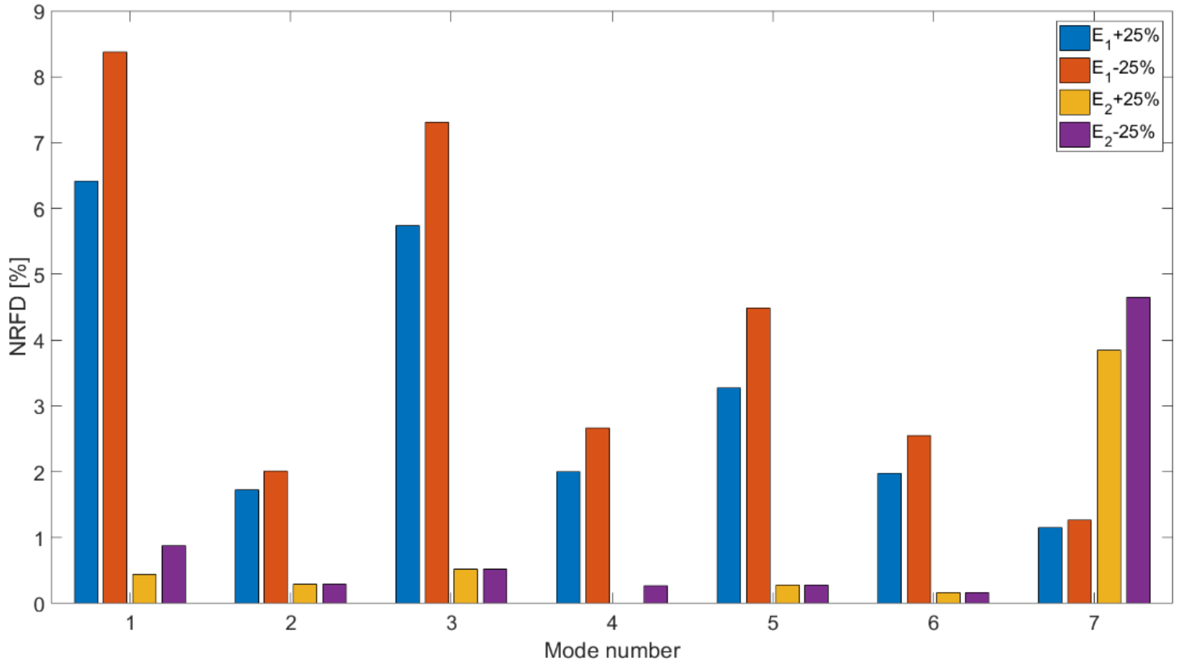

Figure 4.1: NRFDs of Young’s moduli.

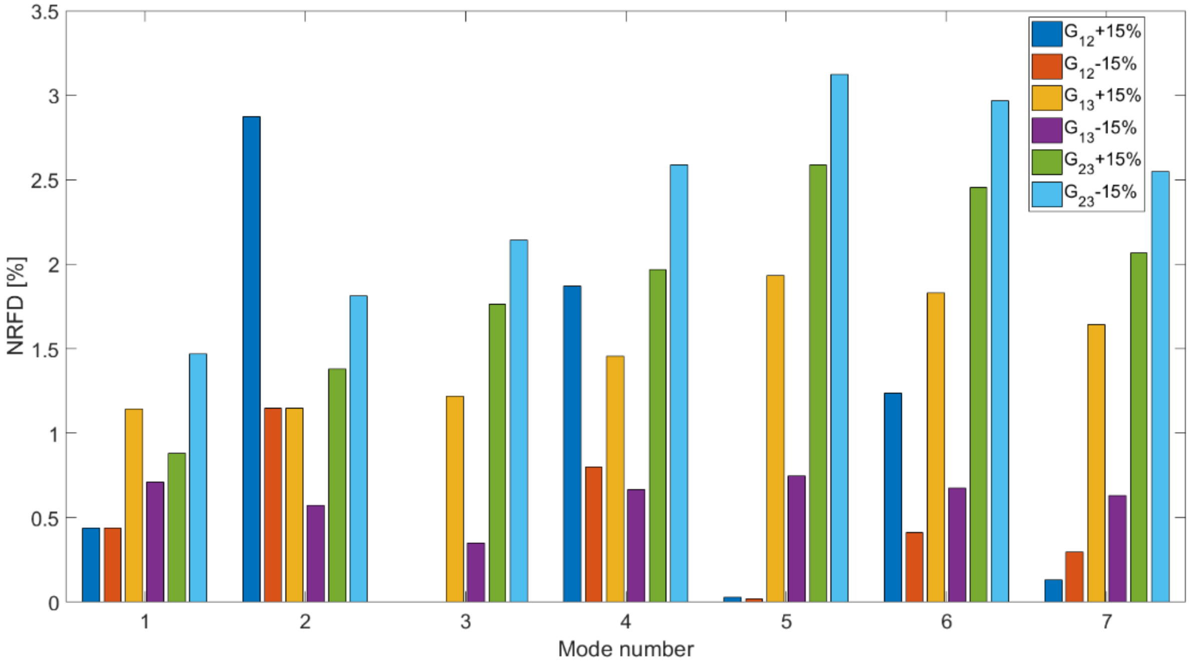

Figure 4.2: NRFDs of shear moduli.

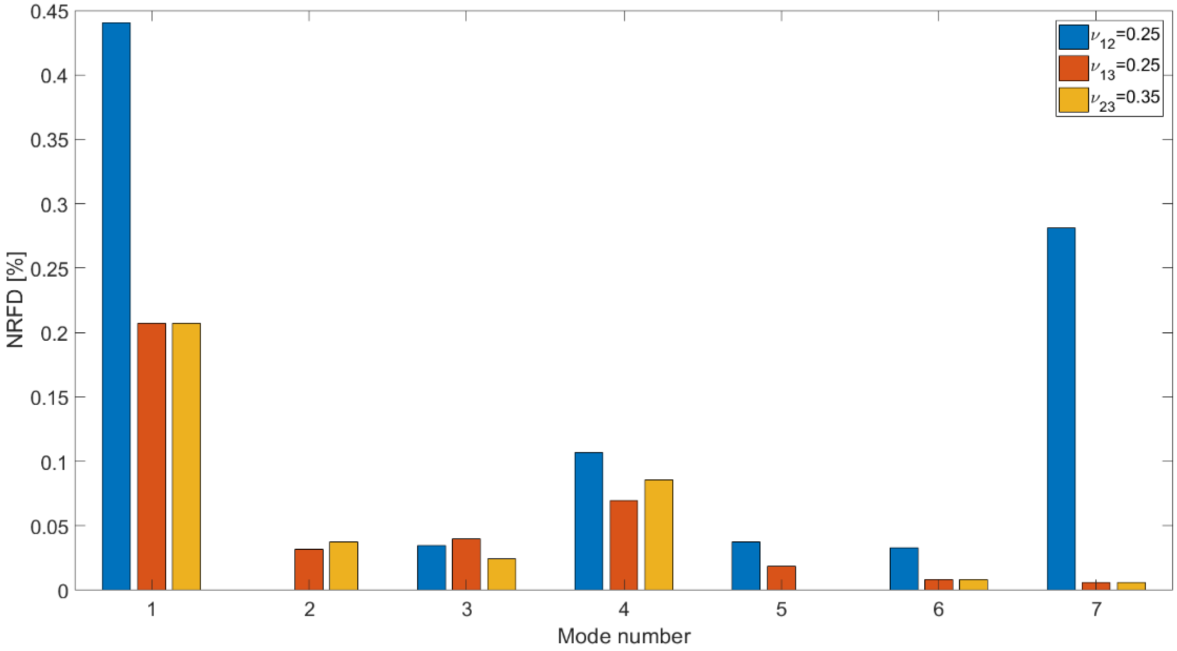

Figure 4.3: NRFDs of Poisson's ratios.

However, from this sensitivity analysis, it can also be noticed that the first four simulated eigen-frequencies are always higher than the first four measured eigen-frequencies even decreasing different elastic constants. This may be caused by the over-stiffened boundary condition. Since the tested CLT was only placed on the top two steel I beams. It is difficult to have a perfect simply supported boundary conditions in reality. Therefore, restricting all the displacements at the boundaries of the FE model can create over stiffened boundary conditions, which results in over-estimated eigen-frequencies. Consequently, the displacement in a vertical direction at one boundary of the FE model is released to try to mimic the real boundary conditions.

4.3. Preliminary Single Variable Investigation

It is known that the dynamic behavior of a system highly depends on the combining effect of different material properties. When one parameter is increased, the effect of this increasing parameter can be compensated by decreasing the other one. Besides, the resulting effect, the change of the eigen-frequencies, can not be characterized by a mathematical function of different material properties. As a consequence, the material properties are difficult to be justified. In this section, in order to ultimately find the most appropriate material properties, the Monte Carlo simulation was performed on one single variable. Next, the stochastic process is extended to six variables to quantify the uncertainties coming from the material properties. After that, the most appropriate material properties can be chosen from the simulations.

The sensitivity analysis of the material properties of CLT indicates that Young's modulus in the longitudinal direction of each wooden layer of the CLT model has the largest influence on the output results. Therefore, only the influences of Young's modulus in the longitudinal direction and the shear moduli are investigated in this work. The Monte Carlo simulation is performed to evaluate the influence of Young's modulus in the longitudinal direction E_1 and shear modulus G_{12} on the dynamic response of the CLT model.

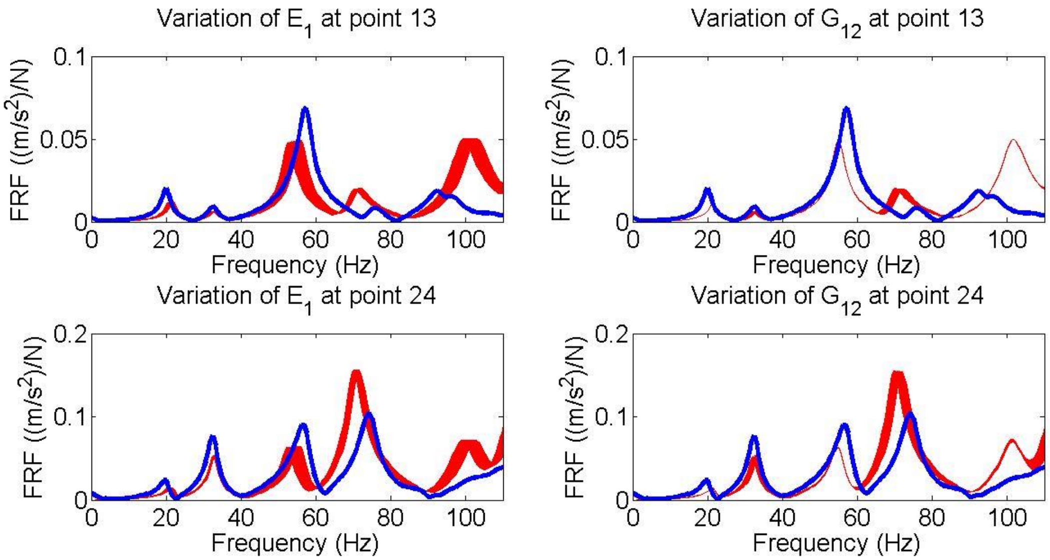

Figure 4.4: FRFs of the point 13 and 24. The blue curves are the measurement results, and the red curves (40 realizations) are the simulation results with different material properties.

The variation of Young's modulus in the longitudinal direction E_1 of each layer is supposed to obey the uniform distribution ranging from 7000 to 9000 MPa and shear modulus G_{12} obeys the uniform distribution ranging from 700 to 900 MPa. Young's modulus and shear modulus generated by Matlab [120] were then exported in Abaqus. The calculations at different points are realized by Abaqus with help of Python script. The results are represented in Figure 4.4. It could be observed from Figure 4.4 that the envelopes of the variations of Young's modulus are larger than that of the variations of shear modulus, due to the fact that Young's modulus has a more significant impact on the dynamic behavior of the CLT than the shear modulus. Consequently, a slight change of Young's modulus can induce a more important change in the dynamic response of the CLT. It should be mentioned that all the probability distribution functions are assumed to follow a uniform distribution which may not be the reality. Thus, a more suitable material property description would help to improve the results. Furthermore, only one elastic constant was changed each time so that it is difficult to have a global evaluation of how the different mechanical constants in different directions influence the FRFs or the vibration behavior of the floor. Therefore, it would be more reasonable to change the different material constants at one time in order to evaluate how the different material properties affect the behavior of the slab. To that end, the stochastic process of multi-variables is introduced.

4.4. Stochastic Process

Even though most material property distributions are non-Gaussian in nature [121, 122], uncertainties of material properties are always assumed to follow the Gaussian distribution for the sake of simplicity and due to the lack of relevant experimental data. The theory introduced in this chapter is about the probabilistic modelling of a random elasticity tensor in an orthotropic symmetric level within the framework of the maximum entropy principle under the constraint of the available information [106, 107, 123]. The established random elasticity tensor is considered as the inputs in the FE model to quantify the uncertainties induced by the CLT material properties and to seek the best combination of CLT material properties to calibrate the CLT model.

In this section, the elastic tensor is firstly decomposed in terms of random coefficients and tensor basis so that the fluctuation of different elastic constants can be characterized by the probability distribution functions (PDF). Next, the method of constructing the PDFs of different elastic constants in high-dimension [104] is shortly introduced. Lagrange multipliers associated with the explicit PDFs of random variables in high dimensions is estimated with the help of the Itô differential equation. The established PDFs are sampled by the Metropolis-Hastings algorithm to obtain the random data to construct a random elasticity matrix [106, 107] in order to derive the corresponding random combinations of elasticity constants to quantify the uncertainties of material properties and to calibrate the CLT model. A flow chart of the application of the stochastic procedure is shown in Figure 4.5.

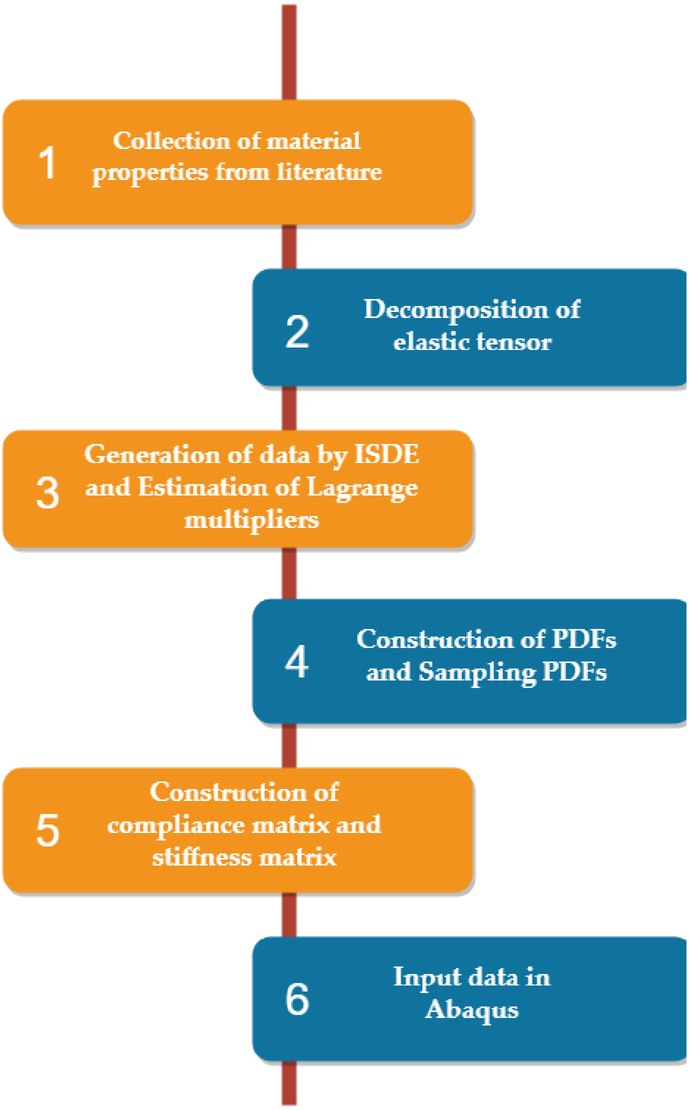

Figure 4.5: Flow chart of the application of the stochastic process.

4.4.1. Decomposition of the Random Elastic Tensor

The approach of construction of a PDF with a multi-variables can be applied to any arbitrary material symmetry class [103, 106, 107], such as isotropic symmetry, cubic symmetry, and transversely isotropic symmetry. In this work, this stochastic approach aims to seek a reasonable probability distribution of the random elastic tensor of the target material (CLT).

Therefore, only the orthotropic symmetry case is considered in this case. The dimension of the random variable $\boldsymbol{N}$ is limited to 9.

Let $\boldsymbol{C}$ be a fourth-order random elastic tensor, which could be decomposed by using the equation below:

$$\boldsymbol{C} = \sum_{i=1}^{N} c_i \boldsymbol{E_i}, \tag{4-1}$$

where c_i is a set of random coefficients that can be described by its PDFs and $\boldsymbol{E_i}$ is the tensor basis of the random elastic tensor $\boldsymbol{C}$, based on Walpole's derivation [124]. The CLT slab is modeled as orthotropic material in Abaqus so that the tensor basis $\boldsymbol{E_i}$ of the orthotropic symmetric elastic tensor are defined in the following form [106]:

$$\begin{cases} \boldsymbol{E^{11}} = \boldsymbol{a} \otimes \boldsymbol{a} \otimes \boldsymbol{a} \otimes \boldsymbol{a}, \boldsymbol{E^{12}} = \boldsymbol{a} \otimes \boldsymbol{a} \otimes \boldsymbol{b} \otimes \boldsymbol{b}, \boldsymbol{E^{13}} = \boldsymbol{a} \otimes \boldsymbol{a} \otimes \boldsymbol{c} \otimes \boldsymbol{c}, \\ \boldsymbol{E^{21}} = \boldsymbol{b} \otimes \boldsymbol{b} \otimes \boldsymbol{a} \otimes \boldsymbol{a}, \boldsymbol{E^{22}} = \boldsymbol{b} \otimes \boldsymbol{b} \otimes \boldsymbol{b} \otimes \boldsymbol{b}, \boldsymbol{E^{23}} = \boldsymbol{b} \otimes \boldsymbol{b} \otimes \boldsymbol{c} \otimes \boldsymbol{c}, \\ \boldsymbol{E^{31}} = \boldsymbol{c} \otimes \boldsymbol{c} \otimes \boldsymbol{a} \otimes \boldsymbol{a}, \boldsymbol{E^{32}} = \boldsymbol{c} \otimes \boldsymbol{c} \otimes \boldsymbol{b} \otimes \boldsymbol{b}, \boldsymbol{E^{33}} = \boldsymbol{c} \otimes \boldsymbol{c} \otimes \boldsymbol{c} \otimes \boldsymbol{c}, \\ E^{4}_{ijkl} = \left(a_i b_j + b_i a_j\right)(a_k b_l + b_k a_l)/2, \\ E^{5}_{ijkl} = \left(b_i c_j + c_i b_j\right)(b_k c_l + c_k b_l)/2, \\ E^{6}_{ijkl} = \left(c_i a_j + a_i c_j\right)(c_k a_l + a_k c_l)/2, \end{cases} \tag{4-2}$$

where $\boldsymbol{a}$, $\boldsymbol{b}$, and $\boldsymbol{c}$ are the unit orthogonal vectors, $\otimes$ is the Kronecker product.

The fourth-order elastic tensor $\boldsymbol{C}$ is decomposed as:

$$\begin{gathered} \boldsymbol{C} = c_1 \boldsymbol{E^{11}} + c_2 \boldsymbol{E^{22}} + c_3 \boldsymbol{E^{33}} + c_4 (\boldsymbol{E^{12}} + \boldsymbol{E^{21}}) + c_5 (\boldsymbol{E^{23}} + \boldsymbol{E^{32}}) + c_6 (\boldsymbol{E^{31}} + \boldsymbol{E^{13}}) \\ + c_7 \boldsymbol{E^{4}} + c_8 \boldsymbol{E^{5}} + c_9 \boldsymbol{E^{6}}. \end{gathered} \tag{4-3}$$

4.4.2. Construction of Probability Distribution Function in High-Dimension Using the Maximum Entropy Principle

The objective of this section is to establish the PDFs of the random coefficients c_i, which control the statistical fluctuation of the fourth-order random elastic tensor. Let $\boldsymbol{c} = (c_1, \dots, c_N)$ be a vector in $\mathbb{R}^N$-valued second-order random variable, which obeys certain unknown probability distribution $P_{\boldsymbol{c}}(d\boldsymbol{c})$ with the Lebesgue measure $d\boldsymbol{c} = dc_1 \dots dc_N$. The element in vector $\boldsymbol{c} = (c_1, \dots, c_N)$ represent the random coefficient of the random elasticity matrix in the previous section (Equation (4-3)). The unknown probability distribution $P_{\boldsymbol{c}}(d\boldsymbol{c})$ of the vector, $\boldsymbol{c}$ can be presented by a probability density function $p_{\boldsymbol{c}}(\boldsymbol{c})$, which satisfies the following normalization condition:

$$\int p_{\boldsymbol{c}}(\boldsymbol{c}) d\boldsymbol{c} = 1. \tag{4-4}$$

The Maximum Entropy Principle applied here aims to construct the unknown probability distribution $P_{\boldsymbol{c}}(d\boldsymbol{c})$ with the help of the available information. The PDF $p_{\boldsymbol{c}}$ could be written using the equation below:

$$p_{\boldsymbol{c}} = arg\ max\, S(p), \tag{4-5}$$

where the entropy $S(p)$ is defined by the equation below:

$$S(p) = -\int p(\boldsymbol{c})\, log\big(p(\boldsymbol{c})\big)\, d\boldsymbol{c}. \tag{4-6}$$

In order to find an explicit probability density function $p_{\boldsymbol{c}}(\boldsymbol{c})$, several constraints should be set as available information: (1) the mean values of the variables, (2) the log condition, and (3) the normalization condition.

$$E\{\boldsymbol{C}\} = \bar{\boldsymbol{c}}, \text{with } \bar{\boldsymbol{c}} = (\bar{c}_1, \dots, \bar{c}_9), \tag{4-7}$$

$$E\left\{log\left(det\left(\sum_{i=1}^{N} c_i \boldsymbol{E}\right)\right)\right\} = \nu_C, \text{with } |\nu_C| < +\infty \tag{4-8}$$

and

$$\int p_c(\boldsymbol{c}) d\boldsymbol{c} = 1. \tag{4-9}$$

Equation (4-7) indicates that the mean values of variables are supposed to be known and Equation (4-8) ensures that both the $\boldsymbol{C}$ and $\boldsymbol{C}^{-1}$ are second-order random variables. This equation also creates the statistical dependence between the different random variables.

To optimize the problem defined by Equation (4-5), Lagrange multipliers associated with Equations (4-7) to (4-9) are introduced. Let $\lambda^0 \in \mathbb{R}^+$, $\boldsymbol{\lambda^1} \in \mathrm{A}_{\lambda_1}$, and $\lambda^2 \in \mathrm{A}_{\lambda_2}$ be Lagrange multipliers associated with the constraints defined by Equations (4-7) to (4-9). It could be proven that the optimized Equation (4-5) could be written as [123]:

$$p_{\boldsymbol{C}}(\boldsymbol{c}) = k_0\, exp\{- < \boldsymbol{\lambda}_{sol}, \boldsymbol{g}(\boldsymbol{c}) >_{R^{N+1}}\}, \forall \mathbf{c} \in \mathbb{R}^N, \tag{4-10}$$

where $k_0 = \exp(-\lambda^0)$ is the normalizing constant, the operator $<,>$ is the Euclidean inner product, the $\boldsymbol{c} \rightarrow \boldsymbol{g}(\boldsymbol{c})$ is the mapping defined on $S \times \mathbb{R}$, with the values in $\mathbb{R}^{N+1}$. $g(\boldsymbol{c})$ is defined by Equation (4-11) below:

$$g(\boldsymbol{c}) = \left(\boldsymbol{c}, \varphi(\boldsymbol{c})\right), \text{with } \varphi(\boldsymbol{c}) = log\left(det\left(\sum_{i=1}^{N} c_i \boldsymbol{E}\right)\right), \tag{4-11}$$

where $det(\sum_{i=1}^{N} c_i \boldsymbol{E}) > 0$ is the support of Equation (4-11).

An $\mathbb{R}^N$-valued random variable B_λ parameterized by $\boldsymbol{\lambda}$ should be introduced to identify the Lagrange multipliers. Supposing the probability density function $\boldsymbol{b} \rightarrow p_{B_\lambda}(\boldsymbol{b}, \boldsymbol{\lambda})$ of the random variable B_λ is written as:

$$p_{B_\lambda}(\boldsymbol{b}, \boldsymbol{\lambda}) = k_\lambda \, exp\{-< \boldsymbol{\lambda}, \boldsymbol{g}(\boldsymbol{b}) >_{R^{N+1}}\}, \forall \boldsymbol{b} \in \mathbb{R}^N, \tag{4-12}$$

where k_λ is the normalization constant parameterized by λ. Taking $k_0 = k_\lambda$, from Equations (4-10) and (4-12), it can be deduced that:

$$p_{\boldsymbol{C}}(\boldsymbol{c}) = p_{B_\lambda}(\boldsymbol{b}, \boldsymbol{\lambda}). \tag{4-13}$$

According to Equations (4-7), (4-8), (4-11), and (4-13), the calculation of Lagrange multipliers can be derived by evaluating the expectation of $g(\boldsymbol{b}_\lambda)$:

$$E\{\boldsymbol{g}(\boldsymbol{b}_\lambda)\} = (\overline{\boldsymbol{c}}, \nu_c). \tag{4-14}$$

As a result, the problem of the calculation of the Lagrange multipliers converts into generating the independent realizations of the random variable $\boldsymbol{B}_\lambda$ defined over $\mathbb{R}^N$ and then evaluating the left-hand side of Equation (4-14).

4.4.2.1. *Calculation of Lagrange Multipliers*

To derive Lagrange multipliers introduced in the previous section, there are several different methods to generate the independent random variable $\boldsymbol{B}_{\lambda}$ with respect to the corresponding probability density function (Equation (4-13)), such as the Metropolis-Hastings method [125, 126], Gibbs method [127]. However, it should be noticed that the Metropolis-Hastings method demands an appropriate proposal distribution, which is sometimes difficult to choose, and the Gibbs method requires us to know the conditional distributions. As a consequence, it could be intricate to give a robust calculation without an adequate initial guess, especially for a high-dimension case. Therefore, another alternative algorithm is introduced in Reference [104] to generate the independent random variable $\boldsymbol{B}_{\lambda}$.

Random Number Generator

Let $\boldsymbol{u} \rightarrow \Phi(\boldsymbol{u}, \boldsymbol{\lambda})$ be the potential function defined as:

$$\Phi(\boldsymbol{u}, \boldsymbol{\lambda}) =< \boldsymbol{\lambda}, \boldsymbol{g}(\boldsymbol{u}) >_{R^{N+1}}. \tag{4-15}$$

Let $\{(\boldsymbol{U}(r), \boldsymbol{V}(r))\}, r \in \mathbb{R}^{+}$be the Markov stochastic process defined on the probability space (Θ, T, P) indexed by $\mathbb{R}^{+}$with values in $\mathbb{R}^{+} \times \mathbb{R}^{+}$, for $r > 0$, satisfying the following Itô stochastic differential equation (ISDE):

$$\begin{cases} d\boldsymbol{U}(r) = \boldsymbol{V}(r)dr, \\ d\boldsymbol{V}(r) = -\nabla_{u}\Phi(\boldsymbol{U}(r), \boldsymbol{\lambda})dr - \dfrac{1}{2} f_0 \boldsymbol{V}(r)dr + \sqrt{f_0}\, d\boldsymbol{W}(r), \end{cases} \tag{4-16}$$

where $\boldsymbol{W}(r)$ is the normalized Wiener process defined on (Θ, T, P) indexed by $\mathbb{R}^{+}$ and with values in $\mathbb{R}^{N}$. The probability distribution of the initial condition $\boldsymbol{U}(0)$ and $\boldsymbol{V}(0)$ are supposed to be known. The parameter f_0 is a real positive number, which could dissipate the transition part of the response generated by the initial condition and ensures a reasonable fast convergence of the stationary solution corresponding to the invariant measure.

When r tends to infinity, the solution $\boldsymbol{U}(r)$ of ISDE converges to the probability distribution of the random variable $\boldsymbol{B}_\lambda$.

$$\lim_{r \to \infty} \big(\boldsymbol{U}(r)\big) = \boldsymbol{B}_\lambda. \tag{4-17}$$

n_s independent realization of $\boldsymbol{B}_\lambda$ is denoted as $\boldsymbol{B}_\lambda(\theta_1), \dots, \boldsymbol{B}_\lambda(\theta_{n_s})$. Let r_o be the iteration step that the solution of ISDE converges. When $r_k \geq r_0$, the ISDE could be written as the equation below:

$$\begin{cases} d\boldsymbol{U}(r_k) = \boldsymbol{V}(r_k) dr_k, \\ d\boldsymbol{V}(r_k) = -\nabla_u \Phi(\boldsymbol{U}(r_k), \boldsymbol{\lambda}) dr_k - \dfrac{1}{2} f_0 \boldsymbol{V}(r_k) dr_k + \sqrt{f_0} d\boldsymbol{W}(r_k). \end{cases} \tag{4-18}$$

Therefore, the independent realizations $\boldsymbol{B}_\lambda(\theta_l)$ can be presented by the stationary solution of ISDE:

$$\boldsymbol{B}_\lambda(\theta_l) = \boldsymbol{U}(r_k, \theta_l). \tag{4-19}$$

It is worthwhile to mention that the Itô stochastic differential equation defined by Equation (4-16) can be discretized by the Explicit Euler scheme to obtain an approximate solution:

$$k = 1, \dots, M-1, \begin{cases} \boldsymbol{U}^{k+1} = \boldsymbol{U}^k + \Delta r \boldsymbol{V}^k, \\ \boldsymbol{V}^{k+1} = \left(1 - \dfrac{f_0}{2} \Delta r\right) \boldsymbol{V}^k + \Delta r \boldsymbol{L}^k + \sqrt{f_0} \Delta \boldsymbol{W}^{k+1}, \end{cases} \tag{4-20}$$

with the initial conditions:

$$\boldsymbol{U}^1 = \boldsymbol{u}_0, \boldsymbol{V}^1 = \boldsymbol{v}_0, \tag{4-21}$$

where Δr is the iteration step and $\Delta \boldsymbol{W}^{k+1} = \boldsymbol{W}^{k+1} - \boldsymbol{W}^k$ is a second-order Gaussian centered $\mathbb{R}^N$-valued random variable with a covariance matrix $E\{\Delta \boldsymbol{W}^{k+1} (\Delta \boldsymbol{W}^{k+1})^T\} = \Delta r\{I_N\}$, where $\boldsymbol{W}^1 = 0_N$. In Equation (4-20), $\boldsymbol{L}^k$ is an $\mathbb{R}^N$-valued random variable, which is the partial derivative of $\Phi(\boldsymbol{u}, \boldsymbol{\lambda})$ defined by the equation below:

$$L_j^k \cong -\frac{\Phi\left(\Delta \boldsymbol{U}^{k,j}, \boldsymbol{\lambda}\right) - \Phi(\boldsymbol{U}^k, \boldsymbol{\lambda})}{U_j^{k+1} - U_j^k}, \tag{4-22}$$

with

$$\Delta \boldsymbol{U}^{k,j} = \left(U_1^k, \dots, U_{j-1}^k, U_j^k + \Delta U_j^{k+1}, U_{j+1}^k, \dots, U_N^k\right), \Delta U_j^{k+1} = U_j^{k+1} - U_j^k. \tag{4-23}$$

Mathematical Expectation Estimation

After the random number generator has been established and the ISDE has been discretized to obtain the random numbers, the expectation of these independent random numbers should be calculated to derive Lagrange multipliers. The mathematical expectation of the random variable $\boldsymbol{B}_\lambda$ can be estimated by using the Monte Carlo method. The evaluation of the mathematical expectation of the random variable $\boldsymbol{B}_\lambda$ is given by the equation below:

$$E\{\boldsymbol{g}(\boldsymbol{B}_\lambda)\} \cong \frac{1}{n_s} \sum_{=1}^{n_s} \boldsymbol{g}\left(\boldsymbol{B}_\lambda(\theta_l)\right). \tag{4-24}$$

After Lagrange multipliers are derived by evaluating the mathematical expectation of the random variable $\boldsymbol{B}_\lambda$, the explicit PDFs of different elastic elements in the random elasticity matrix can be established. Depending on Equation (4-10), the PDF of the elastic tensor for the orthotropic symmetric class material could be defined by using the equation below.

$$p_{\boldsymbol{C}}(\boldsymbol{c}) = p_{C_1,\dots,C_6}(c_1, \dots, c_6) p_{C_7}(c_7) p_{C_8}(c_8) p_{C_9}(c_9), \tag{4-25}$$

with

$$p_{C_1,\dots,C_6}(c_1, \dots, c_6) = k \, det\big(Mat(c_1, \dots, c_6)\big) exp\left(-\sum_{i=1}^{6} \lambda_i^{(1)} c_i\right), \tag{4-26}$$

with

$$Mat(c_1, \dots, c_6) = \begin{pmatrix} c_1 & c_4 & c_6 \\ c_4 & c_2 & c_5 \\ c_6 & c_5 & c_3 \end{pmatrix}, \tag{4-27}$$

and

$$p_{C_j}(c_j) = k_j \exp\left(-\lambda_i^{(1)} c_i\right) c_i^{-\lambda^{(2)}}, j = 7,8,9. \tag{4-28}$$

Remarks 1. *The random variables* $(C_1, \dots, C_6)$*,* C_7*,* C_8*, and* C_9 *are mutually independent of each other.* C_7*,* C_8*, and* C_9 *are Gamma-distributed and the* k *and* k_j *are the normalization constants.*

4.4.3. Numerical Application of the Orthotropic Symmetric Material (CLT)

The material properties of CLT gathered from the literature (cf. Table 4.1) are regarded as an initial starting point (mean value) to proceed with the stochastic approach presented in the previous sections.

In Abaqus, the orthotropic materials compliance matrix can be defined by the engineering constants:

$$\begin{Bmatrix}\varepsilon_{11}\\ \varepsilon_{22}\\ \varepsilon_{33}\\ \gamma_{12}\\ \gamma_{13}\\ \gamma_{23}\end{Bmatrix}=\begin{bmatrix}\frac{1}{E_1} & -\frac{\nu_{21}}{E_2} & -\frac{\nu_{31}}{E_3} & 0 & 0 & 0\\ -\frac{\nu_{12}}{E_1} & \frac{1}{E_2} & -\frac{\nu_{32}}{E_3} & 0 & 0 & 0\\ -\frac{\nu_{13}}{E_1} & -\frac{\nu_{23}}{E_2} & \frac{1}{E_3} & 0 & 0 & 0\\ 0 & 0 & 0 & \frac{1}{G_{12}} & 0 & 0\\ 0 & 0 & 0 & 0 & \frac{1}{G_{13}} & 0\\ 0 & 0 & 0 & 0 & 0 & \frac{1}{G_{23}}\end{bmatrix}\begin{Bmatrix}\sigma_{11}\\ \sigma_{22}\\ \sigma_{33}\\ \sigma_{12}\\ \sigma_{13}\\ \sigma_{23}\end{Bmatrix}. \tag{4-29}$$

The compliance matrix of the CLT panel can be derived depending on the elastic constants reported in Table 4.1 and Equation (4-29). The stiffness matrix is the inverse of the compliance matrix.

$$\boldsymbol{C}=\begin{bmatrix}10.58 & 2.3 & 2.3 & 0 & 0 & 0\\ 2.3 & 5.2619 & 2.4028 & 0 & 0 & 0\\ 2.3 & 2.4028 & 5.2619 & 0 & 0 & 0\\ 0 & 0 & 0 & 0.9 & 0 & 0\\ 0 & 0 & 0 & 0 & 0.09 & 0\\ 0 & 0 & 0 & 0 & 0 & 0.063\end{bmatrix}\times 10^9 \tag{4-30}$$

From Equation (4-30) and the corresponding orthotropic symmetric matrix basis (Equation (4-2)), the mean value of c_i defined in Equation (4-3) can be deduced by using the formulas below.

$$(\bar{c}_1, \dots, \bar{c}_9) = (10.58, 5.2619, 5.2619, 2.3, 2.4048, 2.3, 0.9, 0.09, 0.063) \times 10^9. \tag{4-31}$$

Let $f^{target} = (\bar{\boldsymbol{c}}, \nu_{\boldsymbol{C}})$ be the target vector to compute the Lagrange multipliers.

$$f^{target} \\ = (10.58, 5.2619, 5.2619, 2.3, 2.4048, 2.3, 0.9, 0.09, 0.063, 5.3059). \tag{4-32}$$

And let $f^{est}(\boldsymbol{\lambda}) = \left(\bar{\boldsymbol{c}}(\boldsymbol{\lambda}), \nu_{\boldsymbol{C}}(\boldsymbol{\lambda})\right)$ be the estimated vector to compare with the target vector so that the optimal solution of $\boldsymbol{\lambda}$ can be obtained by solving the following optimization function:

$$J(\boldsymbol{\lambda}^{opt}) = argmin\left((1-\alpha)\left(\bar{\boldsymbol{c}} - \bar{\boldsymbol{c}}(\boldsymbol{\lambda})\right)^2 + \alpha\left(\nu_{\boldsymbol{C}} - \nu_{\boldsymbol{C}}(\boldsymbol{\lambda})\right)^2\right), \tag{4-33}$$

where $\alpha \in [0,1]$ is a free parameter. In this scenario, α is set to be 0.5 to give a robust estimation.

Lagrange multipliers associated with $\boldsymbol{\lambda}^{(\mathbf{1})}$ can be further expressed by means of $\lambda^{(2)}$ [103].

$$\begin{cases} \lambda_1^{(1)} = -\lambda^{\mathbf{2}} \dfrac{c_2 c_3 - c_5^2}{\triangle}, \lambda_2^{(1)} = -\lambda^{(2)} \dfrac{c_1 c_3 - c_6^2}{\triangle}, \lambda_3^{(1)} = -\lambda^{(2)} \dfrac{c_1 c_2 - c_4^2}{\triangle}, \\ \lambda_4^{(1)} = -\lambda^{(2)} \dfrac{(c_5 c_6 - c_3 c_4)}{\triangle}, \lambda_5^{(1)} = -\lambda^{(2)} \dfrac{(c_4 c_6 - c_1 c_5)}{\triangle}, \\ \lambda_6^{(1)} = -\lambda^{(2)} \dfrac{(c_4 c_5 - c_2 c_6)}{\triangle}, \\ \lambda_7^{(1)} = -\lambda^{(2)} \dfrac{1}{c_7}, \lambda_8^{(1)} = -\lambda^{(2)} \dfrac{1}{c_8}, \lambda_9^{(1)} = -\lambda^{(2)} \dfrac{1}{c_9}, \end{cases} \tag{4-34}$$

with

$$\triangle = c_1 c_2 c_3 + 2 c_4 c_5 c_6 - c_1 c_5^{\mathbf{2}} - c_2 c_6^{\mathbf{2}} - c_3 c_4^{\mathbf{2}}. \tag{4-35}$$

From the sensitivity analysis, the initial guess of $\lambda^{(2)}$ is set to be −2. The target optimization function (Equation (4-34)) is evaluated by using the interior-point method (fmincon function) in Matlab.

From Figure 4.6, it could be observed that the optimization algorithm converges fast to a small value and the corresponding optimal values of the Lagrange multipliers are found to be:

$$\begin{gathered}\boldsymbol{\lambda}^{(\mathbf{1})} = \\ \begin{pmatrix}0.1263, 0.2904, 0.2905, -0.0758, -0.2324, \\ -0.0758, 12.9089, 18.4413, 1.2909\end{pmatrix}, \\ \lambda^{(\mathbf{2})} = -1.1618.\end{gathered} \tag{4-36}$$

The estimated vector $f^{est}(\boldsymbol{\lambda})$ is evaluated by the Monte Carlo method.

$$\text{conMC}(n_s) = \left| n_s^{-1} \sum_{i=1}^{n_s} \boldsymbol{g}\big(\boldsymbol{C}(\theta_i)\big) \right|. \tag{4-37}$$

Therefore, the estimated vector $f^{est}(\boldsymbol{\lambda})$ yields the following:

$$f^{est} = \begin{pmatrix}10.5882, 5.2677, 5.2675, 2.3035, 2.4121, 2.2860, \\ 0.8997, 0.0904, 0.0636, 5.3088\end{pmatrix}. \tag{4-38}$$

The cost function of the target vector $J(\boldsymbol{\lambda}^{opt})$ is 1.048211×10^{-3}, which implies good agreement of the estimated values with the reference values.

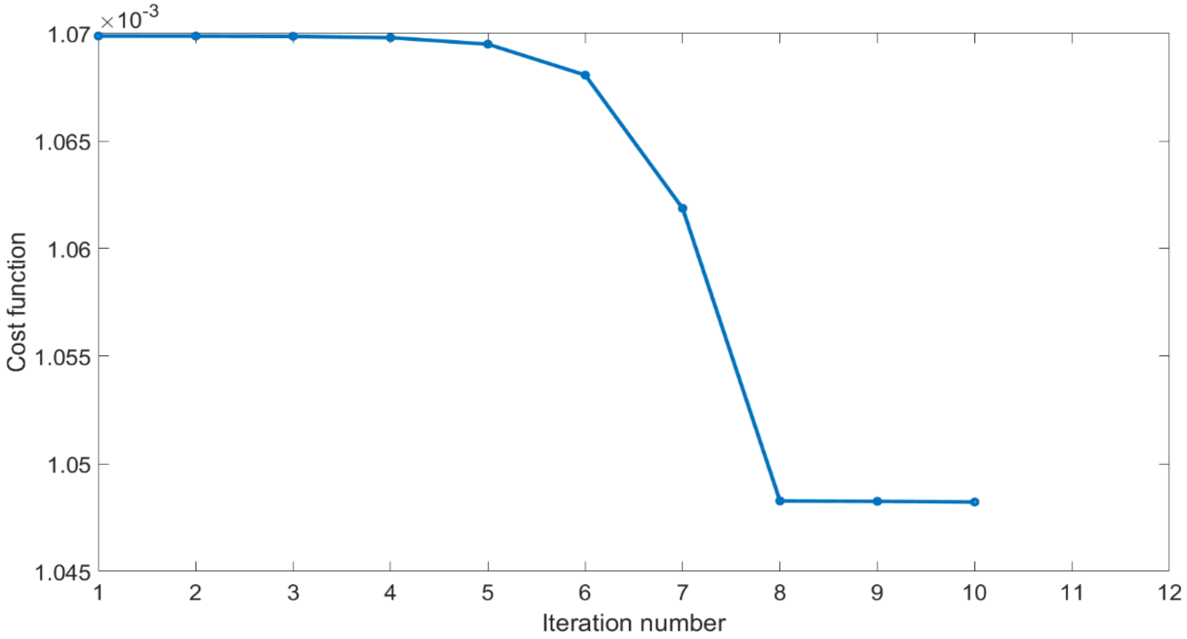

Figure 4.6: Convergence of the optimization algorithm.

4.4.4. Sampling the Defined Probability Distribution Function by Metropolis-Hastings Algorithm

Following the process introduced in the previous section, the PDFs of the random elasticity tensor of the CLT were constructed. The objective of this section is to generate random numbers that obey the defined PDFs. The corresponding random stiffness matrix of CLT can be constructed following the generated data. Subsequently, the compliance matrix of CLT can be derived by transforming the stiffness matrix. The random elastic constants (engineer constants in Abaqus) of CLT can be determined according to Equation (4-29). Lastly, the generated elastic constants should be imported into Abaqus to analyze the dynamic response of the CLT panel. The Markov Chain Monte Carlo method is wildly used to sample the high-dimension PDFs. A specific algorithm, called the Metropolis-Hastings algorithm (MHA), is used in this case to sample the target the function. The proposed distribution is a conventional multi-variate Gaussian distribution. The mathematical support of $p_{C_1,\dots,C_6}(c_1,\dots,c_6)$ is $det(\sum_{i=1}^{N} c_i\boldsymbol{E}) > 0$ and the mathematical support of $p_{C_j}(c_j)$ is $c_j > 0, j = 7,8,9$. When sampling the target function, the generated data should stay in the supports of the sampled function. A total of 50,000 combinations of $(C_1, \dots, C_9)$ are realized by performing the MHA and by obeying the mathematical constraints (supports) of the target functions. The marginal distributions of the different mechanical constants reconstructed by ksdensity function in Matlab are shown in Figure 4.7

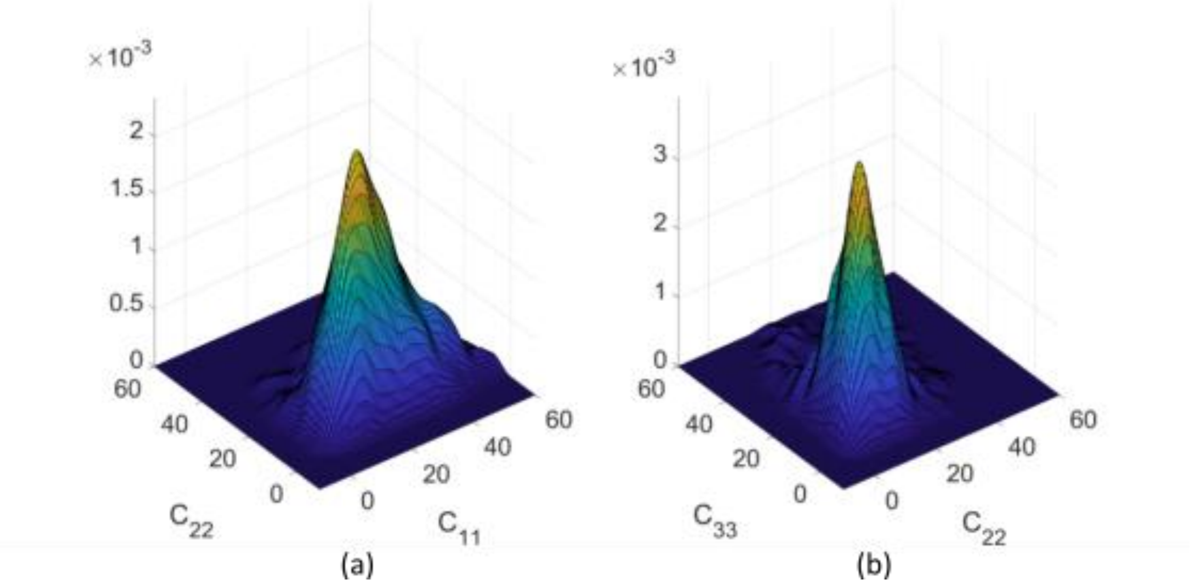

Figure 4.7: (a) Joint probability density function of random variables C_{11} and C_{22}. (b) Joint probability density function of random variables C_{22} and C_{33}.

4.5. Implementation of Stochastic Data in Abaqus

A total of 50,000 generated random numbers $(C_1, \dots, C_9)$ have been generated. The corresponding random stiffness tensor could be determined. The random compliance tensor can also be derived by transforming the random stiffness tensor. Since Poisson's ratios have a very slight influence on the eigen-frequencies and the mode shape order of the CLT numerical model, the variation of the Poisson ratios will not be considered in the FE model. 50,000 generated random elastic constants are only satisfied with the mathematical constraints. The constraints associated with the physical meaning are not considered when generating the random numbers. In order to ensure the data implemented in the FE model has physical meanings, several physical constraints are set:

1) Variation of Young's moduli and shear moduli should be in a reasonable range of wood. The ranges of Young's modulus and the Shear modulus are assumed in $\pm 50\%$ of the respective mean values.

$$E_1 \in [4600MPa, 13800MPa], E_2 \in [2000MPa, 6000MPa], E_3 \in [2000MPa, 6000MPa], \tag{4-39}$$

$$G_{12} \in [450MPa, 1350MPa], G_{13} \in [45MPa, 135MPa], G_{23} \in [45MPa, 135MPa]. \tag{4-40}$$

2) Young's modulus (shear modulus) in a principle direction should be larger than Young's moduli (shear moduli) in the other two directions.

$$E_1 > E_2;\ E_1 > E_3; \tag{4-41}$$

$$G_{12} > G_{13};\ G_{12} > G_{23}. \tag{4-42}$$

3) Young's modulus (Shear modulus) in direction 2 should be larger or equal to Young's modulus (Shear modulus) in direction 3.

$$E_2 \geq E_3;\ G_{13} \geq\ G_{23}. \tag{4-43}$$

Only the generated random elastic constants fulfilled with the above requirements (from Equation (4-39) to Equation (4-43)) could be imported in Abaqus. In the work reported here, due to limited time and limited computer calculation capacity, only 100 different combinations of elastic constants were selected to calibrate the model and to investigate the influence of material properties on the dynamic response of CLT. This large sum of Abaqus input files with different input mechanical constants was realized with the help of Python scripts.

4.6. Results and Discussions

4.6.1. Quantification of Uncertainties

The steady-state simulations with different combinations of material properties were carried out in Abaqus. In Figure 4.8, each subfigure has 100 FRF simulations and the measurement results are shown in blue. Figure 4.8 shows that there is an obvious envelope overlapped around the first four peaks lower than 100 Hz. The larger variation envelope range is caused by a change in five mechanical constants at a time since the effect of five elastic constant changes on the dynamic response of the CLT is greater than the effect of changing only one elastic constant at a time.

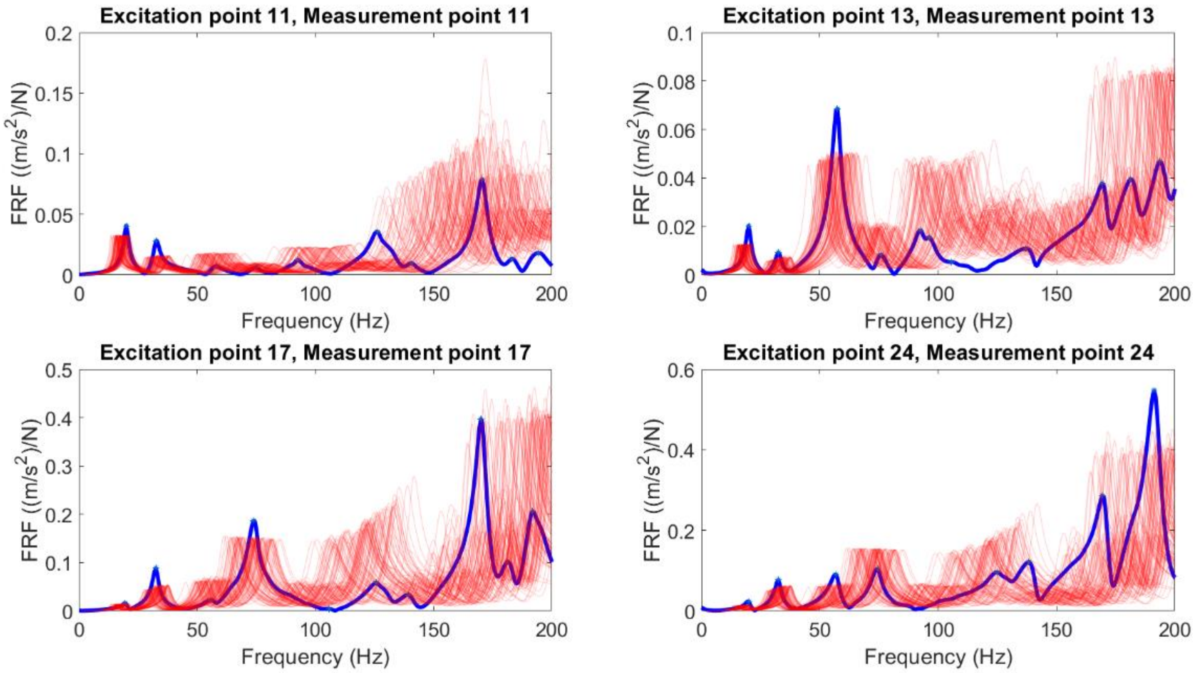

Figure 4.8: Measured (blue) and simulated (red) FRFs at points 11, 13, 17, and 24.

On the contrary to the frequency range lower than 100 Hz, the simulated FRFs begin to scatter above 100 Hz. No clear envelope peaks can be found around the measured resonances higher than 100 Hz. One possible reason for these scattering curves in a relatively higher frequency range is the complexity of the mode shapes. It is known that the lower the eigen-frequency is, the simpler the mode shape is and the longer the wavelength is. Long-wavelength is not sensitive to the small details in the CLT panel, such as the non-uniform air gaps throughout the laminas and the edge bonding (cf. Figure 4.9). It implies that the dynamic behavior of CLT in a low-frequency range can be mimicked by a simplified homogeneous orthotropic laminated FE model. However, when the mode shapes become more complex in a higher frequency range, the wavelength becomes smaller. As a consequence, small details of the CLT panel begin to affect the vibration of the CLT panel. In this case, the homogeneous orthotropic laminated FE model could not properly describe the dynamic response of the CLT panel in the higher frequency range. In order to increase the accuracy of the FE in a high-frequency range, a non-homogeneous laminate layer, such as an account for the irregular air gap in laminas, should be modeled. Nevertheless, it should be aware that the calculation time will become longer when more details are taken into account in the model. The stochastic method needs a large number of calculations to quantify the uncertainties induced by the material properties so that a compromise should be carefully made between the accuracy of the model and the calculation time.

Figure 4.9: (a) Air gaps in the laminate layers of CLT. (b) No edge-bonding of CLT.

4.6.2. Calibration of the CLT Panel

In this section, the best combination of elastic constants of CLT should be identified by selecting the best NRFDs and MACs among 100 simulations. To select the best combination of mechanical constants, the NRFDs of the first four resonances at point 11, point 13, point 17, and point 24 were calculated. The simulations with the smallest NRFDs of the first four resonances at each point were selected from 100 simulations at each point. The NRFDs of the simulated and measured eigen-frequencies at four excitation positions are shown in Figure 4.10. It can be seen from the NRFDs of each excitation position that the NRFDs of the first four resonances are lower than 5%. However, the NRFDs of the 5th and 6th resonances are relatively high when compared to the first four resonances. This result emphasizes that more structural details should be involved in the FE model to calibrate the dynamic behavior of CLT in the frequency range higher than 100 Hz. However, only NRFD values are not enough to justify the best combination of elastic constants. Since the NRFDs can only represent the simulated eigen-frequency shifts when compared with the experimental results, the mode order can be different even with a low NRFD. Therefore, MAC numbers are needed to validate the model by ensuring the modes in the same order with reference even if simulation results provide low NRFDs. The simulated eigen-frequencies and mode shape are reported in and Figure 4.11. The corresponding material properties of CLT are reported in Table 4.2. Figure 4.12 shows that the first six simulated modes are in the same order with the measured ones. However, there exist two extra modes in the simulation results.

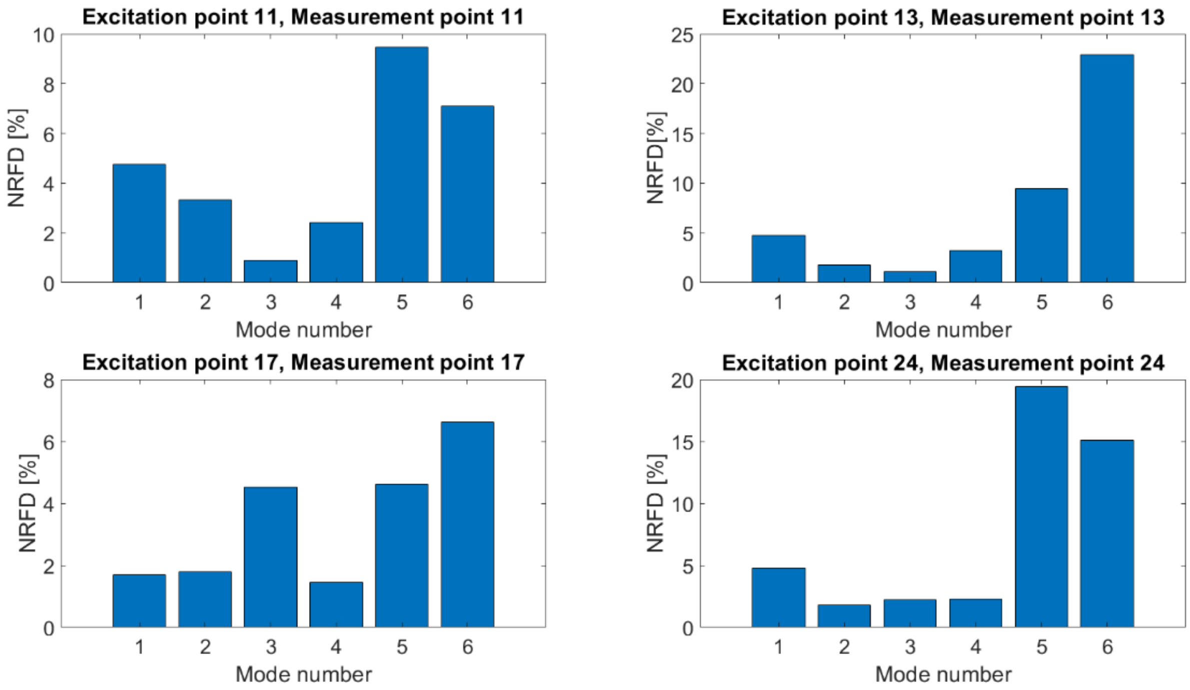

Figure 4.10: NRFDs of the first six resonances at points 11, 13, 17, and 24.

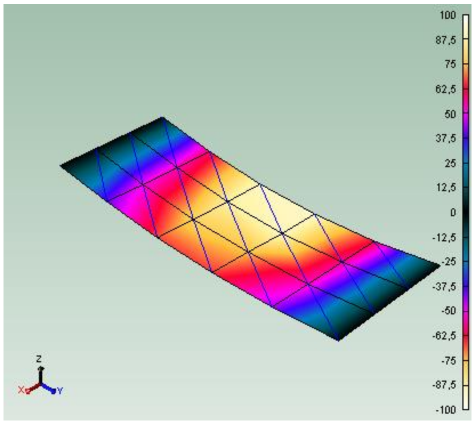

(a1) Measured 1st mode.

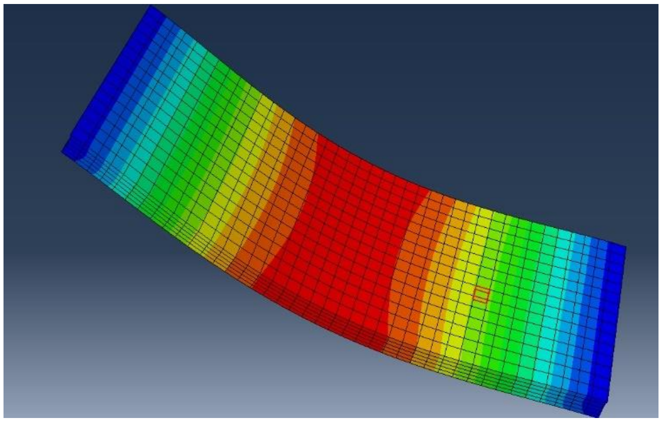

(a2) Simulated 1st mode.

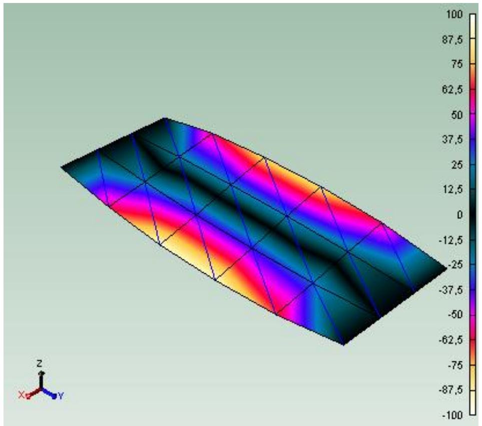

(b1) Measured 2nd mode.

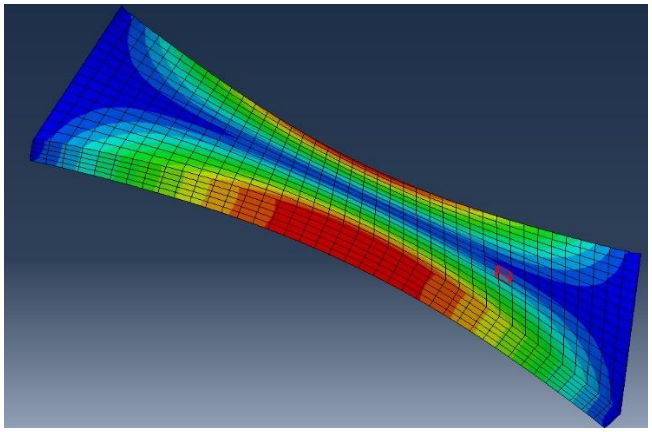

(b2) Simulated 2nd mode.

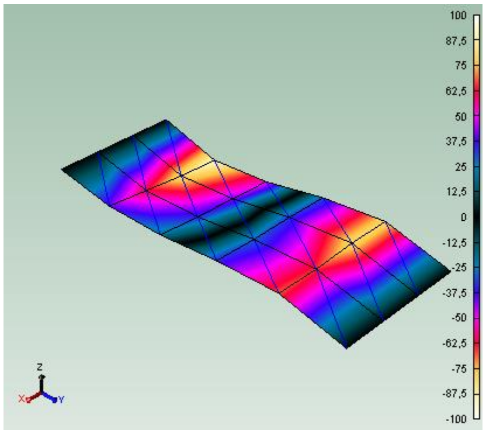

(c1) Measured 3rd mode.

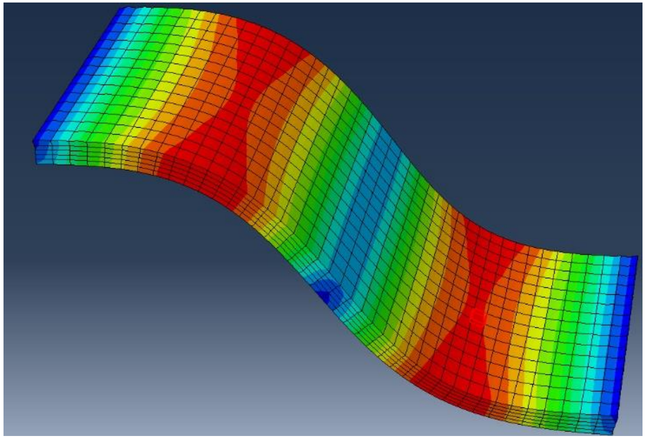

(c2) Simulated 3rd mode.

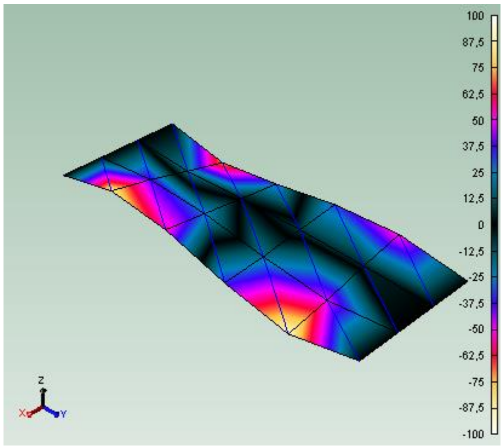

(d1) Measured 4th mode.

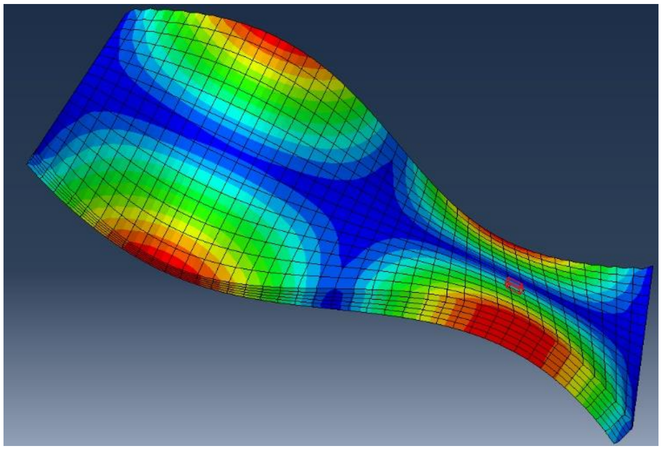

(d2) Simulated 4th mode.

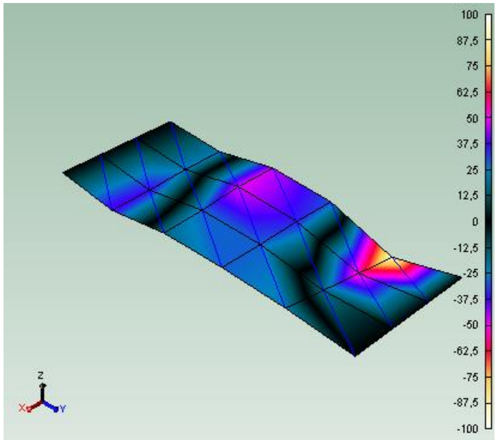

(e1) Measured 5th mode.

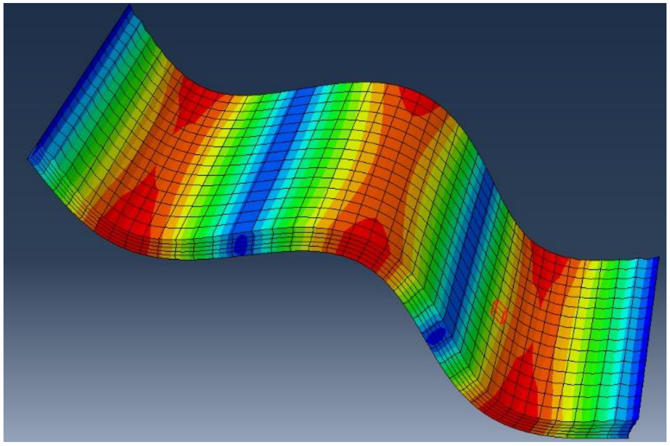

(e2) Simulated 5th mode.

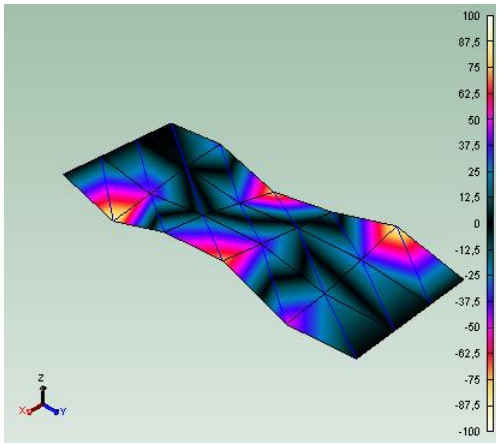

(f1) Measured 6th mode.

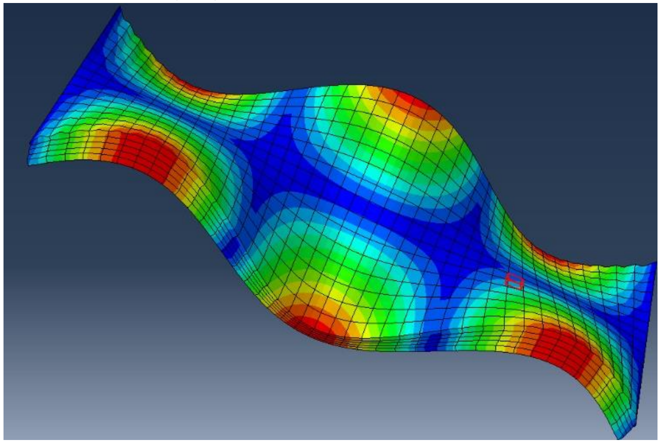

(f2) Simulated 6th mode.

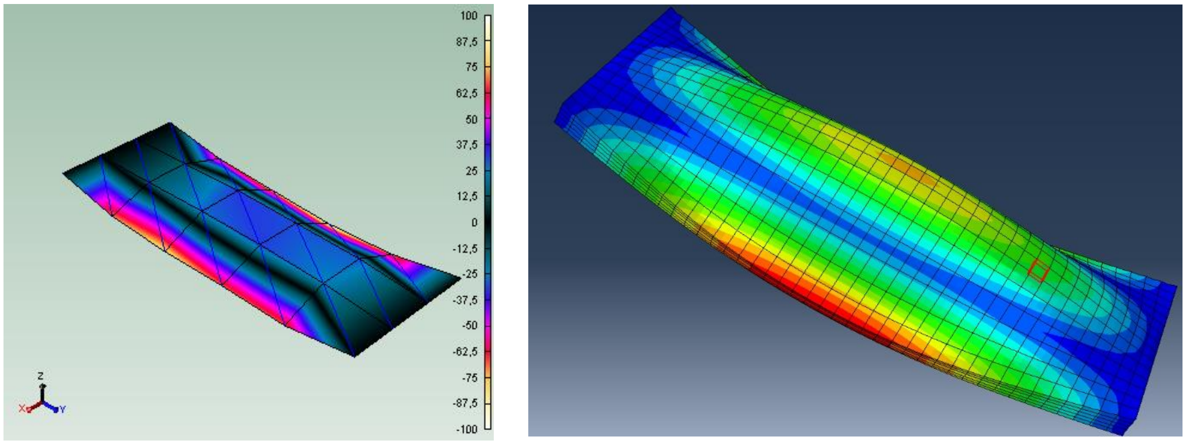

(g1) Measured 7th mode.

(g2) Simulated 7th mode.

Figure 4.11: Measured and simulated modes.

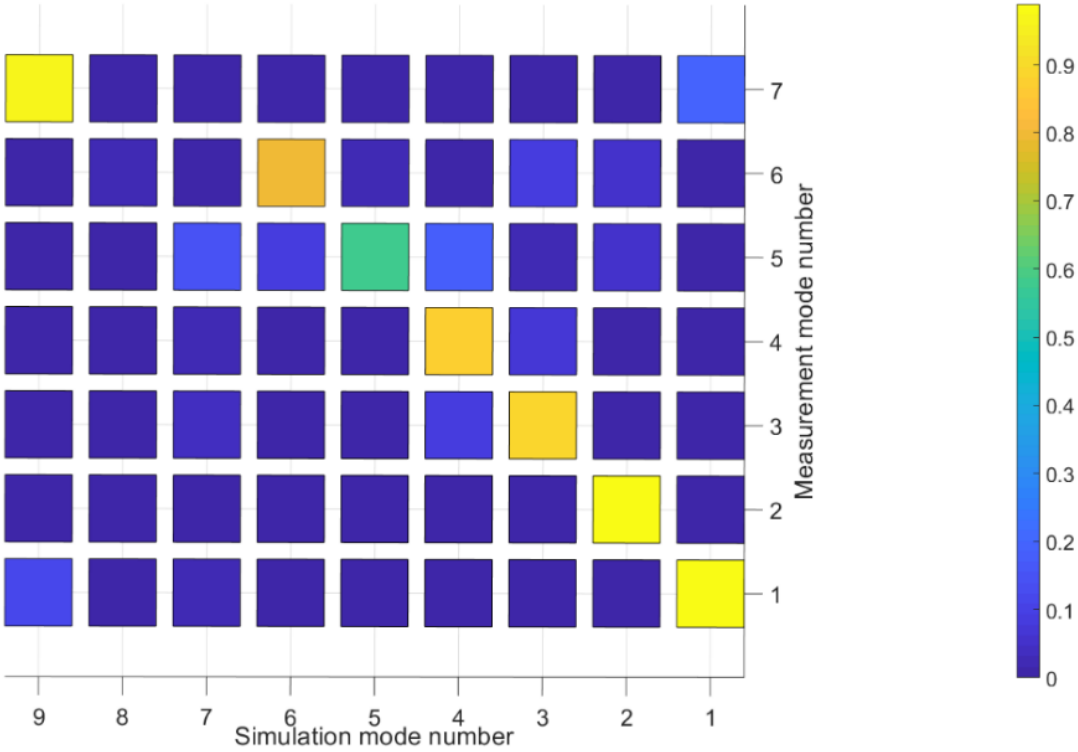

Figure 4.12: Cross-MAC.

Table 4.2: Material Properties of CLT used in the calibrated FE model.

E_1	E_2	E_3	G_{12}	G_{13}	G_{23}	ν_{12}	ν_{13}	ν_{23}	ρ
13396	4712.5	4681.6	974.6	63.64	60.46	0.3	0.3	0.4	520

* Stiffness parameters have the unit of MPa and the density is given in kg/m^3.

Table 4.3: Measured and simulated eigen-frequencies of the bending modes and the measured corresponding damping ratios.

Mode	Simulated eigen-frequency	Measured eigen-frequency	Damping ratio
1	19	19.8	4.9
2	33.2	32.2	3.6
3	58.3	56.7	3.2
4	72.5	73.8	3.2
5	100.8	91.0	3.3
6	117	125.5	2.8
-	131	-	-
-	150	-	-
7	173.9	170.4	1.2

* The simulated and measured eigen-frequencies are in Hz and the damping ratios are shown in percentage (%).

The same results can also be seen in the mobility of different excitation points of the lowest NRFD values (cf. Figure 4.13). The simulated FRFs at these four different excitation points correlate better with the measured ones, while there are extra peaks and eigen-frequency shifts in the simulated FRFs in the frequency range from 110 Hz to 170 Hz. We suspect that these discrepancies higher than the 110 Hz result from the over-simplified homogenous laminated FE model, which ignores the geometrical details contained in the real CLT panel. Yet, the boundary condition set-up in the model could not describe the real measurement boundary conditions. In Table 4.2,the calibrated E_1 is slightly higher than the measured E_1 documented in the reference [58]. However, the calibrated Young's moduli in the other two directions, E_2 and E_3, are much larger than the reference. There are two possible reasons. Firstly, the model is not perfect. We may have numerical errors since we don't know the bending functions included in the software. Furthermore, the material properties of the CLT panel given by Zhou et al. [58] are the material properties of the entire CLT panel, whereas the calibrated material properties in this work are for each layer of the CLT. Furthermore, only 4 measured elastic constants are given by the method of Zhou. The measured entire panel elastic constants can only be the index to calibrate the model.

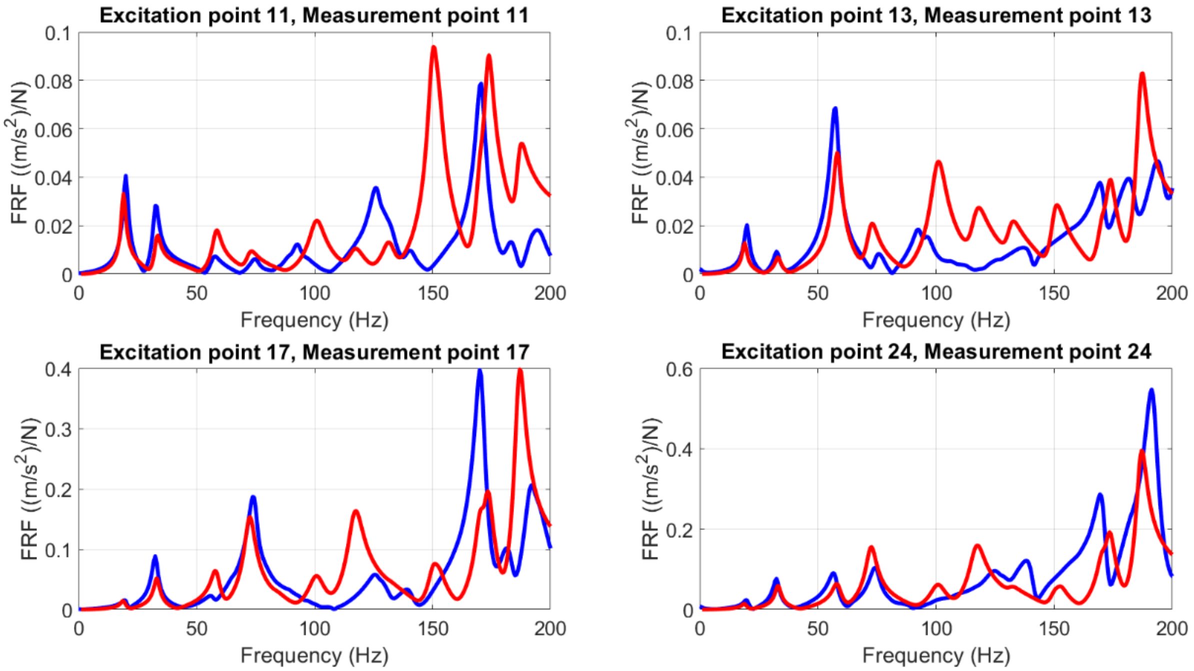

Figure 4.13: Magnitude of the complex mobility in the vertical direction of points 11, 13, 17, and 24. Simulated FRFs in red, measured FRFs in blue.

The dynamic properties of wooden structures highly depend on the material properties of the structure, the geometry details, and the workmanship. Consequently, the deterministic model may not be able to represent the dynamic response of the wooden structures in a realistic way. A calibrated model may not be able to accurately predict the dynamic behavior of the theoretical identical wooden structure due to the uncertainties. The stochastic method is applied in this case to quantify the uncertainties induced by material properties so that this model can estimate the dynamic response of a class of wooden structures, instead of only one structure. Moreover, the influence of material properties on the vibration of CLT is the coupling effect of Young’s moduli and shear moduli in all directions, so that calibration is always time-consuming and tedious work to find the appropriate combination of elastic constants in different directions. The calibration employing the stochastic approach could start from the material properties collected from the literature and set the mathematical and physical constraints to generate the input data to find the best combination of the mechanical constants of the structure. This method could automate the calibration step to avoid repetitive manual calibrations. However, we should pay attention to the mathematical and physical constraints before generating the input elastic constant data. Because the generated elastic constants should be in a reasonable range of the material. Otherwise, the input elastic constants may not have a physical meaning, even though the calibration results fit well with the reference. The stochastic method uses a large amount of data to describe an unknown problem (the database of CLT in our case). More calculations are made, and more accurate calibration can be achieved. However, a trade-off between the calculation time and the accuracy of the result should be made in order to keep the calculation time in a reasonable range. This method can not only be applied to CLT but also can be employed to calibrate the other wooden structures whose stiffness constants are difficult to obtain.

Furthermore, one of the objectives of this stochastic approach is to calibrate the material properties of the target structure. It would be better to decrease the influence of other influence factors, such as boundary conditions. Therefore, it is suggested to hang up the structure (free-free boundary condition) or fix the structure boundary to the ground (perfect simply supported condition) to eliminate the influence of boundary conditions as far as possible. In the work reported here, due to a lack of support materials, the CLT panel just laid on top of the I-steel beam and it was not screwed into the ground. Consequently, when the CLT is excited, the deformation of the I-steel beam can affect the vibration of the CLT slab. Furthermore, the laboratory boundary conditions are always different from the in-situ boundary conditions [128]. Thus, it would be necessary to investigate the dynamic response of CLT in a real building. To achieve that, the FRFs could be first measured from a CLT bare floor in real mounting conditions. Then, the same CLT bare floor could be set in the simplified laboratory conditions to compare the relative differences between different FRFs under different boundary conditions.

From the FE CLT modeling perspective, the model validation criteria (NRFD and MAC) and the simulated FRFs suggest that dynamic behavior of the CLT panel can be modeled by the homogenous orthotropic laminated FE model in the frequency range lower than 100 Hz. In a higher frequency range, as the inhomogeneity of the laminated layers of the CLT slab begins to pronounce in the vibration of the CLT panel, more geometrical details in the CLT panel should be taken into account in the FE CLT model to obtain more accurate results.

4.7. Conclusions

Low-frequency sound insulation is always a challenge for the wooden constructions, especially for multi-family dwellings. Even though the wooden constructions are satisfied with the standards in force, acoustic comfort is not always met. Since the evaluation frequency range even with the adaptation term of the current standards is from 50 Hz to 3150 Hz, however, the first few resonance frequencies of the wooden floor, which are believed to cause most annoyances, are left out of the evaluation scope. Low-frequency prediction tools are needed to access the vibratory performance of wooden buildings at the early design stage due to complaints coming from the inhabitants in wooden buildings. Accessing an accurate low-frequency prediction tool requires involving the structure details in the model. Moreover, material properties are another important factor, which can induce a remarkable change in the modeling output.

In this chapter, we introduced the stochastic process into the FE model to quantify the uncertainties generated by the material properties. By performing Monte Carlo simulations, variation of Young's moduli and shear moduli in different directions were taken into account in the FE model to investigate the coupling effect of different elastic moduli on the dynamic response of the structure. 100 simulations were calculated at 4 different driving points. Clear envelopes can be observed from the simulations lower than 100 Hz. However, the simulations begin to scatter in the frequency range higher than 100 Hz. The best combination of material properties was selected from 100 different combinations of elastic constants to calibrate the FE CLT model. From the promising results, it was concluded that the stochastic method can be applied to a deterministic model (FE model) to quantify the uncertainties of the structures. Furthermore, this method can be employed to calibrate the FE model to acquire the material properties of the under-investigated structure.

We also have to mention that an investigation of the sample size of the Monte Carlo method should also be carried out. Generally, the more numbers are generated, the more precise will be the answer [18]. In order to determine the sample size, we should know that the quantity to be determined; the allowable errors in the estimate; the confidence level to be associate with the preceding error [129]. This step should be done in the future work.

CHAPTER 5 MODELLING OF THE CONCRETE-CLT FLOOR

This chapter is dedicated to the article entitled "*Development of a Numerical Model for Predicting Low-frequency Dynamic Behavior of a Floating Timber-Concrete Floor*" to be submitted.

Résumé

Prédire le comportement vibro-acoustique du plancher est une étape cruciale dans la prévision du niveau de pression acoustique générée par le plancher. L'objectif de ce travail est de développer un modèle numérique capable de prédire le comportement vibro-acoustique d'un plancher Cross Laminated Timber-béton. Pour ce faire, l'Experimental Modal Analysis a d'abord été réalisée sur le plancher Cross Laminated Timber seul afin de collecter les informations dynamiques du plancher, qui ont ensuite été considérées comme une référence pour calibrer le modèle FE. Par la suite, les mêmes mesures ont été effectuées sur le plancher flottant pour obtenir les fréquences propres, les modes, les rapports d'amortissement ainsi que les Frequency Response Functions afin de valider le modèle établi. Les effets des différentes propriétés des matériaux sur la réponse dynamique du plancher ont été étudiés. Il a été conclu que la réponse dynamique du plancher flottant était très sensible aux propriétés des couches résilientes ajoutées entre le plancher de béton et le plancher structural en Cross Laminated Timber. Une plus grande attention devrait être accordée aux propriétés de la couche élastique afin d'obtenir un modèle de prédiction plus précis.

Mots clés : bruit d’impact en basse fréquences vibro-acoustique; bâtiment en bois; modèle de prédiction par la méthode éléments finis; plancher flottant.

Abstract

Predicting the vibro-acoustic behavior of the floor is one crucial step towards predicting the sound pressure generated by the floor. The objective of this work is to develop a numerical model that can predict the vibro-acoustic behavior of concrete-Cross Laminated Timber floor. To achieve that, the Experimental Modal Analysis was first carried out on the Cross Laminated Timber bare floor to collect the dynamic information of the floor, which were considered as a reference to calibrate the FE model afterward. Then, the same measurements were conducted on the floating floor to obtain the eigen-frequencies, the modes shape, the damping ratios as well as the frequency response functions in order to validate the established finite-element model. The effects of different material properties on the dynamic response of the floor were investigated. It was concluded that the dynamic response of the floor is very sensitive to the properties of the resilient layers added between the concrete up the floor and the Cross Laminated Timber structural floor. More attention should be paid to the material properties of the resilient layer in order to obtain a more accurate prediction model.

Keywords: low-frequency range impact sound; vibro-acoustics; wooden building; finite-element prediction model; floating floor.

5.1. Introduction

Low-frequency impact noise is always desirable to be improved in wooden dwellings. It is known that most of the sound radiation comes from the bending waves propagating through the floor [40]. One basic solution to improve the sound insulation performance of the floor is to decrease the mobility of the floor, which can be achieved by modifying the elastic moduli, the density and the thickness of the materials used in the floor [130]. Likewise, increasing damping can also reduce the resonance amplitude of the mobility of the floor. However, it is not an easy task to design material properties, like the elastic moduli, the density, the damping, etc. Increasing the thickness of a floor can improve the sound insulation, but it is not economically attractive (more production costs and reduction of construction space) and it goes counter one of the main advantages of the wooden buildings (i.e., being light). Thus, a floating floor system is often introduced in practice to decrease the impact sound transmission without changing the structural design. In general, a floating floor consists of a structural floor, a floating slab and a continuous/non-continuous elastic layer in between, shown in Figure 5.1. The rigid floating slab is supported by an elastic resilient layer that can decouple the structures and subsequently reduces vibration transmission [97]. The under-investigated floor in this chapter is a concrete-CLT floating floor, shown in Figure 5.2, which leaves the timber showing up on the ceiling, addressing the requirement of industrial partners.

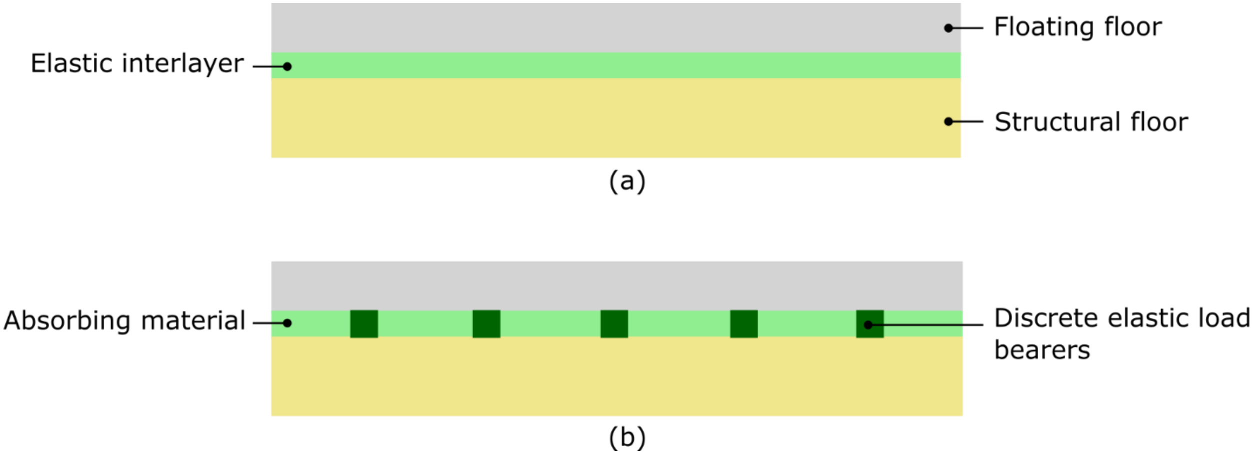

Figure 5.1: Two types of floating floor: (a) Floating floor with the continuous elastic interlayer; (b) Floating floor with a discontinuous elastic interlayer.

Figure 5.2: Compositions of the floating floor. Materials from the top to the bottom: concrete; insulation layers; gypsum boards; CLT panel.

5.1.1. Aims and Outline of the Chapter

An impact source makes the floor into movement in the upper volume. This vibration is transmitted from the upper floor to the lower ceiling. The sound perceived by humans in the lower volume is radiated by the vibrating ceiling. Thus, the dynamic behavior of a floor is one crucial intermediate step to understand the impact sound insulation performance of the floor. To that end, the aim of this chapter is to develop a FE model to predict the vibro-acoustic behavior of the concrete-CLT floating floor. Based on the developed model, the effects of different material parameters on the dynamic response of the floor should be investigated. And these investigations should be able to provide the initial quantitative recommends reducing the mobility of the floor which is one fundamental solution to improve the impact sound performance of the floor.

This chapter consists of three main parts: EMA on the Concrete-CLT Floating Floor, FE Model Development of Concrete-CLT Floating Floor and Results and Discussions. In the measurement phase, EMA was carried out on the floating floor to collect the dynamic properties of the concrete-CLT floor. These recorded data were considered as references to calibrate and to validate the model. In the model development phase, sensitivity analysis of material parameters and connection modeling investigation were performed in order to obtain relatively accurate simulation results. The simulated results and measured ones are discussed in the last section.

5.2. EMA on the Concrete-CLT Floating Floor

The investigated structure consists of one CLT slab, two layers of gypsum board, two layers of insulation material and one concrete slab on the top as shown in Figure 5.2. It is worth to mention that the gypsum boards added on the top of the CLT is to add mass to the floor. This floor composition is close to the floor solution in real life. The EMA tests were performed on the floating floor to collect the dynamic properties (the eigen-frequencies, the mode shapes, the damping ratios, and FRFs) of the floor in order to validate the numerical model. The size of the EMA test grid has been decided according to the highest frequency of interest. Theoretically, one accelerometer and one hammer are enough to conduct the EMA test and obtain all the useful information. In our case, in order to increase the consistency and credibility of the measurement results, three accelerometers were randomly attached to the top of the floating floor and the other two were attached under the CLT panel since we only have five accelerometers. And the accelerometers attached under the CLT panel are all along the edges. This is due to the fact that the distance between the bottom of the CLT and the ground is only around 20cm. It is easier to attach the accelerometers along the edges.

In this chapter, the EMA test procedure wouldn’t be described again since the EMA hammer test procedure is as the previous chapter. More details of the EMA tests please refer to chapter MODELLING OF THE DYNAMIC BEHAVIOR OF THE ISO TAPPING MACHINE.

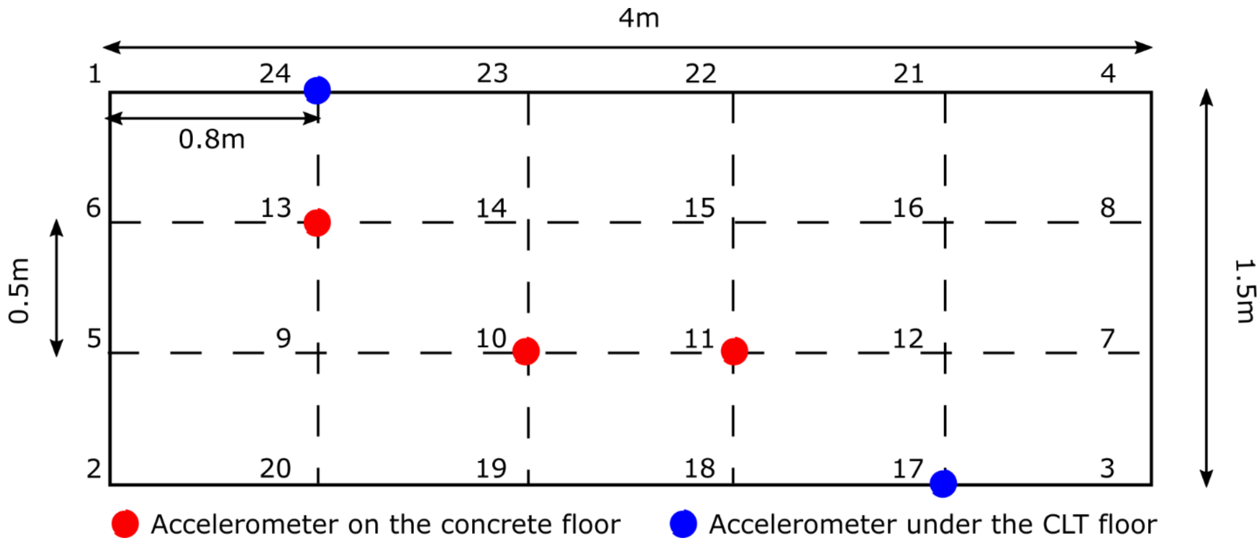

Figure 5.3: Accelerometer positions in the EMA test on the floating floor.

The experimental tests performed on the floating floor aim at collecting the eigen-frequencies, the mode shapes, the damping and the FRFs of the upper concrete floor and the FRFs of the lower structural CLT floor. In this study, two layers of gypsum board of 12.5 mm, two layers of impact board of 15 mm as well as 60 mm C25/30 concrete were added on the top of the CLT floor, as shown in Figure 5.2. At the initial stage, modal tests were planned to carry out step by step on the floating floor (i.e., when adding each material) in order to investigate how the added materials, affect the dynamic response of the floor.

However, when the first layer of the gypsum board was placed on the top of the CLT, cf. Figure 5.4, not enough dynamic information could be extracted. Only two modes, shown in Figure 5.5, were caught. This is owing to the weak connection between the CLT and the gypsum board, as there is no adhesive added between the CLT and the gypsum board. Furthermore, the gypsum board isn't heavy enough to compress itself to the CLT floor. When the resilient layer was added on the top of the gypsum board, shown in Figure 5.4, the FRFs were even worse (no resonance) due to the low stiffness and high damping characteristics of the resilient layer as well as the soft surface. As a consequence, the force could barely be transmitted to the bottom part of the floor.

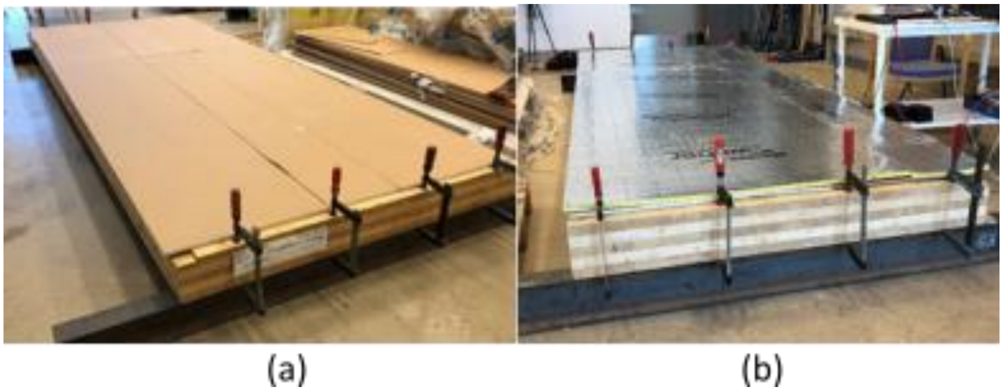

Figure 5.4: (a) Gypsum board on the top of the CLT floor; (b) Resilient layer and gypsum board on the top of the CLT floor.

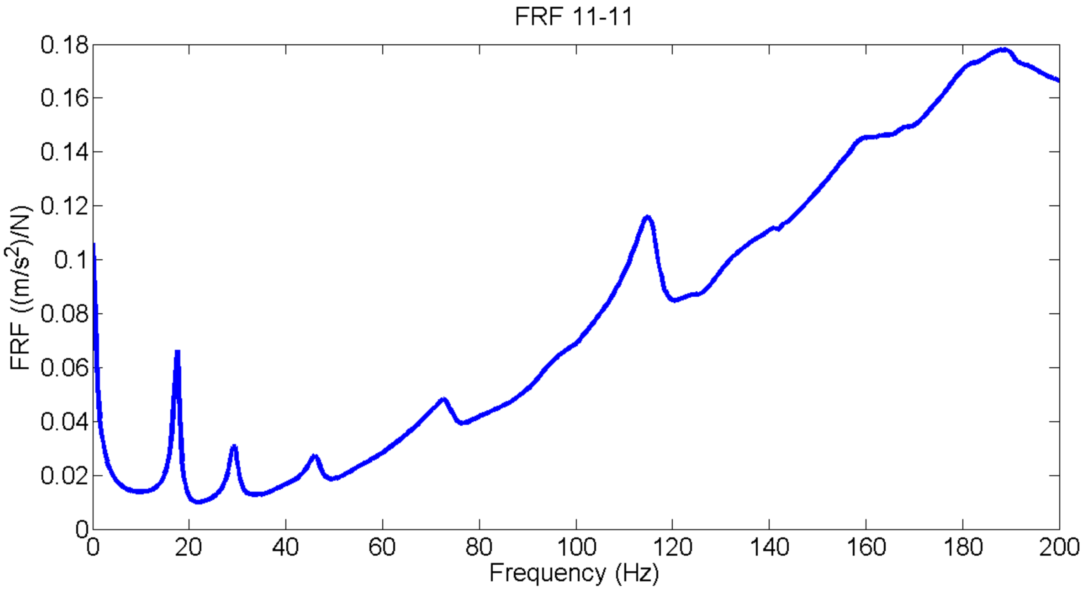

Figure 5.5: FRF at point 11 of the gypsum board-CLT floor.

Due to the difficulties mentioned above, the modal test was only conducted on the floating floor, as the concrete can enforce the connections between the different layers because of its higher weight. The FRFs at the bottom of the floor should also be collected to calibrate the model, as these FRFs can validate the vibration transmission paths which are the previous step to radiate sound from the bottom of the floor. To do so, three accelerometers were attached to the top of the concrete surface, while two accelerometers were attached to the bottom of the CLT, cf. Figure 5.3. The test equipment and the mesh grid were the same as the modal test on the CLT floor, except that the nodes on the shorter edges of concrete were also hit. Since the concrete was just placed on the top of the resilient layer, without adhesive in between, it was “floating” on the elastic layer, implying that no strong restrict was set on the concrete slab. So, when the floor is excited by an external force, the accelerations on the four edges are not 0. The measured eigen-frequencies and the corresponding damping ratios are shown in Table 5.1.

Table 5.1: Measured eigen-frequencies of the bending modes and the measured corresponding damping ratios.

Mode	Measured eigen-frequency	Damping ratio
1	12.2	5.6
2	14.6	11.8
3	19.7	21.8
4	23.1	20.6
5	29.4	11.6

6	41.9	8.0
7	51.2	7.0
8	72.3	5.2
9	74.5	2.1
10	99.4	3.4
11	109.1	1.6
12	115.9	2.4
13	126.1	1.7
14	150.0	2.5

* The simulated and measured eigen-frequencies are in Hz and the damping ratios are shown in percentage (%).

5.3. FE Model Development of Concrete-CLT Floating Floor

The sensitivity analysis is performed in the first place to investigate how the different material properties affect the dynamic response of the FE model. The material properties which have the most important effects will be calibrated in the following steps in terms of different error metrics (the definitions of NRFD and MAC, cf. MODELLING OF THE DYNAMIC BEHAVIOR OF THE ISO TAPPING MACHINE). Then, the modeling method of the connections of different layers of the floor is developed and the model is validated by comparing the simulated and measured dynamic properties of the floor.

5.3.1. Model description

The FE model consists of four different parts: the concrete panel, the resilient acoustic insulation layer, the gypsum board layer and the CLT panel, shown in Figure 5.6. The dimension of this model is established according to the real dimension of the materials used in the experiments. In this model, each ply of the CLT panel is orthotropic, whereas the other materials involved in the floor are all considered as homogenous and isotropic materials. The CLT model is established according to the chapter STOCHASTIC CALIBRATION PROCEDURE. The boundary conditions will be defined as the same as the CLT model. Three direction displacements at one side are restrained and on the other side, the vertical direction is released. The reason to keep this boundary condition is that this modelling method can provide the most accurate results for the CLT panel. Changing the boundary conditions in the model can modifying the dynamic response of the CLT panel and it can potentially decrease the accuracy of the CLT-concrete model. For more details about the CLT boundary conditions, please refer to STOCHASTIC CALIBRATION PROCEDURE.

In general, the dynamic behavior of a visco-elastic material can be modeled in terms of the frequency-dependent dynamic stiffness property of this material [131]. However, the manufacturer’s datasheet of the acoustic insulation material employed in this research only provides a single value of the dynamic stiffness instead of the frequency-dependent values. Furthermore, we lack dynamic stiffness measurement equipment. As a result, the acoustic insulation material is modeled as an isotropic material in Abaqus. In [49], the authors used Ansys as modelling software. In this software, many springs can be evenly assigned to the surface of the element. But Abaqus doesn't have this function. The spring can only be assigned from one point to the other point. In this floating floor system, we consider that the insulation layer acts like a vertically aligned spring. Furthermore, we tried with another modelling approach to simulate the dynamic response of this floor. We removed the resilient layer. The concrete floor was applied directly to the gypsum board layer. The interaction between these two layers was assumed to be "linear-interaction" in Abaqus. In this case, the "Contact stiffness" acts as the spring to replace the resilient layer. But the "Contact stiffness" has a really big value which is much bigger than the dynamic stiffness provided by the manufacturer's datasheet. Although this approach can provide a relatively good result, it may be lacking some physical meanings. So, we decided to model this floating floor with a resilient layer even though considering the resilient layer as an isotropic elastic material is an over-simplified way to describe this material. But under the conditions we have, this is the best solution.

The material properties of the concrete, the acoustic insulation layer, and the gypsum board were collected from the standard [132] and the manufacture technical data sheet [133, 134], reported in Table 5.2. The mesh size is set to 0.1 m which satisfies the rule of the 6 - 8 nodes per wavelength, i.e., the highest frequency of interest is 200 Hz can be resolved accurately. 20-node quadratic brick (C3D20) elements were assigned to the entire model.

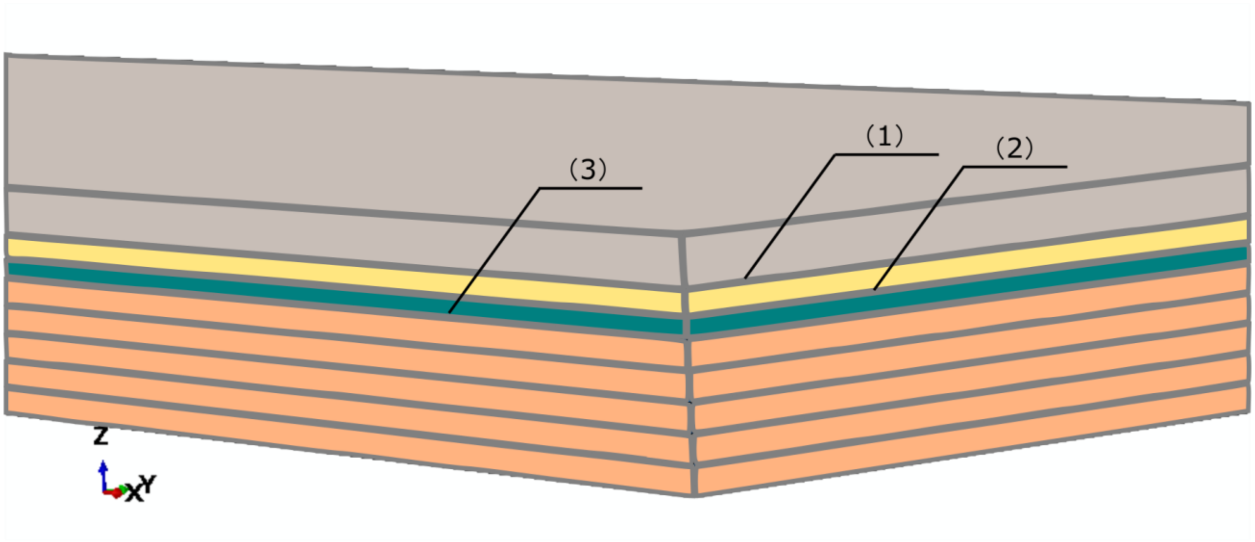

Figure 5.6: FE model with different materials and the connections: (1) Concrete-acoustic insulation layer connection; (2) Gypsum board-acoustic insulation layer connection; (3) CLT-gypsum board connection.

Table 5.2: Material properties of gypsum board and acoustic impact board collected from the literature.

	$\boldsymbol{\rho}$	E	$\boldsymbol{\upsilon}$
Acoustic insulation	86	0.225	0.2
Gypsum board	1120	7000	0.2
Concrete	2500	31000	0.2

* Stiffness parameters have the unit of MPa, the density is given in kg/m^3, and the Poisson ratio is dimensionless.

5.3.2. Model calibration

In the experimental phase, three accelerometers were placed on the top of the floor while two accelerometers were located at the bottom of the panel to obtain the dynamic information, cf. EMA on the Concrete-CLT Floating Floor. The eigen-frequencies and the mode shapes, as well as the FRFs of the concrete upper floor, were obtained and it is interesting to find that the upper floor and the structural floor react independently to the force due to the large mass added on the CLT panel. Therefore, the dynamic response of the concrete-CLT floor at the bottom is different from the one of the bare CLT floor. Furthermore, the force is attenuated very fast so that not enough force is transmitted to the lower slab (CLT panel). As a consequence, the modes are changed (twisted or vanished) and not all the modes are excited. Thus, for the upper floor, the calibration is based on the eigen-frequencies, the mode shapes, and the FRFs. For the lower panel, only the measured FRFs are compared.

5.3.2.1. Sensitivity Analysis and Connection Investigations

The sensitivity analysis aims at investigating the influence of different material properties on the dynamic behavior of the floor and to obtain useful information to calibrate the model afterward. The sensitivity analysis focusses on the material parameters investigations so that the connections between each different material are kept rigid throughout the sensitivity analysis to exclude the connection effects in the parameters' sensitivity analysis. The material properties of the CLT floor coming from the previous chapter STOCHASTIC CALIBRATION PROCEDURE will not change throughout the investigation. Each parameter is increased by 10% of the initial values reported in Table 5.2 in order to investigate how the different parameters influence the dynamic behavior of the model with the same percentage of increase.

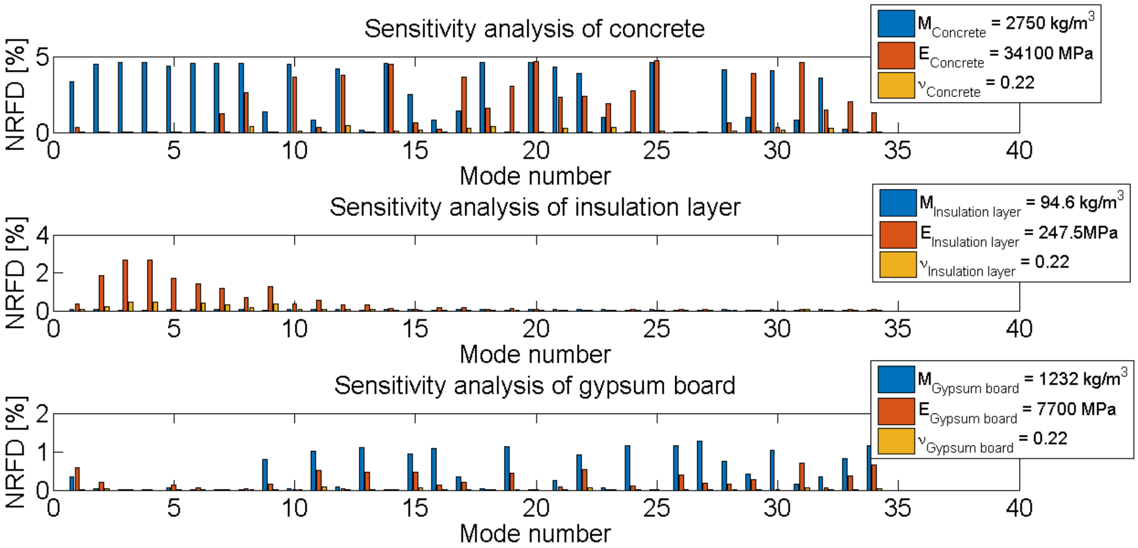

Figure 5.7: Sensitivity analysis of the FE model.

It can be observed from Figure 5.7 that among all the tweaked parameters, the mass density and Young's modulus of the concrete have the most important influence on the eigen-frequencies. This effect is owing to the fact that concrete is one of the most important components involved in the floor due to its huge mass. Following the mass density and Young's modulus of the concrete, Young's modulus of the acoustic insulation layer is the second important parameter that can affect the eigen-frequencies of the model, especially for the first several eigen-frequencies. In spite of having a small mass, the acoustic insulation material has an important impact on the dynamic response of the floor due to its low stiffness. This floating floor can be considered as a mass-spring system whose resonance frequency largely depends on the stiffness of this spring. In this case, Young's modulus of the acoustic insulation layer has to be calibrated in the following steps. The rest NRFDs of the other parameters are lower than 1%.

Thus, in the following investigations, Young’s modulus and the mass density of the concrete, as well as the stiffness of the insulation layer, are tweaked until a relatively good NRFD and MAC obtained.

Besides the material properties, the connection between different materials is another important factor to mimic the dynamic behavior of floors. Different attempts of the connections in the FE model are made in order to correctly simulate the dynamic response of the concrete-CLT floor. It should be noticed that the material properties should be kept constant throughout the connection investigation to exclude the influence of material parameters. There are three different connections, cf. Figure 5.6: (1) CLT-gypsum board connection; (2) Gypsum board-acoustic insulation layer connection; (3) Concrete-acoustic insulation layer connection. The connections between each different layer are not rigid since there is adhesive added. But they are not totally free neither, as the concrete slab is heavy enough to compress all the materials towards the structural panel. So, the rigid connections are too strong restricts to describe this connection, whereas it is too weak to define all connections as pressure-overclosure contact in the FE model. The hybrid connection relation is more reasonable to describe the contacts between different materials on this floor. Thus, the connections (1) and (3) were fully tied together and a pressure-overclosure linear interaction characterized by “Contact stiffness” is assigned to the connection (2).

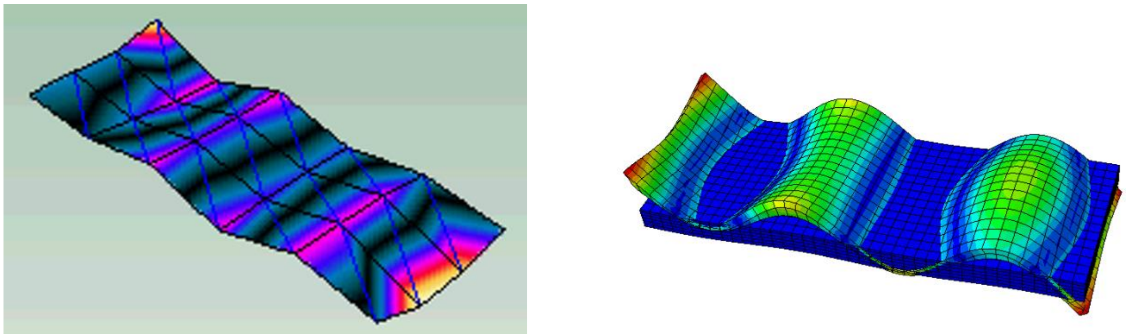

Figure 5.8: 12th measured mode and 12th simulated mode.

5.3.2.2. Model Validation

To validate the entire model, not only should the NRFD and MAC be compared but should the FRFs of different input and output positions be justified. Due to the later, the “Steady-state dynamics, Modal” step is used to calculate the FRFs. Meanwhile, the Rayleigh method introduced in the FE model is defined as: $\zeta_n = \frac{\alpha}{2\omega} + \frac{\beta\omega}{2}$ [135]. The Rayleigh damping ratios ($\alpha = 18.75, \beta = 3.14 \times 10^{-5}$) assigned to the entire system in the FE model are obtained by fitting the Rayleigh damping curve to the modal damping ratios collected from the measurement data, illustrated in Figure 5.9.

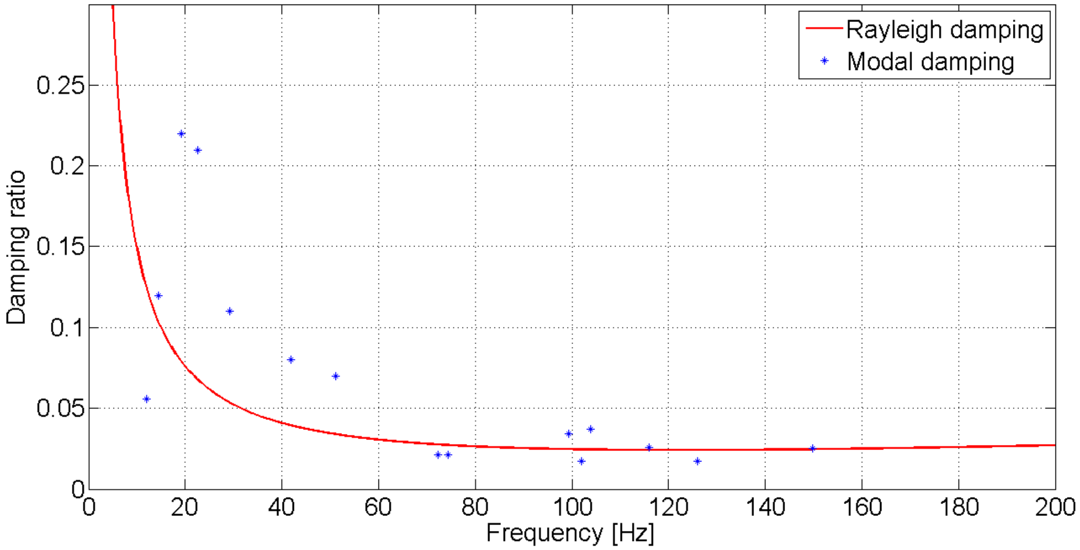

Figure 5.9: Measured modal damping ratios and fitted Rayleigh damping.

After tweaking the most sensitive material parameters as well as the interaction parameters, it is interesting to find that the calibrated material properties which are close to the material parameters collected from the literature can give the best NRFD and MAC. They also provide the relatively good FRFs. It implies that the material properties of the artificial material are easier to be controlled and designed by manufacturers than the ones of natural material, i.e., CLT. The tweaked material properties are reported in Table 5.3. The calibrated contact stiffness is of 4×10^6. The NRFDs and the MAC numbers are shown in Figure 5.10 and Figure 5.11.

Table 5.3: Calibrated material properties of the gypsum board and acoustic impact board.

	$\boldsymbol{\rho}$	E	$\boldsymbol{v}$
Acoustic insulation	86	0.225	0.2
Gypsum board	1120	7000	0.2
Concrete	2600	30000	0.2

* Stiffness parameters have the unit of MPa, the density is given in kg/m^3, and the Poisson ratio is dimensionless.

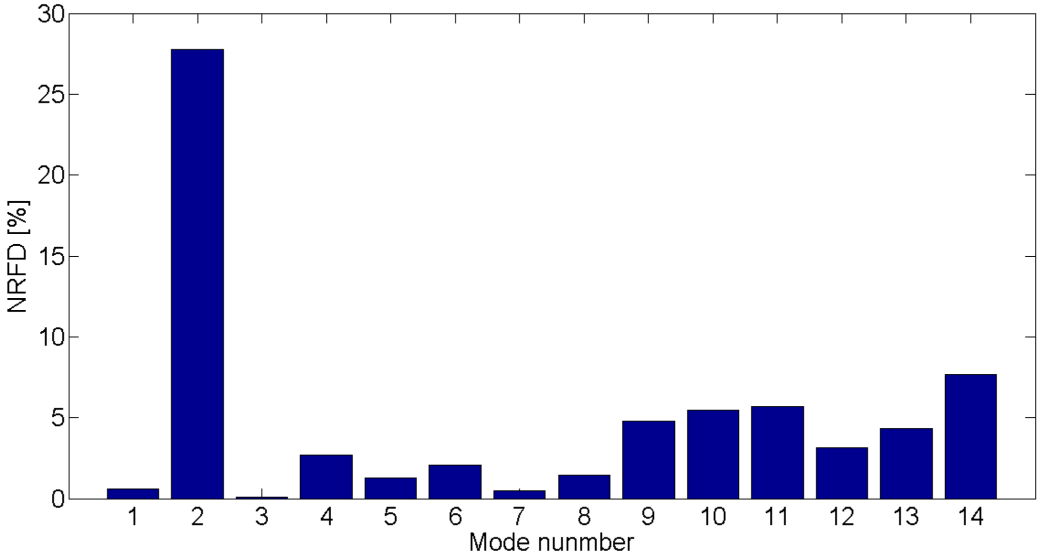

Figure 5.10: NRFD calculated based on the experimental data of the concrete floor.

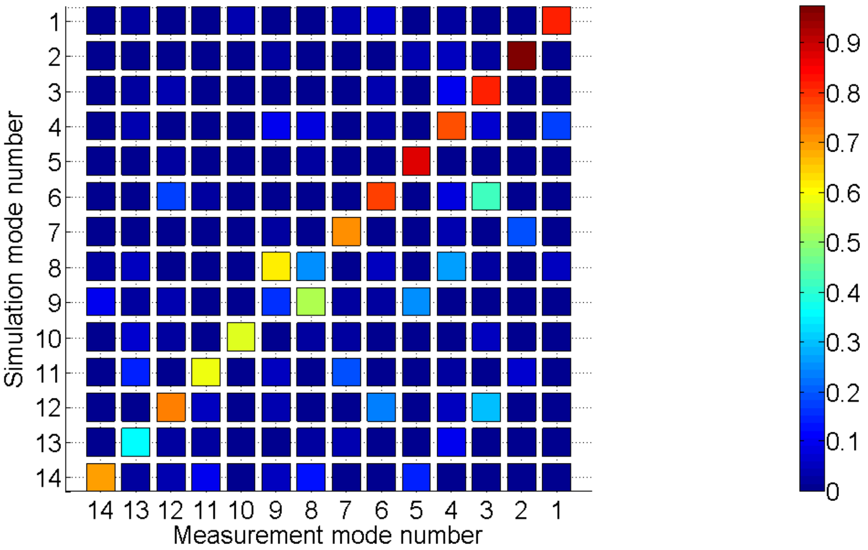

Figure 5.11: MAC calculated based on the experimental data of the concrete floor.

It can be seen from Figure 5.10 that all the NRFDs are lower than 10% except for the second mode. The MAC numbers shown in Figure 5.11 have higher values for the first several simulated mode shapes comparing to the last ones. The MAC values decrease compared to the lower order modes, which may be due to the difficulties in the measurements. The higher the order of the mode is, the more complex the mode shape becomes. This means that the deformation of the structure becomes more difficult to detect in the measurements due to the small deformations of the specimen when the frequency range becomes higher. As a consequence, the extracted higher-order mode shapes are not as clear as the lower order mode shapes, which results in the low MAC values. All in all, the high NRFD values and the high MAC values imply that these modes are captured by the established model, even though they are some shifts in the eigen-frequencies and mode shape correlations are not perfect in the higher frequency range. To further validate the model, the simulated and measured FRFs of different positions which describe the vibration transmission paths are compared in Figure 5.12 and Figure 5.13.

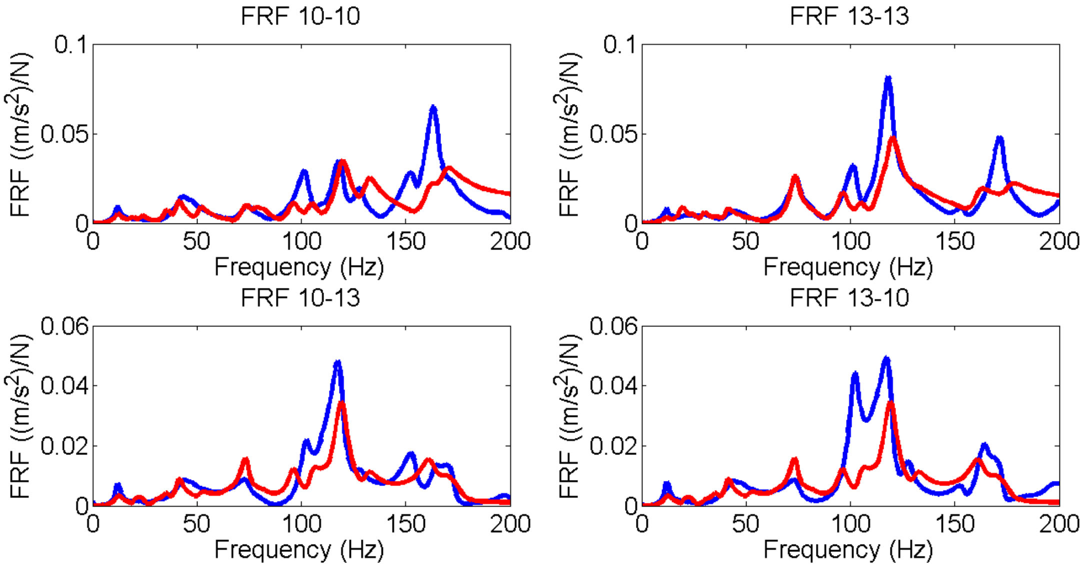

Figure 5.12: FRFs at different excitation and receiving points on the concrete floor which describe horizontal mobility. The first subscript of the FRF title indicates the excitation point and the second one refers to the receiving point. The simulation curves are in red and the measured curves are in blue.

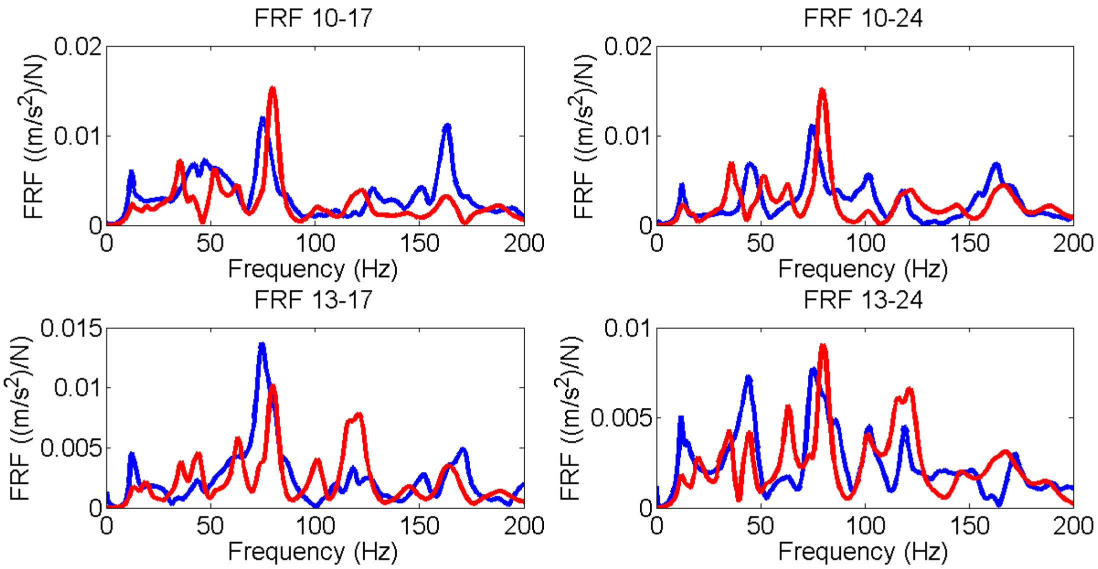

Figure 5.13: FRFs at different excitation and receiving points under the CLT floor which describe the vertical mobility. The first subscript of the FRF title indicates the excitation point and the second one refers to the receiving point. The simulation curves are in red and the measured curves are in blue.

5.4. Results and Discussions

In Figure 5.12, nearly all the main resonances are captured by the model even if there are some discrepancies in amplitudes and some shifts at certain resonance frequencies. The discrepancies of the simulated amplitudes compared with the measured ones may result from the Rayleigh damping employed in this model, which is constructed by fitting a continuous curve to the measured modal damping ratios. In this case, the Rayleigh damping ratio at each resonance frequency is not as precise as the modal damping, as it is obtained from an estimated curve. However, the aim of this research is to develop a prediction model for one sort of floor instead of just focusing on one floor. The constructed Rayleigh damping has a more generalized application. It can be used in the other modified models, like changing the thickness or the mechanical properties of the materials involved in the floor, without knowing the exact resonance frequencies or the modal damping ratios of this system. In order to have a global view of the established model, not only should the FRFs which describe the horizontal vibration transmissions be compared, but also should the FRFs representing the vertical vibration transmissions, reported in Figure 5.13, be investigated. The excitation and receiving positions of the transmission FRFs refer to Figure 5.3. The main resonances of the system can be found in the simulation curves in Figure 5.13. Nevertheless, more eigen-frequency shifts are found in Figure 5.13 than in Figure 5.12, especially in the frequency range higher than 150 Hz. The discrepancies between the simulations and the measurements may be caused by the over-simplified modeling method of the resilient material. The resilient material should have been modelled as the viscoelastic material instead of inserting an isotropic material between the concrete floor and the gypsum board. But due to the lack of the information in the manufacturer datasheet and the lack of the dynamic stiffness measurement equipment, the dynamic reaction of the resilient material is only modeled by an isotropic layer and an artificial contact stiffness. Another possible reason is that the gypsum boards are assumed as one continuous layer in the model, whereas, in reality, the several panels of gypsum board are placed on the top of the CLT floor. The discontinuities of the gypsum boards may interrupt the vibration transmission, resulting in the discrepancies in the simulations.

5.5. Conclusions

Knowing the vibro-acoustic behavior of floors is one crucial intermediate step towards predicting the impact sound performance of floors. This chapter focuses on developing a FE model to predict the dynamic behavior of a floating floor in the low-frequency range. To achieve that, EMA was carried out on the concrete-CLT floor in order to collect the dynamic properties of the floor and then to calibrate the FE model. The sensitivity analysis was performed to find out the most important parameters which can affect the simulation results. Then different attempts were made to model the connections between the different materials in the concrete-CLT floor. The FE model was validated by means of two different criteria and the FRFs. From the model development procedure, it is found that the connections between the different materials on this floor can be modeled by a hybrid connection relation in the FE commercial software. And the calibrated material properties of this floor, except the CLT panel, are close to the ones collected from the manufacturer's datasheet. It implies that the manufacturers have more control in the artificial materials comparing the natural material, like CLT. This model could be further improved by integrating the frequency-dependent dynamic stiffness of the resilient layer in the FE model to simulate the visco-elastic properties of the insulation material. If we want to apply this model to a more realistic case, a more complex boundary condition should be set up.

5.6. Additional Content not Presented in the Original Paper

This section is not included in the original paper. Since CLT panel in the acoustic chamber failed to provide useful measurement data to validate the model. Only simulation results are presented and discussed. The work presented in this section aims at providing more simulation ideas for the future work.

5.6.1. ISO Tapping Machine Model Development

The ISO tapping machine model is developed in the previous research [136], however, only one hammer of the tapping machine is modeled. In this work, the same force modeling method is employed, but the hammer number is extended to five. The input force generated by one hammer can be derived from the FRFs and the measured accelerations:

$$F_{14} = \frac{A_{13}}{FRF_{14-13}}, \tag{5-1}$$

where A_{13} is the response accelerations at Point 13 generated by the one hammer at Point 14, F_{14} is the force generated by one hammer at Point 14 and FRF_{14-13} is the frequency response function related to the input force at Point 14 and the response accelerations at Point 13. It is assumed that five hammers don't interfere with each other. Hence, the accelerations generated by five hammers at one point other than the excitation point can be written as:

$$A_j = \sum_{i=1}^{5} FRF_{14(i)-j} \times F_{14(i)}, \tag{5-2}$$

where A_j are the accelerations at the point of interest, $FRF_{14(i)-j}$ is the frequency response function related to the input force generated by i^{th} hammer at Point 14 and the accelerations at Point j and $F_{14(i)}$ is the input force at Point 14 generated by i^{th} hammer.

The accelerations at Point 13 generated by 5 hammers are shown in Figure 5.14 (a). From the accelerations at Point 13, $F_{14(i)}$ can be deduced according to Equation (5-1) and the

$FRF_{14(i)-j}$ can be acquired from the previous established FE model. So, the accelerations at the point of interest can be determined.

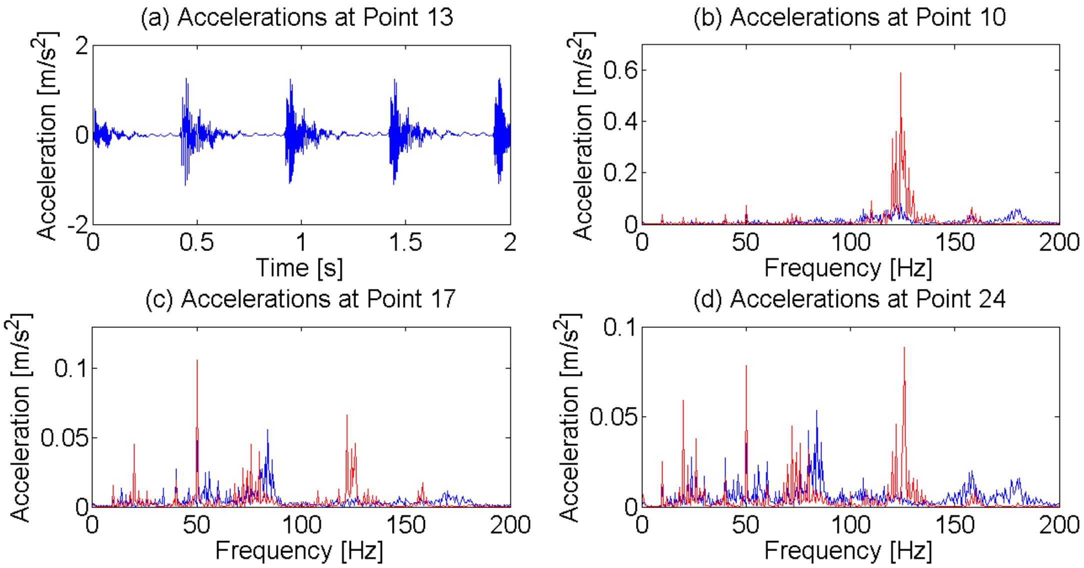

Figure 5.14: Accelerations at the different measurement points. In figure (a), the accelerations generated by one hammer; in figure (b), (c) and (d), the simulation results are shown in red and the experimental results are shown in blue.

Figure 5.14 (b) shows the accelerations at Point 10 on the upper concrete floor and the accelerations at Point 17 and Point 24 under the CLT structural floor are shown in Figure 5.14 (c) and (d). It can be seen from these three figures that the simulated accelerations in the frequency range lower than 100 Hz have nearly the same magnitudes as the measured ones. For the two receiving points under the CLT structural panel, the simulated resonance around 80 Hz has been slightly shifted to the lower frequency range. When the frequency becomes higher than 100 Hz, the over-estimated resonances can be observed in all these 3 figures. In Figure 5.14 (b), the simulated magnitude of the main resonance around 120 Hz is larger than the measured resonance. And for the 2 points under the CLT, cf. Figure 5.14 (c) and (d), there is no more resonance at 120 Hz in the measurement acceleration curves. But the resonances around 120 Hz could be seen in the simulations. The discrepancies in the simulations may result from the simulated FRFs. In fact, the FRFs of a linear system act like a “filter” or an “amplifier”. When the input signal is injected into the system, this signal is either filtered or amplified or both and then the input signal is transferred into the output signal. In our case, the input signals are not reduced enough by the simulated FRFs at 120 Hz. This floating floor system can largely decrease the horizontal vibration transmissions at 120 Hz, and it can damp out the vertical vibration transmissions at 120 Hz. This transmission feature doesn’t show up in the established FE model, which may be owing to the modeling method of the insulation material. Since the resilient layer has a more important amplitude reduction effect/damping effect in the vertical vibration transmission. However, due to the lack of information about the dynamic stiffness of the insulation material, the insulation layer’s dynamic behavior is simplified into linear interaction, characterized by a constant contact stiffness, instead of modeling the frequency-dependent visco-elastic effect. This simplified modeling method of the insulation material can be the main cause of the extra resonances in the vertical transmission simulations.

5.6.2. Sound Radiation Calculation and Impact Sound Improvement Investigation

To calculate the sound radiated by the floor, several assumptions are made:

1) The floor system is installed in an infinite rigid wall, implying that the velocity is 0 everywhere except on the floor system;

2) The sound radiation calculation is based on the far-field and free field assumptions;

3) The floor radiator can be approximated as a sum of point sources.

Under the far-field assumption and the point source assumption, the pressure radiated by a point source can be written as [40]:

$$p(f) = j\omega\rho_0 q_0 \frac{e^{-jk_0 r}}{4\pi r}, \tag{5-3}$$

where ρ_0 is the air density, q_0 is volume velocity, k_0 is the wavenumber in the air, r is the distance between the point source and the receiving point. Since we assume that the floor radiator can be represented by a sum of point sources and only half point source can radiate at the bottom of the floor, so, the pressure radiated by the floor can be expressed as the summation of the pressure radiated by point sources:

$$\begin{aligned} p(f) = \frac{j\omega\rho_0}{2\pi}\sum\frac{q_n}{r_n}e^{-jk_0 r_n} &= \frac{j\omega\rho_0}{2\pi}\sum\frac{v_n s_n}{r_n}e^{-jk_0 r_n} \\ &= \frac{\rho_0}{2\pi}\sum\frac{a_n s_n}{r_n}e^{-jk_0 r_n}. \end{aligned} \tag{5-4}$$

The displacements in three directions on the edges of the floor model and the CLT bare floor model are restricted to mimic the baffled boundary condition. The accelerations generated by the ISO tapping machine on the bottom of the floating floor and the CLT bare floor calculated by employing the calculation method in the previous sections. The calculated SPLs of different cases are portrayed in Figure 5.15.

It can be observed from Figure 5.15 that by adding the concrete topping floor and the insulation material, the impact sound insulation improvement is achieved higher than 50 Hz. The impact sound improvement ΔL is positive in the frequency range higher than 50 Hz. But the impact sound improvement is degraded below 50 Hz, even though large mass and low stiffness material are added into the system. The same demoting effect in sound pressure level improvement by adding low stiffness materials is also observed in the other research [72, 109, 137]. This effect may be due to the mass-spring system. The concrete top floor and the CLT structural floor are two masses which are connected by the “spring”, the insulation material. In this case, the floor vibration can be amplified at the resonance frequency of the mass-spring system and the impact sound insulation is subsequently degraded.

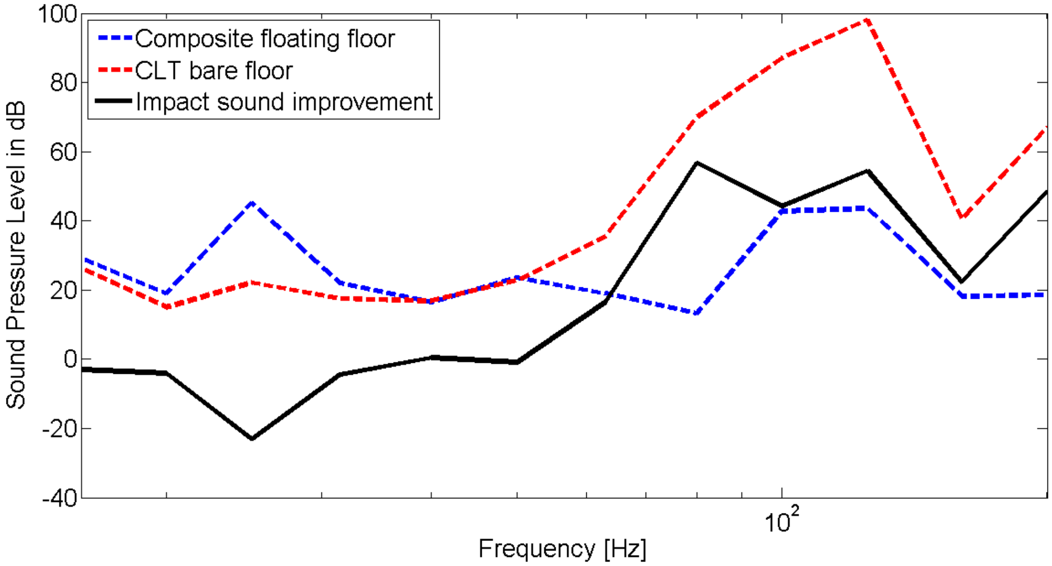

Figure 5.15: SPL generated by the floating floor is in blue dotted line and SPL generated by the CLT bare floor is in red dotted line. The sound pressure level improvement of the floating floor is the black solid line. The frequency band is in the 1/3 Octave band.

Obviously, in Figure 5.15, the levels of the simulated SPL are too high, especially when the frequency range is higher than 70 Hz. However, this model showing the tendency of the impact sound insulation improvement of a floating floor is just an initial step towards an accurate prediction model. Since this calculation model is established under the far-field and the free field assumptions. So, the room effect is not taken into consideration. Furthermore, the floor is assumed to be baffled in an infinite large rigid wall. No matter the radiation condition or the boundary condition assumptions are not the real ISO laboratory condition or the in-situ condition. More efforts should be made in addressing the boundary condition problem in simulations. And room effects, like the reflection waves and room modes, etc. should be considered in the sound radiation calculations.

CHAPTER 6 CONCLUSIONS AND RECOMMENDATIONS

6.1. Conclusions

In the frame of this research, different studies were performed to develop a low-frequency range impact sound insulation prediction model of the CLT-concrete floor. To achieve that, the research follows the sound generation and transmission procedure. The impact source was firstly investigated. The vibration transmissions of different types of floors were then modelled. The sound radiated by the floor was calculated under certain strict assumptions by combining the previously developed models and methods. The following conclusions can be drawn from the research conducted in this project.

The force generated by the tapping machine can be derived from an indirect method. Instead of measuring the force directly, which can always change the contact impedance between the hammer and the floor, the force can be derived from the accelerations and dynamic response of the floor. From the force modelling validation, it was found that the accuracy of this method relates to the accuracy of the dynamic response of the floor. Further investigation of the floor was carried out.

Being a natural material, the material properties of the same species of wood can have a big variance. As a consequence, the nominally identical wooden structures can react differently to the external excitation. The stochastic method applied to the CLT model is able to quantify the uncertainties induced by the material properties of wood. The modelling results can represent dynamic responses of a sort of wooden structures. At the same time, one most accurate modelling result is chosen to retrieve the material properties of the CLT floor. The stochastic applied here can quantify the uncertainties of the wooden structure and automate the material property calibration procedure. But we should also keep in mind that this approach is only able to calculate the uncertainties induced by the material properties in the FRFs of a structure. Further calculations related to the acceleration, the sound radiation, etc. should also be made to quantify the uncertainties.

At the final stage of this project, different construction materials were added on the top of the CLT base floor. The vibroacoustic behavior of this CLT-concrete was modelled. Through the calibration of material properties of the floor, it can be observed that the calibrated material properties of other materials have much less variation than wood, implying that the manufacturers have less control in wooden elements. It was also found that the dynamic stiffness of the resilient material has a paramount impact on the dynamic behavior of the floor.

From the experimental point of view, while extracting the dynamic properties of the structure (the eigen-frequencies, the mode shapes, and the damping ratios) through the EMA tests, the boundary conditions should be well defined. Improper boundary conditions can lead to failure to extract the dynamic properties. So, the SFSF boundary condition is a suitable choice to extract the dynamic properties of the structures in order to further calibrate the FE model.

To sum up, one modelling method of input force was proposed in the first phase of this work. This method can derive the input force by measuring the accelerations of the structure.

However, the accuracy of the simulated accelerations should have been improved by increasing the different measurement positions. Following this, we found that the base floor model has impact on the simulation results. To further increase the accuracy of the simulation results, the stochastic approach was employed to calculate the uncertainties induced by the material properties in the dynamic response of the structure. But here we only investigated the uncertainties of the dynamic response of the structure (FRF). The uncertainties in the accelerations or in the sound radiation weren't calculated since only one leaf of CLT under simply supported boundary condition was tested. In the last section, the concrete-CLT floor was modelled. The main resonances were captured by the model. However, the discrepancies between the measurement and simulation results can be obviously observed. These discrepancies may be caused by the inaccurate input data, i.e., the dynamic stiffness of the resilient material. This research is only one step towards an applicable and accurate prediction model.

6.2. Recommendations

To establish a more practical and more accurate prediction model, boundary conditions and material parameters are crucial factors. Since each log of wood is unique, material properties of wooden elements can have a big variance even though the wooden elements have the same wood species. As a consequence, the FE models of wooden structures always need to be calibrated in terms of material properties. A common method to extract the dynamic properties of the structure which are considered as references to calibrate/validate the model is the EMA test. So, the calibrated material properties will highly depend on the results of the tests and the data quality of the EMA test. In this case, how to obtain high-quality data becomes paramount important to obtain the material properties of the tested structure. Regarding the research reported in this thesis, the EMA tests are sensitive to the boundary conditions. So, in order to obtain more reliable data, the SFSF boundary conditions are recommended. Or, Free-Free-Free-Free conditions can also be tried since these boundary conditions are easier to be modelled afterward. But it should be noticed that the eigen-frequency of the springs to support the structure to set the structure free should be much lower than the first resonance frequency of the structure in order not to change the response of the under-tested element. In the last section of chapter 5, a method to describe the force generated by 5 hammers was proposed. However, the modeling results are not accurate enough. So, to further validate this method, the base floor where the tapping machine is placed on should be changed into a simpler floor, in order to decrease the inaccuracy coming from the base floor. And for the low-frequency issue, another suitable source should be used.

The dynamic stiffness of the resilient material is recommended to measure. Since from the CLT-concrete floor model calibration, it was observed that the dynamic stiffness has an important influence on the dynamic response of the floor. The dynamic stiffness should be a frequency-dependent value instead of just one constant value. By employing the method introduced in [52] and the frequency-dependent dynamic stiffness, the dynamic behavior of the resilient layer can be properly integrated into the model, and it can subsequently provide a more accurate model.

REFERENCES

1. Kohrmann, M., *Numerical Methods for the Vibro-Acoustic Assessment of Timber Floor Constructions*. 2017, Technische Universität München.
2. Oliver, C.D., et al., *Carbon, fossil fuel, and biodiversity mitigation with wood and forests.* Journal of Sustainable Forestry, 2014. **33**(3): p. 248-275.
3. Blon, D., *Influence des jonctions sur le comportement vibro-acoustique d'assemblages de structures bois pour le bâtiment*. 2016.
4. Caullet, J.-Y., *Bois et forêts de France.* Géoéconomie, 2013. **66**(3): p. 177-183.
5. Dagenais, C. and R. Desjardins, *Cases studies of performance-based design for mid-rise wood constructions in Quebec (Canada).* World Conference on Timber Engineering 2012, WCTE 2012, 2012. **2**: p. 293-301.
6. Flodén, O., *Vibration Transmission in Lightweight Buildings: Numerical Prediction Model*. 2016, Lund University.
7. Gustavsson, L., Pingoud, K., Sathre, R., *Carbon dioxide balance of wood substitution: comparing concrete- and wood-framed buildings,.* Mitigation and Adaption Strategies for Global Change, 2006(11): p. 667–691.
8. Chung, H. and G. Emms, *Fourier series solutions to the vibration of rectangular lightweight floor/ceiling structures.* ACTA Acustica united with Acustica, 2008. **94**(3): p. 401-409.
9. *Forest Sector Innovation in Canada*.
10. J.H., Z., *Simultaneous Measurement of Elastic Constants of Engineered Wood-based Panles by Modal Testing.*
11. Brandner, R., et al., *Cross laminated timber (CLT): overview and development.* European Journal of Wood and Wood Products, 2016. **74**(3): p. 331-351.
12. ISO, *ISO 10140-3: AcousticsLaboratory measurement of sound insulation of building elements, Part 3: Measurement of impact sound insulation*. 2016, International Organization for Standardization, Geneva, Switzerland.
13. ISO, *ISO 717-2: Acoustics - Rating of sound insulation in buildings and of building elements: Part 2: Impact sound insulation*. 2013, International Organization for Standardization, Geneva, Switzerland.
14. Negreira, J., *Vibroacoustic performance of wooden buildings: Prediction and Perception*. 2016: Lund University.
15. Forssén J., et al., *Acoustics in wooden buildings. State of the art 2008.* 2008, Vinnova project 2007-01653: Stockholm (2008).
16. Johansson, C., *Low-frequency impact sound insulation of a light weight wooden joist floor.* Applied Acoustics, 1995. **44**(2): p. 133-147.
17. Späh M., et al., *Subjective and Objective Evaluation of Impact Noise Sources in Wooden Buildings.* Building Acoustics, 2013. **20**(3): p. 193-213.
18. Mahn, J., *Prediction of flanking noise transmission in lightweight building constructions: A theoretical and experimental evaluation of the application of EN12354-1.* 2009.

19. Jarnerö, K., Bard, D., Simmons, C., *Vibration performance of apartment buildings with wooden lightweight framework – Residents survey and field measurements, Report 2013:17*, S. SP Technical Research Institute of Sweden, Editor. 2013.
20. Warren E. Blazier Jr, R.B.D., *Investigation of low‐frequency footfall noise in wood‐frame, multifamily building construction.* Journal of the Acoustical Society of America, 1994. **96**(1521).
21. Medveď, J., B. Ingeleare, and L. de Geetere. *Impact Sound Insulation Concept for Lightweight Timber Floor*. in *Advanced Materials Research*. 2014. Trans Tech Publ.
22. Ljunggren, F. and A. Ågren, *Elastic layers to reduce sound transmission in lightweight buildings.* Building Acoustics, 2013. **20**(1): p. 25-42.
23. Bolmsvik, Å. and A. Brandt, *Damping assessment of light wooden assembly with and without damping material.* Engineering Structures, 2013. **49**(Supplement C): p. 434-447.
24. Chung, H., et al., *Lightweight Floor/Ceiling Systems with Improved Impact Sound Insulation.* Building Acoustics, 2010. **17**(2): p. 129-141.
25. Ljunggren F., Simmons C., and Hagberg K., *Correlation between sound insulation and occupants' perception – Proposal of alternative single number rating of impact sound.* Applied Acoustics, 2014. **85**(Supplement C): p. 57-68.
26. Martins, C., et al., *Acoustic performance of timber and timber-concrete floors.* Construction and Building Materials, 2015. **101**(Part 1): p. 684-691.
27. Caniato, M., et al., *Acoustic of lightweight timber buildings: A review.* Renewable and Sustainable Energy Reviews, 2017. **80**(Supplement C): p. 585-596.
28. Filippoupolitis, M., et al., *Structural dynamics of a dowelled-joist timber floor in the low-frequency range modelled using finite element simulation.* Engineering Structures, 2017. **148**: p. 602-620.
29. Hopkins, C., *Sound insulation*. 2012: Routledge.
30. Zeitler, B., I. Sabourin, and S. Schoenwald, *Wood or concrete floor? - A comparison of direct sound insulation*, in *40th International Congress and Exposition on Noise Control Engineering 2011, INTER-NOISE 2011*. 2011. p. 2237-2243.
31. FP0702., C.A., *Net-Acoustics for Timber based lightweight buildings and elements.* 2012.
32. Ljunggren, F., C. Simmons, and R. Öqvist, *Correlation between sound insulation and occupants' perception – Proposal of alternative single number rating of impact sound, part II.* Applied Acoustics, 2017. **123**: p. 143-151.
33. Caniato, M., et al. *Recycled materials for noise reduction in floating floors*. in *22nd International Congress on Sound and Vibration, ICSV 2015*. 2015.
34. Homb, A., *Low frequency sound and vibrations from impacts on timber floor constructions.* Doctoral theses at NTNU, 2006. **132**.
35. Ljunggren, F. and A. Ågren, *Potential solutions to improved sound performance of volume based lightweight multi-storey timber buildings.* Applied Acoustics, 2011. **72**(4): p. 231-240.
36. Flodén O., Persson K., and Sandberg G., *Numerical methods for predicting vibrations in multi-story wood buildings*, in *World Conference On Timber Engineering*. 2016: Vienna, Austria.
37. Simmons, C., K. Hagberg, and E. Backman, *Acoustical Performance of Apartment Buildings–Resident's Survey and Field Measurements. AkuLite Report 2*. 2011.

38. Hveem, S., *Nordic multi-storey timber buildings for residential housing.* Proceedings Inter. noise 2000, 2000: p. 2429-2433.
39. Guigou-Carter, C., N. Balanant, and M. Villenave. *Acoustic comfort evaluation in lightweight wood-based buildings*. in *Proceedings of Forum Acusticum*. 2014.
40. Cremer, L., Heckl, M., Petersson, Björn A.T, *Structure-Borne Sound*. 2005: Springer-Verlag Berlin Heidelberg.
41. *ISO 12354-1: Building acoustics — Estimation of acoustic performance of buildings from the performance of elements, Part 1: Airborne sound insulation between rooms*. 2017, International Organization for Standardization, Geneva, Switzerland.
42. ISO, *ISO 12354-2: Building acoustics — Estimation of acoustic performance of buildings from the performance of elements, Part 2: Impact sound insulation between rooms*. 2017, International Organization for Standardization, Geneva, Switzerland.
43. ISO, *ISO 12354-3: Building acoustics — Estimation of acoustic performance of buildings from the performance of elements , Part 3: Airborne sound insulation against outdoor sound*. 2017, International Organization for Standardization, Geneva, Switzerland.
44. ISO, *ISO 12354-4: Building acoustics — Estimation of acoustic performance of buildings from the performance of elements, Part 4: Transmission of indoor sound to the outside*. 2017, International Organization for Standardization, Geneva, Switzerland.
45. Brunskog, J. *Energy based prediction models for building acoustics*. in *Joint Baltic-Nordic Acoustics Meeting 2012*. 2012.
46. Pedersen, D.B., *Evaluation of EN 12354 part 1 and 2 for Nordic dwelling houses.* Building Acoustics, 1999. **6**(3): p. 259-268.
47. Rasmussen, B. and J.H. Rindel, *Concepts for evaluation of sound insulation of dwellings - from chaos to consensus?* 2005.
48. Hu, L. and J.-P. Migneron, *Vibration and low-frequency impact sound generated by normal human walking in lightweight wood-joisted floor-ceiling assemblies.* 2011, 2011. **39**(3): p. 2.
49. Park, H.S., et al., *Low-frequency impact sound transmission of floating floor: Case study of mortar bed on concrete slab with continuous interlayer.* Building and Environment, 2015. **94**: p. 793-801.
50. Sipari P., *Sound Insulation of Multi-Storey Houses — A Summary of Finnish Impact Sound Insulation Results.* Building Acoustics, 2000. **7**(1): p. 15-30.
51. Homb, A., et al., *Impact sound insulation of wooden joist constructions: Collection of laboratory measurements and trend analysis.* Building Acoustics, 2016. **23**(2): p. 73-91.
52. Negreira, J., A. Sjöström, and D. Bard, *Low frequency vibroacoustic investigation of wooden T-junctions.* Applied Acoustics, 2016. **105**: p. 1-12.
53. Neves e Sousa, A. and B.M. Gibbs, *Low frequency impact sound transmission in dwellings through homogeneous concrete floors and floating floors.* Applied Acoustics, 2011. **72**(4): p. 177-189.
54. Negreira, J., *Vibroacoustic performance of wooden buildings - Prediction and perception*. 2016.
55. Persson, K., *Micromechanical modelling of wood and fibre properties*. 2000, Lund: [Univ.-bibl.].
56. Labonnote, N., *Damping in Timber Structures*. 2012.

57. Coguenanff C., *Robust design of lightweight wood-based systems in linear vibroacoustics*. 2015.
58. Zhou J.H., et al., *Elastic properties of full-size mass timber panels: Characterization using modal testing and comparison with model predictions.* Composites Part B: Engineering, 2017. **112**: p. 203-212.
59. FPInnovations, *CLT Handbook*.
60. Standardization, E.C.f., *EN 16351: Timber structures - cross laminated timber e requirements.* . 2015.
61. Hermansson, A., *Efficiency of floating floors on CLT or concrete plate in the low frequency region*, in *Department of Architechture and Civil Engineering*. 2018, Chalmers University of Technology.
62. Negreira, J., A. Sjöström, and D. Glebe, *Low-frequency behaviour of a sound field inside a reverberant room: Measurements and numerical prediction tools.* Building Acoustics. **0**(0): p. 1351010X19840974.
63. Caniato, M., et al., *Thermal and acoustic performance expectations on timber buildings.* Building Acoustics, 2017. **24**(4): p. 219-237.
64. Santoni, A., et al., *Determination of the elastic and stiffness characteristics of cross-laminated timber plates from flexural wave velocity measurements.* Journal of Sound and Vibration, 2017. **400**: p. 387-401.
65. Zhang, X., et al., *Experimental study on the impact sound insulation of cross laminated timber and timber-concrete composite floors.* Applied Acoustics, 2020. **161**: p. 107173.
66. ISO, *ISO 10140-2: Acoustics Laboratory measurement of sound insulation of building elements, Part 2: Measurement of airborne sound insulation*. 2016, International Organization for Standardization, Geneva, Switzerland.
67. Zeitler, B., S. Schoenwald, and I. Sabourin. *Direct impact sound insulation of cross laminate timber floors with and without toppings*. in *INTER-NOISE and NOISE-CON Congress and Conference Proceedings*. 2014. Institute of Noise Control Engineering.
68. Öqvist, R., F. Ljunggren, and A. Ågren, *On the uncertainty of building acoustic measurements–Case study of a cross-laminated timber construction.* Applied Acoustics, 2012. **73**(9): p. 904-912.
69. Kouyoumji, J.-L., S. Gagnon, and S. Boulet. *Sound transmission loss of Cross Laminated Timber CLT floors, measurements and modelling using SEA*. in *INTER-NOISE and NOISE-CON Congress and Conference Proceedings*. 2009. Institute of Noise Control Engineering.
70. Santoni, A., et al., *Modelling the radiation efficiency of orthotropic cross-laminated timber plates with simply-supported boundaries.* Applied Acoustics, 2019. **143**: p. 112-124.
71. Santoni, A., et al. *Sound radiation efficiency measurements on cross-laminated timber plates*. in *INTER-NOISE and NOISE-CON Congress and Conference Proceedings*. 2016. Institute of Noise Control Engineering.
72. Schoenwald, S., et al. *Sound insulation performance of cross laminated timber building systems*. in *INTER-NOISE and NOISE-CON congress and conference proceedings*. 2013. Institute of Noise Control Engineering.

73. Mahn, J., et al., *Apparent sound insulation in mass timber buildings*, in *Research Report (National Research Council of Canada. Construction); no. RR-335*. 2020, National Research Council of Canada. Construction.
74. Di Bella, A., et al. *Flanking transmission in CLT buildings: comparison between vibration reduction index measurements for different mounting conditions*. in *INTER-NOISE and NOISE-CON Congress and Conference Proceedings*. 2019. Institute of Noise Control Engineering.
75. Barbaresi, L., et al. *Experimental measurements of flanking transmission in CLT structures*. in *Proceedings of Meetings on Acoustics 22ICA*. 2016. Acoustical Society of America.
76. Di Bella, A. and M. Mitrovic, *Acoustic Characteristics of Cross-Laminated Timber Systems.* Sustainability, 2020. **12**(14): p. 5612.
77. Caniato, M., et al., *Impact sound of timber floors in sustainable buildings.* Building and Environment, 2017. **120**: p. 110-122.
78. Pagnoncelli, L. and F. Morales. *Cross-laminated timber system (CLT): laboratory and in situ measurements of airborne and impact sound insulation*. in *EuroRegio conference paper, Porto, Portugal*. 2016.
79. Hashimoto, N., *Measurement of sound radiation efficiency by the discrete calculation method.* Applied Acoustics, 2001. **62**(4): p. 429-446.
80. ISO, *ISO 12354-1: Building acoustics — Estimation of acoustic performance of buildings from the performance of elements — Part 1: Airborne sound insulation between rooms*. 2017, International Organization for Standardization, Geneva, Switzerland.
81. Santoni, A. and P. Fausti. *Field measurements to analyse flanking transmission in buildings*. in *Forum Acusticum 2014, Kracow*. 2014. The Polish Acoustical Society.
82. Burroughs, C.B., R.W. Fischer, and F.R. Kern, *An introduction to statistical energy analysis.* The Journal of the Acoustical Society of America, 1997. **101**(4): p. 1779-1789.
83. Lyon, R.H., R.G. DeJong, and M. Heckl, *Theory and application of statistical energy analysis.* The journal of the acoustical society of america, 1995. **98**(6): p. 3021-3021.
84. Burnett, D.S., *Finite element analysis: from concepts to applications*. 1987: Prentice Hall.
85. Ussher, E., et al. *Predicting effects of design variables on modal responses of CLT floors*. in *Structures*. 2017. Elsevier.
86. Ussher E., et al., *Prediction of motion responses of cross-laminated-timber slabs.* Structures. **11**: p. 49-61.
87. Hibbitt, Karlsson, and Sorensen, *ABAQUS/standard User's Manual*. Vol. 1. 2001: Hibbitt, Karlsson & Sorensen.
88. Ewins, D.J., *Modal testing: theory and practice*. Vol. 15. 1984: Research studies press Letchworth.
89. Bolmsvik, A., *Structural-acoustic vibrations in wooden assemblies*. 2013, PhD thesis, Linnaeus University-Suède.
90. Kjær, B., *Product data - Heavy Duty Impact Hammers - Type 8207, 8208 and 8210.* 2012.
91. JIS, *Measurement of floor impact sound insulation of buildings*, in *Part 2: Method using standard heavy impact sources*. 2000: Tokyo, Japan.

92. JIS, *Measurement of floor impact sound insulation of buildings*, in *Part 1: Method using standard light impact source*. 2000: Tokyo, Japan.
93. Shi, W., C. Johansson, and U. Sundbäck, *An investigation of the characteristics of impact sound sources for impact sound insulation measurement.* Applied Acoustics, 1997. **51**(1): p. 85-108.
94. ISO, *ISO 16283-2: Acoustics - Field measurement of sound insulation in buildings and of building elements, Part 2: Impact sound insulation* 2014, International Organization for Standardization, Geneva, Switzerland.
95. ISO, *ISO 10140-5: Acoustics - Laboratory measurement of sound insulation of building elements, Part 5: Requirements for test facilities and equipment*. 2016, International Organization for Standardization, Geneva, Switzerland.
96. Cremer L., H.M., *Structure-Borne Sound: Structural Vibrations and Sound Radiation at Audio Frequencies*. 1973.
97. Vér, I.L., *Impact Noise Isolation of Composite Floors.* The Journal of the Acoustical Society of America, 1971. **50**(4A): p. 1043-1050.
98. Scholl, W. and W. Maysenhölder, *Impact Sound Insulation of Timber Floors: Interaction between Source, Floor Coverings and Load Bearing Floor.* Building Acoustics, 1999. **6**(1): p. 43-61.
99. Brunskog, J. and P. Hammer, *The Interaction Between the ISO Tapping Machine and Lightweight Floors.* Acta Acustica united with Acustica, 2003. **89**(2): p. 296-308.
100. Rabold, A., et al., *Modelling the Excitation Force of a Standard Tapping Machine on Lightweight Floor Structures.* Building Acoustics, 2010. **17**(3): p. 175-197.
101. Persson P. and Flodén O., *Towards uncertainty quantification of vibrations in wood floors*. 2018.
102. Shannon C. E., *A Mathematical Theory of Communication.* Bell System Technical Journal, 1948. **27**(3): p. 379-423.
103. Staber B. and Guilleminot J., *Approximate Solutions of Lagrange Multipliers for Information-Theoretic Random Field Models*. Vol. 3. 2015.
104. Soize C., *Construction of probability distributions in high dimension using the maximum entropy principle: Applications to stochastic processes, random fields and random matrices.* International Journal for Numerical Methods in Engineering, 2008. **76**(10): p. 1583-1611.
105. Soize C., *Stochastic Models of Uncertainties in Computational Mechanics*. 2012.
106. Guilleminot J. and Soize C., *On the Statistical Dependence for the Components of Random Elasticity Tensors Exhibiting Material Symmetry Properties.* Journal of Elasticity, 2013. **111**(2): p. 109-130.
107. Guilleminot J. and Soize C., *Generalized stochastic approach for constitutive equation in linear elasticity: a random matrix model.* International Journal for Numerical Methods in Engineering, 2012. **90**(5): p. 613-635.
108. Schiavi, A., *Improvement of impact sound insulation: A constitutive model for floating floors.* Applied Acoustics, 2018. **129**: p. 64-71.
109. Kim, K.-W., et al., *Correlation between dynamic stiffness of resilient materials and heavyweight impact sound reduction level.* Building and Environment, 2009. **44**(8): p. 1589-1600.

110. Cho, T., *Vibro-acoustic characteristics of floating floor system: The influence of frequency-matched resonance on low frequency impact sound.* Journal of Sound and Vibration, 2013. **332**(1): p. 33-42.
111. ISO, *ISO 16283-1: Acoustics - Field measurement of sound insulation in buildings and of building elements, Part 1: Airborne sound insulation*. 2014, International Organization for Standardization, Geneva, Switzerland.
112. Warnock, A., *Controlling the transmission of impact sound through floors*. 1999: Institute for Research in Construction, National Research Council of Canada.
113. Dassault, *ABAQUS/CAE*. 2017, Simulia.
114. Juan Negreira, D.B., *Modelling of the tapping machine for finite element prediction tools - preliminary parametric studies*, in *International Congress on Acoustics*. 2016: Buenos Aires.
115. Ewins, D.J., *Modal testing: theory, practice, and application*. 2000: Research Studies Press.
116. Bolmsvik A., Linderholt A., and Jarnerö K. *FE modeling of a lightweight structure with different junctions*. in *Proceedings - European Conference on Noise Control*. 2012.
117. Wang P., et al., *Numerical prediction of impact sound in dwelling from low to high frequency*, in *Internoise*. 2018: Chicago, USA.
118. Negreira J., Sjöström A., and Bard D., *Low frequency vibroacoustic investigation of wooden T-junctions.* Applied Acoustics, 2016. **105**(Supplement C): p. 1-12.
119. Flodén O., Persson K., and Sandberg G., *A multi-level model correlation approach for low-frequency vibration transmission in wood structures.* Engineering Structures, 2018. **157**: p. 27-41.
120. Mathworks, *Matlab v2010b*. 2010.
121. Shang S. and Yun G.J., *Stochastic finite element with material uncertainties: Implementation in a general purpose simulation program.* Finite Elements in Analysis and Design, 2013. **64**: p. 65-78.
122. Stefanou G., *The stochastic finite element method: Past, present and future.* Computer Methods in Applied Mechanics and Engineering, 2009. **198**(9): p. 1031-1051.
123. Soize C., *Random matrix theory for modeling uncertainties in computational mechanics.* Computer Methods in Applied Mechanics and Engineering, 2005. **194**(12): p. 1333-1366.
124. Walpole L.J., *Fourth-rank tensors of the thirty-two crystal classes: multiplication tables.* Proceedings of the Royal Society of London. A. Mathematical and Physical Sciences, 1984. **391**(1800): p. 149-179.
125. Chib S. and Greenberg E., *Understanding the Metropolis-Hastings Algorithm.* The American Statistician, 1995. **49**(4): p. 327-335.
126. P. Robert C. and Casella G., *Monte Carlo Statistical Methods (Springer Texts in Statistics)*. 2005: Springer-Verlag.
127. P. Kroese D., Taimre T., and Botev Z., *Handbook of Monte Carlo Methods*. 2011.
128. Martini A. and Troncossi M., *Upgrade of an automated line for plastic cap manufacture based on experimental vibration analysis.* Case Studies in Mechanical Systems and Signal Processing, 2016. **3**: p. 28-33.
129. Hahn, G., *Sample sizes for Monte Carlo simulation.* 1972.

130. Hambric, S.A., *Structural acoustics tutorial—Part 1: vibrations in structures.* Acoustics Today, 2006. **2**(4): p. 21-33.
131. Negreira, J., et al., *Characterisation of an Elastomer for Noise and Vibration Insulation in Lightweight Timber Buildings.* Building Acoustics, 2014. **21**(4): p. 251-276.
132. Standardisation, E.C.f., *EN 1992-1-1 Eurocode 2: Design of concrete structures - Part 1-1: General rules and rules for buildings*. 2004.
133. Weber, S.G., *Data sheet of the Weber-floor Acoustic*.
134. Gobain, G.S., *Data sheet of Golvgipsskivor - GG 13*.
135. Chopra, A.K., *Dynamics of Structures: Theory and Applications to Earthquake Engineering, Prentice Hall.* Inc., Upper Saddle River, NJ, 1995.
136. Qian, C., et al., *Calibration of the ISO tapping machine for finite-element prediction tool on a wooden-base floor.* Building Acoustics. **0**(0): p. 1351010X19855227.
137. Hopkins, C. and R. Hall, *Impact Sound Insulation Using Timber Platform Floating Floors on a Concrete Floor Base.* Building Acoustics, 2006. **13**(4): p. 273-284.

ANNEXES

Python Code

Python script of the CLT model whose Young's modulus in longitudinal direction follows a normal distribution.

```
# -*- coding: mbcs -*-


from part import *
from material import *
from section import *
from assembly import *
from step import *
from interaction import *
from load import *
from mesh import *
from optimization import *
from job import *
from sketch import *
from visualization import *
from connectorBehavior import *

session.journalOptions.setValues(replayGeometry=COORDINATE,
recoverGeometry=COORDINATE)

Elastic_1 =
[7825056529,10017461733,8862702112,8468472563,8857371451,8397516970,84
37927825,9244848803,
9204517244,9208596206,8835748566,7896256538,8858619325,9315117644,8744
446885,9017346504,8863442566,8348279537,
8646935733,8106358598,8944197815,7926464946,7965564770,8095250652,7027
857919,9219190146,8662595269,8122535840,9185149270,
7644241790,8448878776,8379276479,8659603369,8656429298,8067560041,8484
974351,8417560490,8813853643,9046632834,9054636648]

E1 = 7825056529



for E1 in Elastic_1 :
```

```
    mdb.models['Model-1'].ConstrainedSketch(name='__profile__',
sheetSize=200.0)
    mdb.models['Model-1'].sketches['__profile__'].rectangle(point1=(-
2.0, -0.75),
        point2=(2.0, 0.75))
    mdb.models['Model-1'].Part(dimensionality=THREE_D, name='CLT',
type=
        DEFORMABLE_BODY)
    mdb.models['Model-1'].parts['CLT'].BaseSolidExtrude(depth=0.175,
sketch=
        mdb.models['Model-1'].sketches['__profile__'])
    del mdb.models['Model-1'].sketches['__profile__']
    mdb.models['Model-
1'].parts['CLT'].DatumPointByCoordinate(coords=(2.0, 0.75,
        0.035))
    mdb.models['Model-
1'].parts['CLT'].DatumPointByCoordinate(coords=(2.0, 0.75,
        0.07))
    mdb.models['Model-
1'].parts['CLT'].DatumPointByCoordinate(coords=(2.0, 0.75,
        0.105))
    mdb.models['Model-
1'].parts['CLT'].DatumPointByCoordinate(coords=(2.0, 0.75,
        0.14))
    mdb.models['Model-
1'].parts['CLT'].PartitionCellByPlanePointNormal(cells=
        mdb.models['Model-1'].parts['CLT'].cells.findAt(((2.0, 0.25,
0.116667), )),
        normal=mdb.models['Model-1'].parts['CLT'].edges.findAt((2.0,
0.75,
        0.04375), ), point=mdb.models['Model-
1'].parts['CLT'].datums[5])
    mdb.models['Model-
1'].parts['CLT'].PartitionCellByPlanePointNormal(cells=
        mdb.models['Model-1'].parts['CLT'].cells.findAt(((2.0, 0.25,
0.093333), )),
        normal=mdb.models['Model-1'].parts['CLT'].edges.findAt((2.0,
0.75, 0.035),
        ), point=mdb.models['Model-1'].parts['CLT'].datums[4])
    mdb.models['Model-
1'].parts['CLT'].PartitionCellByPlanePointNormal(cells=
        mdb.models['Model-1'].parts['CLT'].cells.findAt(((2.0, 0.25,
0.07), )),
        normal=mdb.models['Model-1'].parts['CLT'].edges.findAt((2.0,
0.75,
        0.02625), ), point=mdb.models['Model-
1'].parts['CLT'].datums[3])
    mdb.models['Model-
1'].parts['CLT'].PartitionCellByPlanePointNormal(cells=
```

```
        mdb.models['Model-1'].parts['CLT'].cells.findAt(((2.0, 0.25,
0.046667), )),
        normal=mdb.models['Model-1'].parts['CLT'].edges.findAt((2.0,
0.75, 0.0175),
        ), point=mdb.models['Model-1'].parts['CLT'].datums[2])
    mdb.models['Model-
1'].parts['CLT'].DatumCsysByThreePoints(coordSysType=
        CARTESIAN, line1=(1.0, 0.0, 0.0), line2=(0.0, 1.0, 0.0),
name='Longi',
        origin=mdb.models['Model-1'].parts['CLT'].InterestingPoint(
        mdb.models['Model-1'].parts['CLT'].edges.findAt((2.0, -0.75,
0.14875), ),
        MIDDLE))
    mdb.models['Model-
1'].parts['CLT'].DatumCsysByThreePoints(coordSysType=
        CARTESIAN, name='Trans', origin=
        mdb.models['Model-1'].parts['CLT'].InterestingPoint(
        mdb.models['Model-1'].parts['CLT'].edges.findAt((2.0, -0.75,
0.11375), ),
        MIDDLE), point1=mdb.models['Model-
1'].parts['CLT'].InterestingPoint(
        mdb.models['Model-1'].parts['CLT'].edges.findAt((2.0, 0.75,
0.11375), ),
        MIDDLE), point2=mdb.models['Model-
1'].parts['CLT'].InterestingPoint(
        mdb.models['Model-1'].parts['CLT'].edges.findAt((-2.0, 0.75,
0.11375), ),
        MIDDLE))




    # Material property

    mdb.models['Model-1'].Material(name='CLT')
    mdb.models['Model-
1'].materials['CLT'].Density(table=((515.0, ), ))
    mdb.models['Model-1'].materials['CLT'].Elastic(table=((E1,
    3800000000.0, 3800000000.0, 0.44, 0.3, 0.3, 800000000.0,
70000000.0,
    61800000.0), ), type=ENGINEERING_CONSTANTS)
    mdb.models['Model-1'].HomogeneousSolidSection(material='CLT',
name='CLT',
    thickness=None)
    mdb.models['Model-1'].parts['CLT'].Set(cells=
    mdb.models['Model-1'].parts['CLT'].cells.findAt(((2.0, 0.25,
0.023333), ),
    ((2.0, -0.25, 0.081667), ), ((2.0, -0.25, 0.046667), ), ((-2.0,
0.25,
    0.116667), ), ((2.0, -0.25, 0.151667), ), ), name='Set-1')
    mdb.models['Model-1'].parts['CLT'].SectionAssignment(offset=0.0,
offsetField=''
```

```
    , offsetType=MIDDLE_SURFACE, region=
    mdb.models['Model-1'].parts['CLT'].sets['Set-1'],
sectionName='CLT',
    thicknessAssignment=FROM_SECTION)
    mdb.models['Model-
1'].parts['CLT'].MaterialOrientation(additionalRotationField=
    '', additionalRotationType=ROTATION_NONE, angle=0.0, axis=AXIS_3,
    fieldName='', localCsys=mdb.models['Model-
1'].parts['CLT'].datums[10],
    orientationType=SYSTEM, region=Region(
    cells=mdb.models['Model-1'].parts['CLT'].cells.findAt(((2.0, 0.25,
    0.023333), ), ((2.0, -0.25, 0.081667), ), ((2.0, -0.25,
0.151667), ), )),
    stackDirection=STACK_3)
    mdb.models['Model-
1'].parts['CLT'].MaterialOrientation(additionalRotationField=
    '', additionalRotationType=ROTATION_NONE, angle=0.0, axis=AXIS_3,
    fieldName='', localCsys=mdb.models['Model-
1'].parts['CLT'].datums[11],
    orientationType=SYSTEM, region=Region(
    cells=mdb.models['Model-1'].parts['CLT'].cells.findAt(((2.0, -
0.25,
    0.046667), ), ((-2.0, 0.25, 0.116667), ), )),
stackDirection=STACK_3)


    # Assembly
    mdb.models['Model-1'].rootAssembly.DatumCsysByDefault(CARTESIAN)
    mdb.models['Model-1'].rootAssembly.Instance(dependent=OFF,
name='CLT-1', part=
    mdb.models['Model-1'].parts['CLT'])
    mdb.models['Model-1'].rootAssembly.Set(edges=
    mdb.models['Model-1'].rootAssembly.instances['CLT-
1'].edges.findAt(((2.0,
    0.375, 0.0), ), ((-2.0, -0.375, 0.0), ), ), name='BC')
    mdb.models['Model-1'].DisplacementBC(amplitude=UNSET,
createStepName='Initial',
    distributionType=UNIFORM, fieldName='', localCsys=None,
name='BC_SS',
    region=mdb.models['Model-1'].rootAssembly.sets['BC'], u1=SET,
u2=SET, u3=
    SET, ur1=SET, ur2=SET, ur3=SET)




    # Mesh
    mdb.models['Model-
1'].rootAssembly.seedPartInstance(deviationFactor=0.1,
    minSizeFactor=0.1, regions=(
    mdb.models['Model-1'].rootAssembly.instances['CLT-1'], ),
size=0.1)
```

```
    mdb.models['Model-1'].rootAssembly.generateMesh(regions=(
    mdb.models['Model-1'].rootAssembly.instances['CLT-1'], ))
    mdb.models['Model-
1'].rootAssembly.setElementType(elemTypes=(ElemType(
    elemCode=C3D20R, elemLibrary=STANDARD), ElemType(elemCode=C3D15,
    elemLibrary=STANDARD), ElemType(elemCode=C3D10,
elemLibrary=STANDARD)),
    regions=(
    mdb.models['Model-1'].rootAssembly.instances['CLT-
1'].cells.findAt(((2.0,
    0.25, 0.023333), ), ((2.0, -0.25, 0.081667), ), ((2.0, -0.25,
0.046667), ),
    ((-2.0, 0.25, 0.116667), ), ((2.0, -0.25, 0.151667), ), ), ))


    # Set driving point
    mdb.models['Model-1'].rootAssembly.Set(name='Driving point 13',
nodes=
    mdb.models['Model-1'].rootAssembly.instances['CLT-
1'].nodes[3833:3834])

    mdb.models['Model-1'].FrequencyStep(maxEigen=200.0, name='Step-1',
previous=
    'Initial')




    mdb.models['Model-1'].SteadyStateModalStep(compositeDamping=None,
subdivideUsingEigenfrequencies=
    OFF, directDamping=None, directDampingByFrequency=((22.0, 0.049),
(33.0, 0.036),
    (56.0, 0.0318), (72.0, 0.0316), (105.0, 0.033), (118.0, 0.028),
(140.0,
    0.0174), (170.0, 0.0124)), frequencyRange=((0.0, 200.0, 400,
1.0), ), name=
    'Step-2', previous='Step-1', rayleighDamping=None, scale=LINEAR,
    structuralDamping=None)

    # Concentrate force
    mdb.models['Model-1'].ConcentratedForce(cf3=(-1+0j),
createStepName='Step-2',
    distributionType=UNIFORM, field='', localCsys=None, name='Load-1',
region=
    mdb.models['Model-1'].rootAssembly.sets['Driving point 13'])



    mdb.Job(atTime=None, contactPrint=OFF, description='',
echoPrint=OFF,
            explicitPrecision=SINGLE, getMemoryFromAnalysis=True,
historyPrint=OFF,
```

```
            memory=90, memoryUnits=PERCENTAGE, model='Model-1',
modelPrint=OFF,
            multiprocessingMode=DEFAULT, name='Eigenfreq_'+str(E1)+'',
nodalOutputPrecision=SINGLE,
            numCpus=6, numDomains=6, numGPUs=0, queue=None,
resultsFormat=ODB, scratch=
            '', type=ANALYSIS, userSubroutine='', waitHours=0,
waitMinutes=0)

    mdb.models['Model-1'].fieldOutputRequests['F-Output-
2'].setValues(variables=(
    'U', 'V', 'A'))


mdb.jobs['Eigenfreq_'+str(E1)+''].submit(consistencyChecking=OFF)#,
datacheckJob=True)
```

Matlab Code

Random_generator_Lagrange_multiplier.m

```
close all

clear variables
clc

N = 5; % number of variables

delta_r = 0.001; % 1 discretization step

f0 = 1000;

ns = 15e5; % Convergence number

mu = zeros(1,N); % sqrt(delta_r).*ones(1,N); % Expectation

sigma = sqrt(delta_r).*eye(N); % Covariance matrix

W = mvnrnd(mu,sigma,ns);

delta_W = zeros(ns,N);

for ii =1:N
for jj = 1:ns-1

delta_W(jj,ii) = W(jj+1,ii)-W(jj,ii);

end
end

delta_W(1,:) = 0;

% histogram(delta_W(:,1))

% stem(delta_W(:,1))

U = zeros(ns,N);

U(1,:) = [182.6657 10.6232 4.2066 9.5238 14];

% U(:,1) = normrnd(182.6657,1,[1,ns]);
%
% U(:,2) = normrnd(10.6232,1,[1,ns]);
%
% U(:,3) = normrnd(4.2066,1,[1,ns]);
%
% U(:,4) = normrnd(9.5238,1,[1,ns]);
%
% U(:,5) = normrnd(14,1,[1,ns]);
```

```
% delta_U = zeros(ns,N);

V = ones(ns,N)./100;

% V = zeros(ns,N);

Lk = zeros(ns,N);

lamda =  [0.6142 10.5644,-0.4852, 23.2096, 15.7301, -110];

for kk = 1:ns-1

    for jj = 1:N


        U(kk+1,jj) = U(kk,jj)+delta_r.*V(kk,jj);

        g_U = [U(kk,:) log(U(kk,4)^2*U(kk,5)^2*(U(kk,1)*U(kk,2)-U(kk,3)^2))];

        phi_2 = lamda*g_U';

        exchange = U(kk,jj);

        U(kk,jj) = U(kk+1,jj);

        g_U = [U(kk,:) log(U(kk,4)^2*U(kk,5)^2*(U(kk,1)*U(kk,2)-U(kk,3)^2))];

        phi_1 = lamda*g_U';

        U(kk,jj) = exchange;

        Lk(kk,jj) = -(phi_1-phi_2).*lamda(jj)./(U(kk+1,jj)-U(kk,jj));%-
lamda(jj);%-(a-b)*lamda/(c-b);%K = -(a.*lamda-b.*lamda)./(c-b);



        V(kk+1,jj) = (1-
f0*delta_r/2).*V(kk,jj)+delta_r.*Lk(kk,jj)+sqrt(f0).*delta_W(kk+1,jj);

    end
end
%
% histogram(V(:,1))
% mean(V(:,1))

m = zeros(1,ns);

m(1,1) = U(1,1).^2;

for ll = 1:ns-1
```

```
m(ll+1) = (m(ll).*ll+U(ll+1,1).^2)/(ll+1);

end

mean(U(:,1))

mean(U(:,2))

mean(U(:,3))

mean(U(:,4))

mean(U(:,5))

figure;
plot(V(:,1))
figure;
plot(U(:,1))
figure;
plot(U(:,2))
figure;
plot(U(:,3))
figure;
plot(U(:,4))
figure;
plot(U(:,5))

figure;
plot(m)
```

M_H_sampling_independent_c7.m

```
close all

clear variables
clc

%% Initial data
% Parameters
N      = 5e4;    % Number of samples (iterations)
burnin = 100;     % Number of runs until the chain approaches stationarity
lag    = 10;       % Thinning or lag period: storing only every lagth point
acc    = 0;        % To note the acceptance
% Storage and initial points
theta = zeros(1,N);   % Samples drawn from the Markov chain
tt    = 0.09;      % Start points or initial states of the chain in C

%% Target PDF
lamda0 = -1.1618;
lamda7 = 12.9089;
```

```
% Target PDF definition
k7 = lamda7.^(1-2*lamda0)./gamma(1-2*lamda0);
Target_p = @(c7) k7*c7.^(-lamda0).*exp(-
lamda7.*c7)*(c7>0);%*(0.315>c7)*(c7>0.045);


%% Proposal PDF (proposal distribution)
proposal_PDF = @(X,mu) mvnpdf(X,mu,eye(1));           % Proposal PDF
sample_from_proposal_PDF = @(mu) mvnrnd(mu,eye(1));   % Function that samples
from proposal PDF


%% M-H routine
for i = 1:burnin    % First make the burn-in stage
   [tt a] = MH_routine(tt,Target_p,proposal_PDF,sample_from_proposal_PDF);
end
for i = 1:N    % Cycle to the number of samples
   for j = 1:lag    % Cycle to make the thinning
      [tt a] = MH_routine(tt,Target_p,proposal_PDF,sample_from_proposal_PDF);
   end
   theta(:,i) = tt;         % Store the chosen states
   acc        = acc + a;    % Accepted ?
end
accrate = acc/N;            % Acceptance rate

c7 = linspace(0,10);
p = @(c7) k7.*c7.^(-lamda0).*exp(-lamda7.*c7);

%% Plots
figure;
hist(theta(1,:), ceil(sqrt(N)))
% hold on
% plot(c7,ff,'linewidth',4)
% hold on
% plot(c7,p(c7),'r','linewidth',4)

%% Export/save data
%save('c7.mat','theta')
```